Higgs Boson Pair Production via Gluon Fusion: Full NLO QCD Corrections

---

Dissertation

zur

Erlangung der naturwissenschaftlichen Doktorwürde
(Dr. sc. nat.)

vorgelegt der

Mathematisch-naturwissenschaftlichen Fakultät

der

Universität Zürich

von

Seraina Glaus

aus

Thalwil ZH

Promotionskommission

Prof. Dr. Thomas Gehrmann (Vorsitz)

PD Dr. Michael Spira (Leitung der Dissertation)

Prof. Dr. Massimiliano Grazzini

Prof. Dr. Adrian Signer

Zürich, 2018

Abstract

The measured properties of the particle detected six years ago at the LHC at CERN indicate that it is compatible with the Higgs boson predicted by the Standard Model. However, the theoretical and experimental uncertainties allow associations with extended models. Therefore it is of essential importance to investigate the properties of this particle in more detail. The determination of the Higgs potential is crucial to test whether this particle causes electroweak symmetry breaking. The self-coupling strength has to be determined to measure the Higgs potential. This can be achieved in a first step by measuring the trilinear self-coupling in Higgs pair production. At the LHC, the dominant process of Higgs pair production is the loop induced gluon fusion. Therefore the main goal of this thesis is the calculation of the next-to-leading order (NLO) QCD corrections considering the complete top-quark mass dependence in the framework of the Standard Model. The relevant two-loop integrals cannot be calculated analytically with the currently known methods. Instead a numerical integration is required. The main challenge is the extraction of the ultraviolet, the infrared and the collinear divergences from the amplitudes. For this purpose, a modified end-point subtraction has been developed for the extraction of the IR-singularities. Publicly available programs have been used for the real corrections. The differential cross section has been obtained as a distribution in the invariant Higgs pair mass. It shows that the main contributions to the cross section emerge from the invariant Higgs pair masses between 300 and 800 GeV and that the heavy-top limit is a reasonable approximation for invariant Higgs pair masses only up to about 600 GeV. Further, it can be observed that for an invariant Higgs pair mass up to 400-600 GeV the NLO QCD corrections can be reasonably approximated by the K-factor of the triangular contributions alone. The obtained hadronic cross section implies a negative contribution of about -15% from NLO mass effects compared to the previous known heavy-top limit results involving the full leading-order mass dependence.

Zusammenfassung

Die gemessenen Eigenschaften des vor sechs Jahren am CERN detektierten Teilchens weisen darauf hin, dass es sich um das langgesuchte Higgsboson des Standardmodells handelt. Jedoch lassen die theoretischen wie auch experimentellen Unsicherheiten Zuordnungen zu anderen erweiterten Modellen zu. Deshalb ist es von ausschlaggebender Bedeutung, die Eigenschaften des detektierten Teilchens genauer zu bestimmen. Dabei spielt die Messung des Higgspotentials eine zentrale Rolle, um zu prüfen, ob dieses Teilchen effektiv für die elektroschwache Symmetriebrechung verantwortlich ist. Um das Higgspotential zu messen, muss die Selbstwechselwirkungsstärke zwischen Higgsbosonen direkt bestimmt werden. Dies ist über Higgspaarproduktion zur Bestimmung der trilineare Kopplung möglich. Der dominante Prozess der Higgspaarproduktion ist die loop-induzierte Gluonfusion. Ziel dieser Arbeit ist die Berechnung der NLO QCD-Korrekturen unter Berücksichtigung der vollen Topquarkmassenabhängigkeit im Rahmen des Standardmodells. Die relevanten Zwei-Loop-Integrale können analytisch nicht mit gegenwärtig bekannten Methoden berechnet werden. Stattdessen ist eine numerische Integration nötig. Die grösste Herausforderung ist die Extraktion der ultravioletten, der infraroten wie auch der kollinearen Divergenzen der Amplituden. Dazu wurde die bekannte Endpunktsubtraktionsmethode erweitert. Für die reellen Korrekturen wurden die Programme FeynArts und FormCalc verwendet. Der differentielle Wirkungsquerschnitt wurde als Funktion der invarianten Higgspaarmasse bestimmt. Daraus wird ersichtlich, dass die grössten Beiträge zum Wirkungsquerschnitt von dem invarianten Higgspaarmassenbereich zwischen 300 und 800 GeV kommen, und dass der Heavy-Top-Limit bis ungefähr 600 GeV eine gute Näherung ist. Für eine invariante Higgspaarmasse bis 400-600 GeV können die NLO QCD-Korrekturen durch den K-Faktor der Dreiecksbeiträge angenähert werden. Der berechnete totale hadronische Wirkungsquerschnitt impliziert NLO Masseneffekte von -15% verglichen zu den bekannten Heavy-Top-Limit Resultaten, welche die volle Massenabhängigkeit in führender Ordnung berücksichtigen.

Contents

Chapter 1

Introduction

1.1 Standard Model

The Standard Model (SM) of particle physics is a successful and elegant model to describe particle physics processes in nature. The SM provides a set of elementary particles and characterizes their properties and interactions in the framework of a spontaneously broken gauge theory. Its development is based on experimental data gathered in collider and low-energy experiments. The SM is a quantum field theory which is symmetric under the non-abelian $SU(3)_C \otimes SU(2)_L \otimes U(1)_Y$ gauge group. The first one is the symmetry group of the strong interaction between quarks and gluons described by quantum chromodynamics (QCD) [1–9]. The $SU(2)_L \otimes U(1)_Y$ symmetry describes the unified electromagnetic and weak interactions [10–12].

Leptons and quarks build together the fundamental constituents of matter characterized by their quantum numbers. For every lepton and quark there is an antiparticle with the same mass but opposite inner quantum numbers. Leptons and quarks appear in three generations with left-handed isospin doublets and right-handed singlets.

$$\begin{array}{cccccc} \begin{pmatrix} \nu_e \\ e \end{pmatrix}_L & e_R & \begin{pmatrix} \nu_\mu \\ \mu \end{pmatrix}_L & \mu_R & \begin{pmatrix} \nu_\tau \\ \tau \end{pmatrix}_L & \tau_R \\ \begin{pmatrix} u \\ d \end{pmatrix}_L & u_R & \begin{pmatrix} c \\ s \end{pmatrix}_L & c_R & \begin{pmatrix} t \\ b \end{pmatrix}_L & t_R \\ & d_R & & s_R & & b_R \end{array} \tag{1.1}$$

The Lagrange density of the SM, $\mathcal{L}_{SM}$, can be split into the kinetic part of the gauge bosons, $\mathcal{L}_V$, the kinetic properties of the fermions and their couplings to the gauge bosons, $\mathcal{L}_f$, the Higgs sector, $\mathcal{L}_H$, and the Yukawa interaction of the Higgs boson with the fermions, $\mathcal{L}_Y$,

$$\mathcal{L}_{SM} = \mathcal{L}_V + \mathcal{L}_f + \mathcal{L}_H + \mathcal{L}_Y \,. \tag{1.2}$$

Every generator of the symmetry group results in a gauge field. Hence we have 8 gluon fields G_μ^a (a=1,...,8) for the strong interaction and 4 fields W_μ^a (a=1,...3) and B_μ for the electroweak interaction. The kinetic part of the gauge fields can then be written as

$$\mathcal{L}_V = -\frac{1}{2}\mathrm{Tr}\sum_{\mathrm{V=G,W,B}}\frac{1}{\mathrm{ig_V}}\left[\mathrm{D_\mu^V},\mathrm{D_\nu^V}\right]^2 \tag{1.3}$$

with the covariant derivatives $D_\mu^V = \partial_\mu + ig_V V_\mu$ and the gauge fields $V_\mu = T^a V_\mu^a$. T^a are the generators of the associated symmetry group and g_V the coupling strength of the corresponding gauge field. The physical particles Z^0 and the photon A are obtained by a rotation of the neutral component W^3- and B-fields by the Weinberg angle θ_w,

$$\begin{pmatrix} A \\ Z \end{pmatrix} = \begin{pmatrix} \cos\theta_w & \sin\theta_w \\ -\sin\theta_w & \cos\theta_w \end{pmatrix}\begin{pmatrix} B \\ W^3 \end{pmatrix}. \tag{1.4}$$

The charged W bosons are a superposition of the first two W fields

$$W^\pm = \frac{1}{\sqrt{2}}\left(W^1 \mp iW^2\right). \tag{1.5}$$

The kinetic part of the Lagrangian for the fermions f can be expressed as

$$\mathcal{L}_f = \sum_f \bar{f}_i\gamma^\mu D_\mu f \tag{1.6}$$

with the covariant derivative $D_\mu = \partial_\mu + i\sum_V g_V V_\mu$.

The Higgs sector of the SM is necessary to introduce massive particles. Gauge symmetry demands massless gauge fields to preserve gauge invariance in general. However, experiments provide ample evidence for massive gauge fields. Therefore, a mechanism is needed introducing masses to certain particles, but still preserving unitarity and the renormalizability of the theory. This can be achieved by the Higgs mechanism which is based on spontaneous symmetry breaking [13–18]. It introduces a Higgs doublet ϕ which acquires the following form in the unitary gauge

$$\phi = \begin{pmatrix} \phi^+ \\ \phi^0 \end{pmatrix} \to \frac{1}{\sqrt{2}}\begin{pmatrix} 0 \\ v+H \end{pmatrix} \tag{1.7}$$

where $v = 1/\sqrt{\sqrt{2}G_F}$ is its vacuum expectation value. It can be determined experimentally to high precision from muon decay using Fermi theory in terms of the Fermi constant G_F. Thereby the three remaining degrees of freedom are absorbed in the longitudinal polarization states of the massive vector bosons. Only one scalar Higgs

boson H is left over as a physical particle. The vacuum expectation value causes a shift of the ground state from the symmetric origin. The model is still locally invariant under $\mathrm{SU(2)_I} \times \mathrm{U(1)_Y}$ gauge transformations. Hence, renormalizability is maintained [19, 20]. The non-trivial ground state of the Higgs field is established with a finite Higgs field strength such that all particles interacting with the Higgs field acquire a mass term. This implies in addition that the Higgs couplings to the SM particles grow proportionally to their masses. In this way, the electroweak symmetry is hidden and thus not visible in the spectrum of states and the observables with the exception of the electromagnetic $\mathrm{U(1)_{em}}$ and $\mathrm{SU(3)_c}$. Therefore the photon, respectively the gluon, remains massless. The Higgs sector of the Lagrangian reads

$$\mathcal{L}_H = |D_\mu \phi|^2 - \frac{\lambda}{2}\left(|\phi|^2 - \frac{v^2}{2}\right)^2 . \tag{1.8}$$

Finally, the Yukawa part of the Lagrangian can be expressed as

$$\mathcal{L}_Y = \sum_f g_f \bar{f}_L(\phi + \phi_c) f_R + h.c. , \tag{1.9}$$

where ϕ_c is the charge conjugated Higgs field. ϕ_c gives rise to fermion masses with isospin $+1/2$ while ϕ induces fermion masses with isospin $-1/2$. The neutrinos have a vanishing coupling strength and are therefore massless in the original version of the SM[1].

The last missing particle predicted by the SM, the Higgs boson, was detected at the LHC in 2012 at CERN [21, 22]. Figure 1.1 shows the branching ratios for the individual decay modes in the Higgs boson mass range of 120 to 130 GeV. The branching ratios have been produced with PROPHECY4F for the decays $H \to WW/ZZ$ [23–25] and HDECAY for all the other decay channels [26–29]. The latter is a program calculating the branching ratios and decay widths of the Higgs boson in the SM and MSSM for the allowed decays. It considers all the relevant higher-order QCD corrections for the decays of a Higgs boson into quark pairs or gluons. PROPHECY4F is a Monte Carlo generator for $H \to WW/ZZ \to 4f$. It considers the decays into intermediate WW and ZZ states and their interferences for the same final states. The leading-order (LO) and next-to-leading order (NLO) partial width for any 4-fermion final state are included. The total uncertainties are represented by the size of the bands in Figure 1.1. The uncertainties in the branching ratios of the individual Higgs boson decay channels originate from missing higher-order corrections

[1]Neutrino masses as required by the observation of neutrino oscillations require extensions of the original SM framework. However, they do not play a role at high-energy colliders.

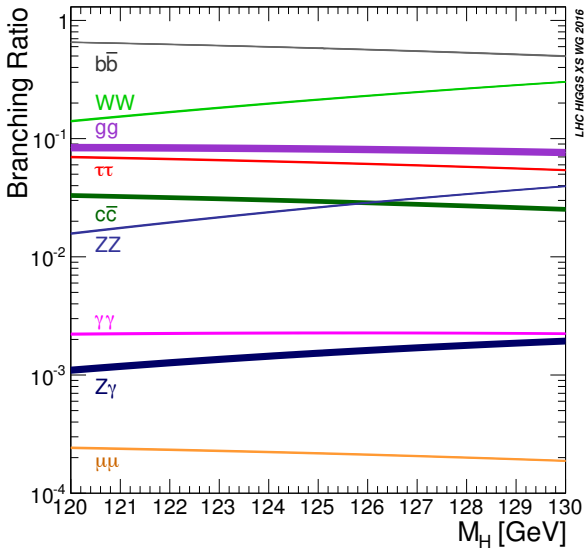

Figure 1.1: Higgs boson branching ratios with uncertainty bands representing the theoretical and parametric uncertainties [30].

and parametric uncertainties. The main uncertainties from the latter come from the strong coupling constant α_s and the top, bottom and charm quark masses. For α_s its value at the Z boson mass scale has been chosen, $\alpha_s(M_Z) = 0.118 \pm 0.0015$. The $\overline{MS}$ masses have been introduced for the two lighter quarks as [30]

$$\overline{m}_b(\overline{m}_b) = (4.18 \pm 0.03)\text{GeV},$$
$$\overline{m}_c(3\text{GeV}) = (0.986 \pm 0.026)\text{GeV},$$

while the pole mass of the top quark has been chosen as [30]

$$m_t = (172.5 \pm 1)\text{GeV}.$$

The resulting parametric uncertainties have been determined by the quadratic sum of the individual contributions of the input parameters to a certain decay mode.

The theoretical uncertainties have been estimated by the missing QCD and electroweak higher-order contributions considered by HDECAY and PROPHECY4F. For the decays $H \to b\bar{b}$, $c\bar{c}$ the QCD corrections are implemented up to N^{4}LO in HDECAY with a remaining scale dependence of 0.2% [31–41]. The electroweak corrections are implemented up to NLO [42–45]. For $H \to \tau^+\tau^-$ the electroweak corrections are as well included up to NLO. In HDECAY, the complete massive NLO QCD corrections [46–48] are implemented and interpolated to the large Higgs mass results at N^{4}LO. The electroweak corrections due to the self-interaction of the Higgs boson beyond NLO are included [49–52]. The missing electroweak contributions are

Partial width	QCD	Electroweak	Total	on-shell Higgs
$H \to b\bar{b}/c\bar{c}$	$\sim 0.2\%$	$\sim 0.5\%$	$\sim 0.5\%$	$\mathrm{N^4LO/NLO}$
$H \to \tau^+\tau^-/\mu^+\mu^-$	–	$\sim 0.5\%$	$\sim 0.5\%$	$--/\mathrm{NLO}$
$H \to gg$	$\sim 3\%$	$\sim 1\%$	$\sim 3\%$	$\mathrm{N^3LO/NLO}$
$H \to \gamma\gamma$	$< 1\%$	$< 1\%$	$\sim 1\%$	NLO/NLO
$H \to Z\gamma$	$< 1\%$	$\sim 5\%$	$\sim 5\%$	LO/LO
$H \to WW/ZZ \to 4f$	$< 0.5\%$	$\sim 0.5\%$	$\sim 0.5\%$	NLO/NLO

Table 1.1: Theoretical uncertainties originating from the missing higher-order corrections and the order of the radiative QCD/ electroweak corrections included in the partial decay modes.

estimated to be about 0.5% [30]. Further, in HDECAY the QCD corrections for $H \to gg$ are implemented up to $\mathrm{N^3LO}$ in the heavy-top limit (HTL) [53–56] and the scale dependence leads to an uncertainty of 3%. For this process the electroweak corrections are known up to NLO [57–63]. For the decay of a Higgs boson to two photons the electroweak contributions are calculated up to the two-loop level [63–65]. They yield a decrease of about 2% in the partical photonic decay width. The two-loop QCD corrections are known considering the full quark mass. In the heavy-top limit the three-loop QCD corrections are known. They lead to an additional contribution at the per mille level [66–78]. For $H \to Z\gamma$ the LO partial decay width is considered by HDECAY. The QCD corrections for this process are small and therefore neglected [79–81]. Finally, for $H \to WW/ZZ \to 4f$ the complete NLO QCD and electroweak corrections, considering all interference terms and leading two-loop heavy Higgs corrections, are included using PROPHECY4F. A detailed summary can be found in Table 1.1. These uncertainties and the ones of the input parameters are added linearly.

Figure 1.2 shows the LO Feynman diagrams for the four different production channels for a single Higgs boson at hadron colliders. The dominant production channel at the LHC for a single Higgs boson is gluon fusion as can be seen in Figure 1.3. For this channel the full QCD corrections are known up to NLO [54, 55, 82, 83]. Higher-order contributions are approximated by the heavy-top-quark limit [84–98]. The next relevant production channel is vector boson fusion for which the full QCD and electroweak corrections are known up to NLO [99–104]. The electroweak corrections have been calculated using the Monte Carlo program HAWK [105]. The QCD

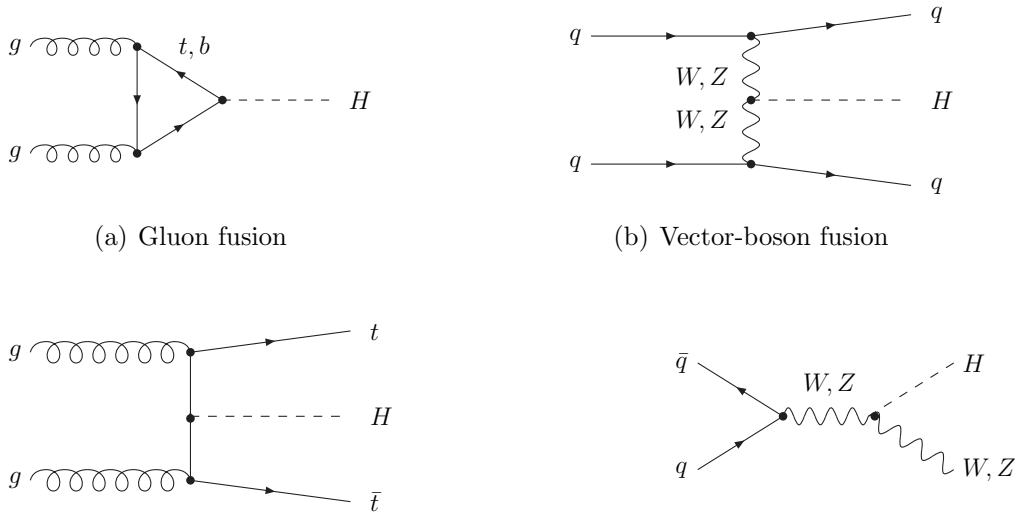

(a) Gluon fusion

(b) Vector-boson fusion

(c) Higgs bremsstrahlung off top-quarks

(d) Higgs-strahlung

Figure 1.2: The four different production channels for a single Higgs boson at hadron colliders.

NNLO and N^{3}LO corrections are known in the structure function approach [106–109]. At NLO it has been found that the effects beyond the structure function approach are smaller than 1% and therefore this is a reliable approximation. Further, there is the Higgs-strahlung and the Higgs bremsstrahlung off top quarks. For the former, the QCD corrections are calculated up to NNLO [110–113] and the electroweak corrections at NLO level using the program HAWK [105, 114, 115]. For the latter, both the QCD [116–120] and the electroweak corrections [121, 122] are known up to NLO. In addition, the NNLO corrections are approximated by a soft gluon resummation [123–125]. The Higgs boson production cross sections have been calculated using all the known higher-order corrections and the latest parton density functions, i.e. PDF4LHC15 [126]. Figure 1.3 shows the obtained cross sections for the individual channels for a Higgs mass of 125 GeV in a center of mass energy range of 6 to 15 TeV. The size of the error bands include the theoretical and parametric uncertainties. The same values as in the case for the branching ratio were used for the input parameters. For all production channels for which the results are known beyond NLO in QCD the uncertainties are at the few-per-cent level. The remaining uncertainty for gluon fusion is about 5%, the uncertainty for vector boson fusion is about 3% and for WH/ZH Higgsstrahlung about 4%. The uncertainties for $t\bar{t}H$ production are about $10-15\%$, for $b\bar{b}H$ production about $20-25\%$ and for $s-$ and $t-$channel tH production about $15-20\%$.

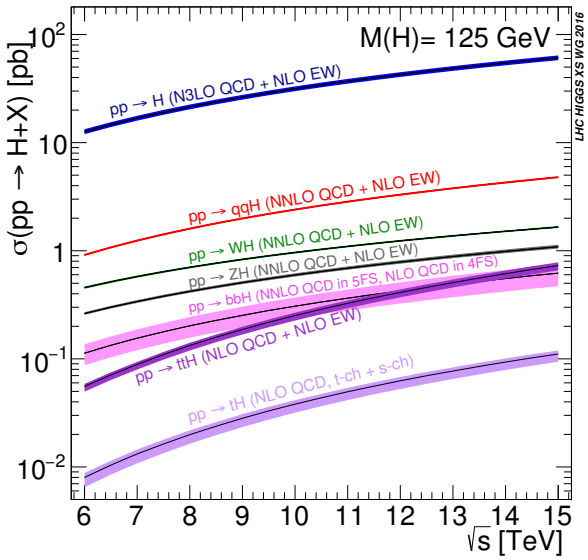

Figure 1.3: Single Higgs boson production cross sections as a function of the center of mass energy $\sqrt{s}$ at the LHC [30]. The theoretical and parametric uncertainties are reflected by the size of the error bands. The brackets show the included QCD and electroweak higher-order corrections.

1.2 Motivation

The measured properties of the detected Higgs boson indicate that it is consistent with the SM Higgs boson. For instance, the mass of (125.09 ± 0.24) GeV, zero spin and the positive CP quantum numbers are confirmed properties [21, 22, 127–131]. Further, its coupling strengths to other particles follow the SM prediction within the uncertainties. This can be inferred from Figure 1.4 where the coupling strengths of the Higgs boson to the heavy fermions and the vector bosons are illustrated. The theoretical uncertainties resulting from the missing higher-order corrections and the experimental uncertainties are represented by the size of the bands. Despite all those indications, to clarify whether it is indeed the SM Higgs boson the trilinear and quartic self-couplings have to be measured, since the shape of the Higgs potential can be reconstructed from this measurement. At the current performance state of the LHC, it will not be possible to measure the trilinear Higgs self-coupling. Such possibility will, however, be enabled at the future high luminosity LHC or other future colliders [132–152]. The quartic Higgs self-coupling will not be accessible due to its very small related cross sections [153–158]. A first step for a direct measurement of the trilinear coupling is provided by Higgs pair production. There are four different production channels for Higgs pair production (see Figure 1.5): gluon fusion [160–163], vector-boson fusion [138, 162, 164–168], double Higgs bremsstrahlung off top-

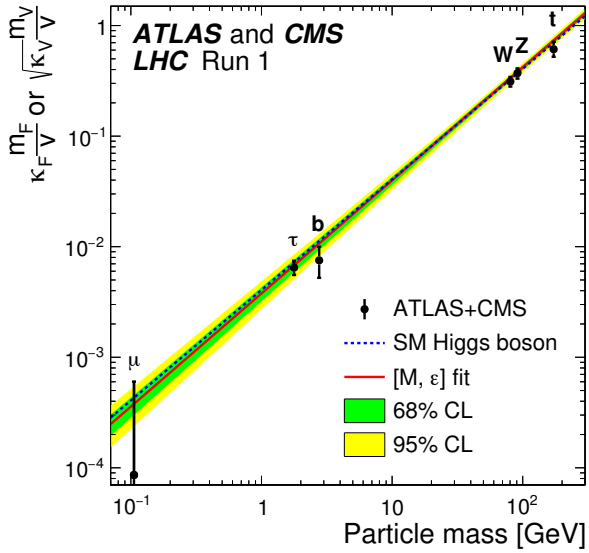

Figure 1.4: Higgs boson couplings to vector bosons and heavy fermions as a function of their masses for the combined ATLAS and CMS data of Run 1. In green/ yellow the 68%/ 95% the negative log-likelihood contours are shown [159].

quarks [138, 169, 170] and double Higgs-strahlung [138, 162, 171]. Gluon fusion is the dominant production channel by more than an order of magnitude (see Figure 1.6). The production cross section of Higgs boson pairs is about three orders of magnitude smaller than the single Higgs production cross section. The four production modes contain diagrams involving the trilinear Higgs self-coupling. The other remaining diagrams generate an irreducible background for the observation of the trilinear Higgs coupling. As can be inferred from Figure 1.6, for the gluon fusion process the relative uncertainty in the trilinear coupling is proportional to the relative uncertainty of cross section since the negative slope of the relative variations of the cross section as a function of the trilinear coupling λ in units of the SM coupling is about the same

$$\frac{\Delta\sigma}{\sigma} \sim -\frac{\Delta\lambda}{\lambda}. \tag{1.10}$$

A reduction of the uncertainty in the cross section results therefore in a better accuracy of the extracted trilinear coupling. This underlines the importance of higher-order corrections to reduce the uncertainty in the cross section. The Higgs boson self-coupling λ is defined by the Higgs potential V,

$$V(\phi) = \frac{\lambda}{2}\left\{|\phi|^2 - \frac{v^2}{2}\right\}^2. \tag{1.11}$$

An expansion around the vacuum expectation value establishes a quadratic dependence of the trilinear Higgs self-coupling, respectively quartic Higgs self-coupling, on

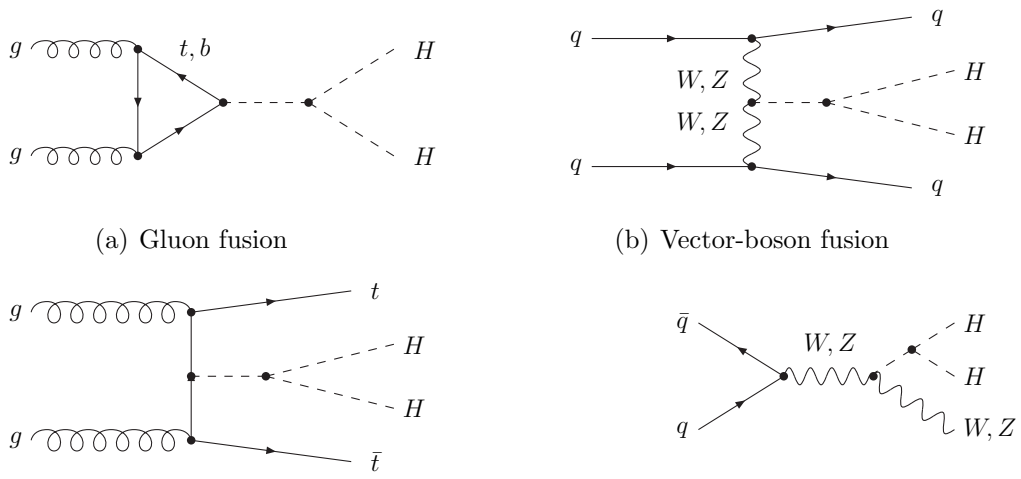

(a) Gluon fusion

(b) Vector-boson fusion

(c) Double Higgs bremsstrahlung off top-quarks

(d) Double Higgs-strahlung

Figure 1.5: The four different production channels for Higgs boson pairs at hadron colliders.

the Higgs mass,

$$\lambda = \frac{m_h^2}{v^2}, \quad \lambda_{h^3} = 3\frac{m_h^2}{v}, \quad \lambda_{h^4} = 3\frac{m_h^2}{v^2}. \tag{1.12}$$

The SM Higgs boson decays mainly to b-quark pairs (Figure 1.1). However, the $b\bar{b}b\bar{b}$ channel in Higgs pair production is plagued by huge backgrounds making rare decays more feasible. For instance the decay into a b-quark pair and two photons or a b-quark pair and two τ leptons are studied. Currently, the CMS detector provides the most accurate results for Higgs pair production in the $HH \to bb\gamma\gamma$ channel with bounds of $-8\lambda_{h^3}^{SM} < \lambda_{h^3}^{SM} < 15\lambda_{h^3}^{SM}$ for the trilinear coupling [172]. An ATLAS study predicts to narrow down the exclusion values for the $HH \to bb\gamma\gamma$ channel with an integrated luminosity of 3000 fb^{-1} to $-0.8\lambda_{h^3}^{SM} < \lambda_{h^3} < 7.7\lambda_{h^3}^{SM}$ as can be reached at the HL-LHC [173]. These results are based on the assumption among others that beyond Standard Model effects originate only from modifications of the trilinear self-coupling. These result require an accurate knowledge of the production cross sections so that the full NLO effects are indispensable. An alternative approach to the direct search for Higgs pairs are the indirect effects using the dependence of single Higgs boson processes on λ_{h^3} via loop effects. Since the single Higgs cross section is larger than the one of Higgs boson pair production, the methods can be used for the data gathered at recent and current colliders. It is, however, a model dependent approach. This method was first used in a study at an e^+e^- collider for ZH production where the λ_{h^3} dependence arises at NLO level [175]. More recently,

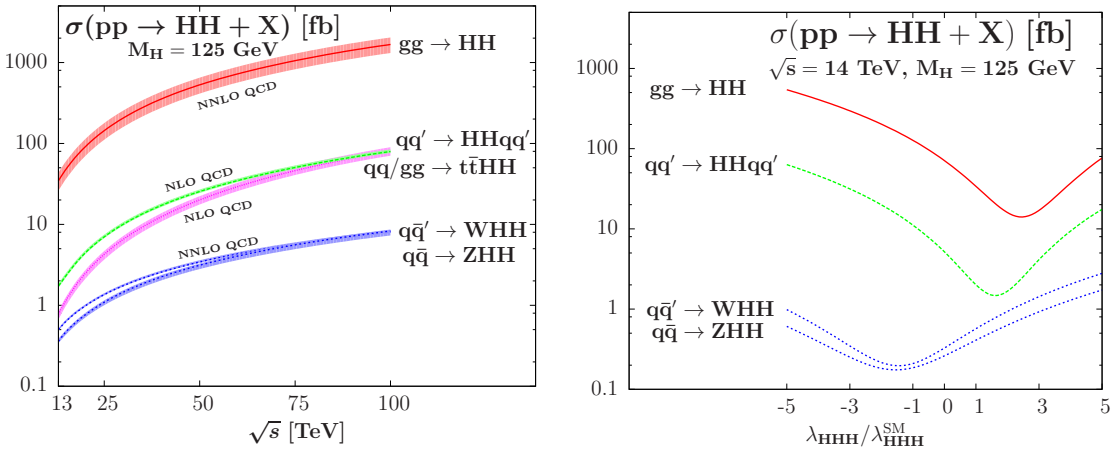

Figure 1.6: Left: Higgs boson pair production cross sections as a function of the center of mass energy for the different production channels. The theoretical uncertainties are represented by the bands [174]. Right: Production cross sections as a function of the trilinear coupling normalized to the SM self-coupling [138].

the method has been applied to Higgs boson production and decay via gluon fusion and vector boson fusion at the LHC [176–178]. Furthermore, the method has been extended to precision observables such as the W boson mass and the effective sine of the Weinberg angle which are at two-loop level λ_{h^3}-dependent. The exclusions limits obtained from those observations are comparable to the current ones from direct searches for Higgs pair production [179, 180].

1.3 Previous Work

In 1998 the virtual and real NLO QCD corrections to Higgs pair production via gluon fusion were calculated in the large top mass limit leading to an increase of the cross section by about a factor 2 [181]. Later the calculation was improved by adding a large top mass expansion of the inclusive cross section. Additional 10% NLO mass effects were obtained [182]. However, depending on the definition of the large top mass expansion on top of the massive LO expression, it was not clear whether it leads to an increase or decrease of 10% in the cross section [183]. The calculation of the full NLO mass effects for the real corrections yielded a correction of -10% [151, 170]. In parallel to our work, there was another group calculating the NLO QCD corrections including the full top mass dependence as well. They obtained a decrease in the total cross section of 14% for a center of mass energy of 13 TeV [184, 185]. Further, the NNLO QCD corrections in the heavy-top limit were added to the NLO results [183, 186, 187] and the NNLL soft and collinear gluon resummation

was computed [188]. For the vector-boson fusion the NLO [138, 170] and NNLO [189] QCD corrections are calculated. They amount to about 10% at the NLO and less than a per-cent at NNLO. For double Higgs-strahlung they are known at NLO [170] and NNLO [138] while for double Higgs bremsstrahlung off top-quarks they are calculated up to the NLO level [170].

1.4 Topic of this Thesis

The aim of this thesis is the calculation of the full NLO QCD corrections to Higgs pair production via gluon fusion including all mass effects in the context of the SM. Since gluon fusion is a loop-induced process at LO, the calculation of the virtual NLO corrections constitutes a two-loop calculation of a two-to-two process containing massive and massless particles in the loops. This leads to ultraviolet (UV) and infrared (IR) divergent NLO amplitudes. At the present time, there is no systematic method of how to perform such a calculation analytically. Our approach is based on a former unpublished numerical method used in the calculation of the single Higgs NLO corrections [55, 82].

Chapter 2 starts with a basic introduction about the calculation of the cross section. This is followed by a section about the leading-order calculation (Section 2.1) and Section 2.2 about the virtual corrections. The latter is split into of the calculation of the box diagrams, the one-particle-reducible diagrams, the triangular diagrams, the renormalization, the finite virtual corrections and their numerical evaluation. Further, Section 2.3 explains the real corrections consisting of the recalculation of the heavy-top limit results and the massive calculation. In Chapter 3 the results are discussed including the differential cross section and the total hadronic cross section.

Chapter 2

Higgs pair production

High energy collisions of hadrons can be characterized by the constituents of the hadronic bound states, the partons. The QCD factorization theorem [190] predicts the division of processes into short-distance and long-distance parts in infinite momentum frames. The first one contains the hard parton scattering described by perturbation theory. It is independent of the external hadrons. The long-distance part is described by parton distribution functions (PDF). These are independent of the hard-scattering process and contain the properties of the external hadrons. The PDFs can be obtained for instance from fits to experimental data of deep inelastic scattering experiments. Both parts are brought together by the factorization scale μ_F describing the scale down to which the perturbative description holds. Therefore the LO hadronic cross section of two protons scattering to a Higgs pair via two gluons can be written as

$$\sigma(pp \to gg \to hh) = \int_0^1 \mathrm{d}x_1 \mathrm{d}x_2 f_g(x_1, \mu_F) f_g(x_2, \mu_F) \hat{\sigma}\left(g(p_1)g(p_2) \to hh\right) \tag{2.1}$$

where $\hat{\sigma}$ is the perturbative partonic cross section and $f_g(x_i, \mu_F)$ the non-perturbative parton distribution functions depending on the gluon momentum fraction x_i of the proton. The latter can be interpreted as the probability density to find a gluon with momentum fraction x_i in the proton. The NLO cross section σ_{NLO} can be split into the LO cross section σ_{LO}, the virtual corrections $\Delta\sigma_{virt}$ and the real corrections $\Delta\sigma_{real}$. Since the LO cross-section is already a loop-induced process the virtual corrections are two-loop contributions and the real corrections are one-loop contributions. The virtual corrections consist of triangular and box loops mediated by top and bottom quarks. We denote processes with two incoming and one outgoing particle from the quark loop as triangular diagrams and processes with two incoming and two outgoing particles as box diagrams (see Figure 2.1). The real corrections are distinguished by their initial states. There can be either two gluons, a gluon and a (anti-)quark

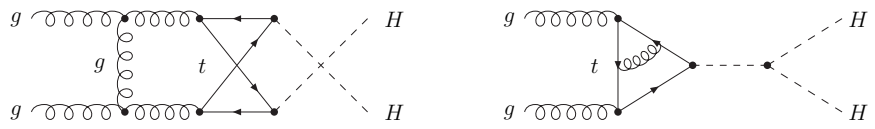

Figure 2.1: Example Feynman diagrams for a box (left) and a triangular (right) contribution.

or a quark and an antiquark in the initial state. The individual corrections can be expressed in the following compact form [181]:

$$\sigma_{NLO}\left(pp \to HH + X\right) = \sigma_{LO} + \Delta\sigma_{virt} + \Delta\sigma_{gg} + \Delta\sigma_{gq} + \Delta\sigma_{q\bar{q}}, \tag{2.2}$$

with

$$\begin{aligned}
\sigma_{LO} &= \int_{\tau_0}^{1} \mathrm{d}\tau \frac{\mathrm{d}\mathcal{L}^{gg}}{\mathrm{d}\tau} \hat{\sigma}_{LO}\left(Q^2 = \tau s\right), \\
\Delta\sigma_{virt} &= \frac{\alpha_s(\mu)}{\pi} \int_{\tau_0}^{1} \mathrm{d}\tau \frac{\mathrm{d}\mathcal{L}^{gg}}{\mathrm{d}\tau} \hat{\sigma}_{LO}\left(Q^2 = \tau s\right) C, \\
\Delta\sigma_{gg} &= \frac{\alpha_s(\mu)}{\pi} \int_{\tau_0}^{1} \mathrm{d}\tau \frac{\mathrm{d}\mathcal{L}^{gg}}{\mathrm{d}\tau} \int_{\frac{\tau_0}{\tau}}^{1} \frac{\mathrm{d}z}{z} \hat{\sigma}_{LO}\left(Q^2 = z\tau s\right) \Bigg\{ - zP_{gg}(z)\log\frac{\mu_F^2}{\tau s} \\
&\qquad + d_{gg}(z) + 6[1 + z^4 + (1-z)^4] \left(\frac{\log(1-z)}{1-z}\right)_+ \Bigg\}, \\
\Delta\sigma_{gq} &= \frac{\alpha_s(\mu)}{\pi} \int_{\tau_0}^{1} \mathrm{d}\tau \sum_{q,\bar{q}} \frac{\mathrm{d}\mathcal{L}^{gq}}{\mathrm{d}\tau} \int_{\frac{\tau_0}{\tau}}^{1} \frac{\mathrm{d}z}{z} \hat{\sigma}_{LO}\left(Q^2 = z\tau s\right) \\
&\qquad \Bigg\{ - \frac{z}{2} P_{gq}(z)\log\frac{\mu_F^2}{\tau s(1-z)^2} + d_{gq}(z) \Bigg\}, \\
\Delta\sigma_{q\bar{q}} &= \frac{\alpha_s(\mu)}{\pi} \int_{\tau_0}^{1} \mathrm{d}\tau \sum_{q,\bar{q}} \frac{\mathrm{d}\mathcal{L}^{q\bar{q}}}{\mathrm{d}\tau} \int_{\frac{\tau_0}{\tau}}^{1} \frac{\mathrm{d}z}{z} \hat{\sigma}_{LO}\left(Q^2 = z\tau s\right) d_{q\bar{q}}(z),
\end{aligned} \tag{2.3}$$

where μ_F is the factorization scale, $\tau_0 = 4m_h^2/S$, S the hadronic center of mass energy squared and Q^2 is the invariant Higgs pair mass,

$$Q^2 = m_{hh}^2. \tag{2.4}$$

LO mass effects are included in the LO partonic cross section $\hat{\sigma}_{LO}$. The quark masses affect only the C and the d_{ij} functions at NLO. In the heavy-top limit they approach

the following concise expressions

$$
\begin{aligned}
C &\to \pi^2 + \frac{11}{2} + \frac{33 - 2N_F}{6}\log\left(\frac{\mu_R^2}{Q^2}\right) + C_{\Delta\Delta}, \\
d_{gg} &\to -\frac{11}{2}(1-z)^3, \\
d_{gq} &\to \frac{2}{3}z^2 - (1-z)^2, \\
d_{q\bar{q}} &\to \frac{32}{27}(1-z)^3.
\end{aligned}
$$

$C_{\triangle\triangle}$ are the NLO mass effects from the one-particle reducible diagrams (Figure 2.2)

$$
C_{\triangle\triangle} = \mathrm{Re}\frac{\int_{\hat{t}_-}^{\hat{t}_+} \mathrm{d}\hat{t}\left\{\frac{4}{9}(\mathrm{C}_\triangle \mathrm{F}_\triangle + \mathrm{F}_\square) - \frac{4}{9}\frac{\mathrm{p}_\mathrm{T}^2}{2\hat{t}\hat{u}}(\mathrm{Q}^2 - \mathrm{m}_1^2 - \mathrm{m}_2^2)^2 \mathrm{G}_\square\right\}}{\int_{\hat{t}_-}^{\hat{t}_+} \mathrm{d}\hat{t}\{|\mathrm{C}_\triangle \mathrm{F}_\triangle + \mathrm{F}_\square|^2 + |\mathrm{G}_\square|^2\}} \tag{2.5}
$$

with

$$
\begin{aligned}
C_\triangle &= \frac{3m_h^2}{Q^2 - m_h^2}, \\
\hat{t} &= -\frac{1}{2}\left[Q^2 - m_1^2 - m_2^2 - \sqrt{\lambda(Q^2, m_1^2, m_2^2)}cos\theta\right], \\
\hat{u} &= -\frac{1}{2}\left[Q^2 - m_1^2 - m_2^2 + \sqrt{\lambda(Q^2, m_1^2, m_2^2)}cos\theta\right],
\end{aligned}
$$

and the integration limit

$$
\hat{t}_\pm = -\frac{1}{2}\left[Q^2 - m_1^2 - m_2^2 \mp \sqrt{\lambda(Q^2, m_1^2, m_2^2)}\right],
$$

$F_{\triangle,\square}$ the corresponding spin-0 form factors and $G_\square$ the corresponding spin-2 form factor. Further m_1 and m_2 are the masses of the two Higgs bosons. The Mandelstam variables are defined as

$$
\begin{aligned}
s &= (q_1 + q_2)^2 = (p_1 + p_2)^2, \\
t &= (p_1 - q_1)^2 = (p_2 - q_2)^2, \\
u &= (p_1 - q_2)^2 = (p_2 - q_1)^2,
\end{aligned} \tag{2.6}
$$

where q_i are the momenta of the gluons and p_i the momenta of the two Higgs bosons. Further we use the modified Mandelstam variables

$$
\begin{aligned}
t_1 &= t - p_1^2 = -2p_1q_1, \\
u_1 &= u - p_1^2 = -2p_1q_2,
\end{aligned} \tag{2.7}
$$

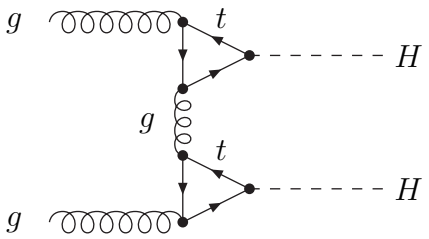

Figure 2.2: Feynman diagram for the one-particle-reducible contribution.

and the ratios

$$\rho_s = \frac{s}{m_t^2}, \quad \rho_t = \frac{t_1}{m_t^2}, \quad \rho_u = \frac{u_1}{m_t^2}, \quad \rho_h = \frac{m_h^2}{m_t^2}. \tag{2.8}$$

The perturbative description of QCD leads to divergences in higher order calculations. One distinguishes between divergences caused through large momenta in the loop, ultra-violet divergences (UV), and infrared divergences (IR) if the momentum of a real or virtual particle becomes small, or collinear divergencies (COLL) through the radiation of a massless particle by a massless particle. These divergences have to be separated from the finite parts and cancelled to be able to perform higher order calculations. For the IR divergences this can be achieved by using conventional dimensional regularization [19]. This is a gauge and Lorentz invariant regularization scheme. A dimensional regulator ϵ is introduced to reduce the space-time dimension by a small amount $D = 4 - 2\epsilon$. An arbitrary scale μ is introduced to preserve the dimension of the amplitude.

The following part of this chapter is about the methods used to derive the amplitudes of the individual contributions to the NLO cross section and the extraction of the divergences of those. In the first section the LO cross section is derived followed by a section about the calculation of the finite part of the virtual corrections. This is complemented by a last section about the real correction.

2.1 Leading-Order Cross Section

The total leading-order cross section σ_{LO} in the perturbative expansion of the strong coupling is obtained by the integration over the partonic LO cross section and the

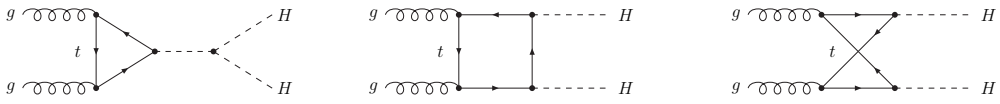

(a) (b) (c)

Figure 2.3: LO Feynman diagrams for the three possible topologies of gluon fusion.

PDF functions (see Equation (2.1)),

$$\sigma_{LO}(pp \to gg \to hh) = \int_{\tau_0}^{1} \mathrm{d}\tau \frac{d\mathcal{L}^{gg}}{d\tau} \hat{\sigma}_{LO}(s = \tau S) \tag{2.9}$$

where S is the hadronic energy squared and $\tau_0 = \frac{4m_h^2}{S}$. The PDF functions have been included in the gluon luminosity $\mathcal{L}^{gg}$,

$$\frac{d\mathcal{L}^{gg}}{d\tau} = \int_{\tau}^{1} \frac{\mathrm{d}x}{x} f_g(x, \mu_F) f_g(\tau/x, \mu_F). \tag{2.10}$$

The LO partonic cross section can be calculated from the LO matrix element by integration over the two-particle phase space $\mathrm{d}\Phi_2$,

$$\hat{\sigma}_{LO}(s) = \frac{1}{2}\frac{1}{2s} \int \mathrm{d}\Phi_2 \overline{|\mathcal{M}_{LO}|}^2 \tag{2.11}$$

where s denotes the squared partonic center of mass energy. The factor $1/2$ originates from the symmetry of the identical final state particles. The LO matrix element can be expressed using the gluon polarisation vectors ϵ_μ and ϵ_ν as

$$\mathcal{M}_{LO} = 2i \frac{(2\pi\mu)^{4-D}}{16\pi^2} \int \frac{\mathrm{d}^D k}{i\pi^2} \left[\mathcal{M}_{\triangle}^{\mu\nu} + \mathcal{M}_{\square}^{\mu\nu}\right] \epsilon_\mu(q_1)\epsilon_\nu(q_2) \tag{2.12}$$

where $\mathcal{M}_{\triangle}$ is the amplitude of the triangle diagrams (Figure 2.3(a)) and $\mathcal{M}_{\square}$ the amplitude of the box diagrams (Figures 2.3 (b) and (c)). The former can be obtained from the known single Higgs results by adding the triple Higgs vertex on the matrix element level. For the box diagram contributions two different generic diagrams have to be calculated. This calculation is performed in dimensional regularization with $D = 4 - 2\epsilon$. The matrix element can be divided into two process-independent Lorentz tensors $T_i^{\mu\nu}$ $(i = 1, 2)$ with two form factors that are Lorentz and gauge invariant. In general, the relation between the matrix element and $T^{\mu\nu}$ can be expressed as $\mathcal{M} = T^{\mu\nu}\epsilon_\mu(q_1)\epsilon_\nu(q_2)$ with $T^{\mu\nu} = f_{00}g^{\mu\nu} + \sum_{i,j=1}^{3} f_{ij} q_i^\mu q_j^\nu$. The Ward identities and the on-shell properties for the gluons constrain the coefficients f_{ij},

$$q_1^\mu T_{\mu\nu} = q_2^\nu T_{\mu\nu} = 0\,. \tag{2.13}$$

In the following, the form factor basis is chosen such that the Lorentz tensors are orthogonal in four dimensions,

$$
\begin{aligned}
T_1^{\mu\nu} &= g^{\mu\nu} - \frac{q_1^\nu q_2^\mu}{q_1 \cdot q_2}, \\
T_2^{\mu\nu} &= g^{\mu\nu} + \frac{(p_1 \cdot p_1)(q_1^\nu q_2^\mu)}{p_T^2 (q_1 \cdot q_2)} - \frac{2(q_2 \cdot p_1)(q_1^\nu p_1^\mu)}{p_T^2 (q_1 \cdot q_2)} - \frac{2(q_1 \cdot p_1)(q_2^\mu p_1^\nu)}{p_T^2 (q_1 \cdot q_2)} + \frac{2(p_1^\mu p_1^\nu)}{p_T^2},
\end{aligned} \tag{2.14}
$$

with the transverse momentum squared p_T^2 given by

$$
p_T^2 = 2\frac{(q_2 \cdot p_1)(q_1 \cdot p_1)}{q_1 \cdot q_2} - p_1 \cdot p_1 \,. \tag{2.15}
$$

In D dimensions, however, the orthogonality requirement does not hold anymore.

$$
\begin{aligned}
T_1^{\mu\nu} \cdot T_{1,\mu\nu} = T_2^{\mu\nu} \cdot T_{2,\mu\nu} &= (D-2), \\
T_1^{\mu\nu} \cdot T_{2,\mu\nu} &= (D-4).
\end{aligned} \tag{2.16}
$$

This means that the projectors onto form factors need to be adjusted. For this purpose, the property $P_i^{\mu\nu} T_{j,\mu\nu} = \delta_{i,j}$ with $i, j \in 1, 2$ has to hold. Choosing $P_i^{\mu\nu} = \sum_j a_{ij} T_j^{\mu\nu}$ leads to

$$
\begin{aligned}
P_1^{\mu\nu} &= \frac{(D-2)T_1^{\mu\nu} - (D-4)T_2^{\mu\nu}}{4(D-3)}, \\
P_2^{\mu\nu} &= \frac{(D-2)T_2^{\mu\nu} - (D-4)T_1^{\mu\nu}}{4(D-3)}.
\end{aligned} \tag{2.17}
$$

Summing up, the LO matrix element can thus be expressed in terms of the form factor as

$$
\mathcal{M}_{LO} = \frac{\alpha_s}{\pi}[(\mathcal{F}_\triangle + \mathcal{F}_1)P_1^{\mu\nu} + \mathcal{F}_2 P_2^{\mu\nu}]\delta_{ab}\epsilon_\mu(q_1)\epsilon_\nu(q_2). \tag{2.18}
$$

The form factors can be obtained using

$$
\frac{\alpha_s}{\pi}\mathcal{F}_\triangle = i\frac{(2\pi\mu)^{4-D}}{16\pi^2}\int \frac{\mathrm{d}^D k}{i\pi^2}\mathcal{M}_\triangle^{\mu\nu} \cdot P_{1,\mu\nu}, \tag{2.19}
$$

$$
\frac{\alpha_s}{\pi}\mathcal{F}_1 = i\frac{(2\pi\mu)^{4-D}}{16\pi^2}\int \frac{\mathrm{d}^D k}{i\pi^2}\mathcal{M}_\square^{\mu\nu} \cdot P_{1,\mu\nu}, \tag{2.20}
$$

$$
\frac{\alpha_s}{\pi}\mathcal{F}_2 = i\frac{(2\pi\mu)^{4-D}}{16\pi^2}\int \frac{\mathrm{d}^D k}{i\pi^2}\mathcal{M}_\square^{\mu\nu} \cdot P_{2,\mu\nu}. \tag{2.21}
$$

The second form factor of the triangle contribution vanishes since $\mathcal{M}_\triangle^{\mu\nu} \cdot P_{2,\mu\nu} = 0$. This leads to the following relation between the partonic cross section and the form factors

$$
\hat{\sigma}_{LO}(\hat{s}) = \frac{\alpha_s^2(\mu_R^2)}{1024\pi^3\hat{s}^2}\int_{\hat{t}_-}^{\hat{t}_+} \mathrm{d}\hat{t}\left(|\mathcal{F}_\triangle + \mathcal{F}_1|^2 + |\mathcal{F}_2|^2\right), \tag{2.22}
$$

$\lambda_{htt} = -i\frac{m_t}{v}$

$\lambda^{\mu}_{gtt} = -ig_s\gamma^{\mu}\frac{T^a}{2}$

$\lambda_{hhh} = -i\frac{3m_h^2}{v}$

$\Delta_t(q) = \frac{i(\not{q}+m_t)}{q^2-m_t^2}$

$\Delta_g^{\mu\nu}(q) = -i\frac{g^{\mu\nu}}{q^2}$

$\Delta_h(q) = \frac{i}{q^2-m_h^2}$

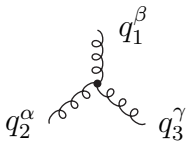

$$\Delta_{ggg}(q_1,q_2,q_3;\alpha,\beta,\gamma) = -g_s f^{\mathrm{abc}}[(q_2-q_1)^{\gamma}g^{\alpha\beta} + (q_1-q_3)^{\alpha}g^{\beta\gamma} + (q_3-q_2)^{\beta}g^{\gamma\alpha}]$$

Figure 2.4: Feynman rules used for the calculation of the gluon fusion cross section. The gluon propagator is defined in the Feynman gauge.

where μ_R is the renormalization scale. The integration limits resulting from the parametrization of the two-particle phase space are given by

$$\hat{t}_{\pm} = m_h^2 - \frac{s(1 \mp \beta)}{2}, \tag{2.23}$$

with $\beta = \sqrt{1-4m_h^2}s$.

For this calculation, the LO cross section has been calculated analytically in the narrow width approximation and numerically with all terms up to order $\mathcal{O}(\epsilon^2)$ for finite top quark widths. This was required since the analytical results in the literature are only valid in the narrow width approximation.

The matrix elements are calculated using the Feynman rules illustrated in Figure 2.4. This leads for the amplitudes of the two boxes $\mathcal{M}_1$ and $\mathcal{M}_2$ (Figure 2.3 (b) and (c)) to

$$\begin{aligned}
\mathcal{M}_1 &= \int \frac{\mathrm{d}^D k}{(2\pi)^D} \mathrm{Tr}\Big\{\lambda^{\nu}_{\mathrm{gtt}}\Delta_{\mathrm{t}}(\mathrm{k}+\mathrm{q}_1)\lambda^{\mu}_{\mathrm{gtt}}\Delta_{\mathrm{t}}(\mathrm{k})\lambda_{\mathrm{htt}}\Delta_{\mathrm{t}}(\mathrm{k}+\mathrm{p}_1)\lambda_{\mathrm{htt}}\Delta_{\mathrm{t}}(\mathrm{k}+\mathrm{q}_1+\mathrm{q}_2)\Big\}, \\
\mathcal{M}_2 &= \int \frac{\mathrm{d}^D k}{(2\pi)^D} Tr\Big\{\lambda^{\mu}_{gtt}\Delta_t(k)\lambda_{htt}\Delta_t(k+q_1+q_2-p_1)\lambda^{\nu}_{gtt}\Delta_t(k+q1-p_1)\lambda_{htt} \\
&\qquad \Delta_t(k+q_1)\Big\},
\end{aligned} \tag{2.24}$$

giving rise to tensor integrals in the loop momenta of the quark k.

A Feynman parametrization is performed to transform the denominator into a polynomial using Equation (2.25). For this purpose, a Feynman parameter $\hat{x}_i$ is

introduced for every propagator.

$$\frac{1}{a_1^{\alpha_1} a_2^{\alpha_2} \dots a_n^{\alpha_n}} = \frac{\Gamma(\alpha_1 + \dots + \alpha_n)}{\Gamma(\alpha_1) \cdots + \Gamma(\alpha_n))} \int_0^1 \mathrm{d}\hat{x}_1 \int_0^{1-\hat{x}_1} \mathrm{d}\hat{x}_2 \cdots \int_0^{1-\hat{x}_1-\cdots-\hat{x}_{n-2}} \mathrm{d}\hat{x}_{n-1} \frac{(1-\hat{x}_1-\cdots-\hat{x}_{n-1})^{\alpha_1-1} \hat{x}_1^{\alpha_2-1} \cdots \hat{x}_{n-1}^{\alpha_n-1}}{[a_1(1-\hat{x}_1-\cdots-\hat{x}_{n-1}) + a_2\hat{x}_1 + \cdots + a_n\hat{x}_{n-1}]^{\sum \alpha_i}} . \tag{2.25}$$

In our case, we choose the propagator denominators a_i as

$$\begin{aligned} a_1 &= (k+q_1)^2 - m_t^2, \\ a_2 &= (k+q_1+q_2)^2 - m_t^2, \\ a_3 &= (k+p_1)^2 - m_t^2, \\ a_4 &= k^2 - m_t^2 \end{aligned} \tag{2.26}$$

for $\mathcal{M}_1$ and

$$\begin{aligned} a_1 &= (k+q_1)^2 - m_t^2, \\ a_2 &= (k+q_1-p_1)^2 - m_t^2, \\ a_3 &= (k+p_2)^2 - m_t^2, \\ a_4 &= k^2 - m_t^2 \end{aligned} \tag{2.27}$$

for $\mathcal{M}_2$. A proper substitution is performed to obtain integrals from 0 to 1 since the numerical integration routine requires those boundaries. In the case of $\mathcal{M}_1$ we choose the following substitution.

$$\begin{aligned} \hat{x_1} &\to (1-x_1)(1-x_2) \\ \hat{x_2} &\to (1-x_1)x_2 \\ \hat{x_3} &\to x_1 x_3 \end{aligned} \tag{2.28}$$

and for $\mathcal{M}_2$

$$\begin{aligned} \hat{x_1} &\to x_1(1-x_2) \\ \hat{x_2} &\to (1-x_1)(1-x_3) \\ \hat{x_3} &\to (1-x_1)x_3 \end{aligned} \tag{2.29}$$

Further, a momentum shift Q_i is applied to transform the integral to the generic form of the left side of Equation (2.32),

$$\begin{aligned} k_\mu &\to k'_\mu = k_\mu - Q_i \\ Q_1 &= (1-x_1)q_1 + (1-x_1)x_2 q_2 + x_1 x_3 p_1 \\ Q_2 &= (1-x_1x_2)q_1 + (1-x_1)x_3 q_2 - (1-x_1)p_1 \end{aligned} \tag{2.30}$$

with the transformed mass terms

$$M_1^2 = m_t^2 - s(1-x_1)x_2 - m_h^2 x_1 x_3,$$
$$M_2^2 = m_t^2 - (1-x_1)(1-x_3)t_1 - (1-x_1)m_h. \tag{2.31}$$

The integral over the momentum-space variables k can then be evaluated using the following identities,

$$\begin{aligned}
\int \frac{\mathrm{d}^D k}{(2\pi)^D} \frac{1}{(k^2 - M^2 + i\bar{\epsilon})^N} &= i\frac{(-1)^N}{(4\pi)^{D/2}} \frac{\Gamma(N-\frac{D}{2})}{\Gamma(N)} \frac{1}{(M^2 - i\bar{\epsilon})^{N-\frac{D}{2}}} \\
\int \frac{\mathrm{d}^D k}{(2\pi)^D} \frac{k^2}{(k^2 - M^2 + i\bar{\epsilon})^N} &= \frac{i}{2}\frac{(-1)^{N-1}}{(4\pi)^{D/2}} \frac{\Gamma(N-1-\frac{D}{2})}{\Gamma(N)} \frac{D}{(M^2 - i\bar{\epsilon})^{N-1-\frac{D}{2}}} \\
\int \frac{\mathrm{d}^D k}{(2\pi)^D} \frac{k_\mu k_\nu}{(k^2 - M^2 + i\bar{\epsilon})^N} &= \frac{i}{2}\frac{(-1)^{N-1}}{(4\pi)^{D/2}} \frac{\Gamma(N-1-\frac{D}{2})}{\Gamma(N)} \frac{g_{\mu\nu}}{(M^2 - i\bar{\epsilon})^{N-1-\frac{D}{2}}}
\end{aligned} \tag{2.32}$$

In the case of $\mathcal{M}_i$ this results in the generic integrals

$$\begin{aligned}
\mathcal{I}_i &= \Gamma(4) \int \mathrm{d}\hat{\vec{x}} \int \frac{\mathrm{d}k}{(2\pi)} \frac{(1, k^2, k^4)}{(k^2 - R_i^2)^4} \\
&= i\frac{\Gamma(2+\epsilon)}{(4\pi)^2 m^4} \left(\frac{4\pi\mu^2}{m^2}\right)^\epsilon \int \mathrm{d}\hat{\vec{x}} \frac{\left(1; -\frac{2-\epsilon}{1+\epsilon}R_i^2; \frac{(2-\epsilon)(3-\epsilon)}{\epsilon(1+\epsilon)}R_i^4\right)}{N_i^{2+\epsilon}}
\end{aligned} \tag{2.33}$$

where the denominators N_i of the amplitudes are

$$\begin{aligned}
N_1 &= 1 - x_1(1-x_1)\left\{\rho_s x_2 x_3 + \rho_t x_2 + \rho_u x_3 + \rho_H\right\}, \\
N_2 &= 1 - x_1(1-x_1)\{\rho_s x_2 x_3 + \rho_t x_2 + \rho_u x_3 + \rho_h\},
\end{aligned} \tag{2.34}$$

and

$$R_i = Q_i^2 + M_i^2 \tag{2.35}$$

and $\mathrm{d}\vec{\hat{x}} = \mathrm{d}\hat{x}_1 \mathrm{d}\hat{x}_2 \mathrm{d}\hat{x}_3$. Singularities in the integration region emerge above the virtual threshold where $m_{hh}^2 > 4m_t^2$. In this region, the virtual top quarks can become on-shell causing imaginary parts of the integrals. An analytic continuation can be achieved by the replacement $m_t^2 \to m_t^2(1 - i\bar{\epsilon})$ where $\bar{\epsilon} \ll 1$. For small values of $\bar{\epsilon}$ the numerical integration over the three Feynman parameters causes numerical instabilities. This can be prevented by reducing the power of the denominator of the amplitude. This can be achieved with integration by parts w.r.t. one Feynman parameter, exemplified as

$$\int_0^1 \mathrm{d}x \, \frac{f(x)}{(a+bx)^3} = \frac{f(0)}{2a^2} - \frac{f(1)}{2(a+b)^2} + \int_0^1 \mathrm{d}x \, \frac{f'(x)}{2(a+bx)^2}. \tag{2.36}$$

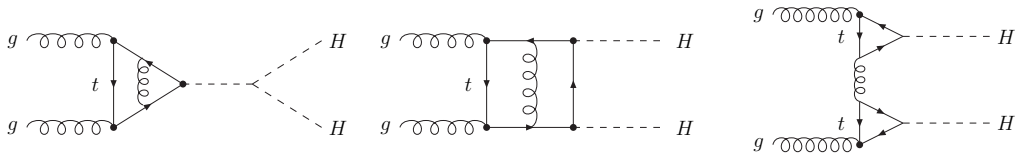

Figure 2.5: Example Feynman diagrams for the virtual corrections: a triangular, a box diagram and a one-particle reducible.

Fractions with polynomials of higher orders in the denominator can be integrated by parts using similar expressions. The choice of different Feynman parameters leads to different levels of stability. In the scope of this work it has not been investigated in detail what the optimal choice is. For both $\mathcal{M}_i$, we choose to integrate over x_2. The denominator can be written as a first order polynomial in this parameter $N_i = a+bx_2$. The integration by parts leads to

$$\int_0^1 \frac{\mathrm{d}x_2 H_i(x_2)}{N_i^{2+\epsilon}} = -\left.\frac{H_i(x_2)}{(1+\epsilon)bN_i^{1+\epsilon}}\right|_0^1 + \frac{1}{(1+\epsilon)b}\int_0^1 \mathrm{d}x_2 \frac{H_i'(x_2)}{N_i^{1+\epsilon}} \tag{2.37}$$

where H_i is the numerator of the matrix element $\mathcal{M}_i$.

For the analytic LO cross section we used the program HPAIR [181]. This is a Fortran based code calculating the NLO QCD corrections to Higgs pair production in the heavy-top limit in the SM and the minimal supersymmetric SM, while keeping the full mass dependence at LO.

2.2 Virtual Corrections

The virtual corrections to Higgs pair production can roughly be divided into three types of diagrams: triangular diagrams, one-particle reducible and box diagrams (Figure 2.5). The challenging part of this calculation are the box diagrams which are described in Section 2.2.1. This is followed by a section about the calculation of the one-particle reducible diagrams (Section 2.2.2), one about the triangular diagrams (Section 2.2.3), one about the renormalization (Section 2.2.4) and one about the finite part of the virtual corrections in Section 2.2.5. The final Section of this chapter explains the numerical evaluation of the integrals derived in the preceding sections.

2.2.1 Box Diagrams

The box diagrams are the most challenging contributions since they require the calculation of two-loop integrals with three kinematical parameter and mass ratios. First, the procedure to establish the amplitudes of such diagrams is described based on the unpublished method used in [55, 82]. Then this procedure is exemplified for a non-planar box diagram. For diagrams with an additional threshold the method had to be extended since they have a more involved singularity structure. We refer to those diagram as gluon rescattering contribution. There are 47 generic box diagrams which can be divided into six topologies with similar propagator structure. Topologies 1 to 5 are the diagrams for which the general method works, while the last topology contains the gluon rescattering diagrams. An overview of all the Feynman diagrams can be found in Appendix A.

The amplitude of a box diagram can generically be expressed as

$$\mathcal{M}^{ab}_{virt} = F_c \epsilon_\mu(q_1)\epsilon_\nu(q_2)\mu_R^{2(4-D)} \int \frac{\mathrm{d}^D q}{(2\pi)^D} \int \frac{\mathrm{d}^D k}{(2\pi)^D} \mathcal{M}^{\mu\nu} \tag{2.38}$$

where F_c is the color factor and ϵ_μ and ϵ_ν are the gluon polarization vectors. As for the LO matrix element, the virtual matrix element can be expressed in terms of the form factors as

$$\mathcal{M}_{virt} = \frac{\alpha_s^2}{\pi^2} \left[F_1 T_1^{\mu\nu} + F_2 T_2^{\mu\nu}\right] \delta_{ab} \epsilon_\mu(q_1)\epsilon_\nu(q_2). \tag{2.39}$$

The contraction of the matrix element with the projectors of Equation (2.17) leads to the expressions for the form factors. Those are integrals in the loop momenta of the gluons and quarks. Following the same procedure as for LO, a Feynman parametrization, where a Feynman parameter $\hat{x}_i$ is introduced for every propagator, is performed using Equation (2.25). This is followed by a proper substitution to obtain integrals from 0 to 1 since the numerical integration routine that was used requires those integration boundaries (see Section 2.2.6). A shift in the momentum leads to integral structures such that the integral over the momenta can be performed using Equation (2.32). Integrals with an odd power of the loop momentum in the numerator vanish.

The obtained scalar integral still cannot be integrated due to ultraviolet, collinear and infrared singularities. Below the virtual top mass threshold, there are UV and IR singularities at the endpoints of the integral and due to the Gamma functions UV singularities within the form factors. The ultraviolet singularities can be extracted using the suitable end-point subtractions. Thereby, the divergent part of the integral

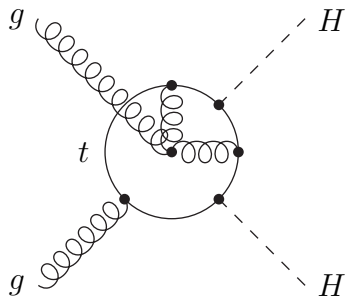

Figure 2.6: Non-planar diagram evaluated to exemplify the extraction of the singularities from the amplitudes.

is subtracted from the main integrand leading to a regular expression S_2. The term S_1 added back can be evaluated analytically since its numerator does not depend on the corresponding integrated variable any more. Generically this method is given by

$$\begin{aligned}\int_0^1 \mathrm{d}x\, \frac{f(x)}{(1-x)^{1-\epsilon}} &= \underbrace{\int_0^1 \mathrm{d}x\, \frac{f(1)}{(1-x)^{1-\epsilon}}}_{S_1} + \underbrace{\int_0^1 \mathrm{d}x\, \frac{f(x)-f(1)}{(1-x)^{1-\epsilon}}}_{S_2} \\ &= \frac{f(1)}{\epsilon} + \int_0^1 \mathrm{d}x\, \frac{f(x)-f(1)}{(1-x)} + \mathcal{O}(\epsilon). \end{aligned} \tag{2.40}$$

Further singularities in the integration region emerge above the virtual threshold where $m_{hh}^2 > 4m_t^2$. In this region, the virtual top quarks can become on-shell causing imaginary parts of the integrals. An analytic continuation is performed by the replacement $m_t^2 \to m_t^2(1 - i\bar{\epsilon})$ where $\bar{\epsilon} \ll 1$. For small values of $\bar{\epsilon}$ the numerical integration over the six Feynman parameters causes numerical instabilities. As in the LO calculation, this can be prevented with integration by parts w.r.t. one Feynman parameter (see Equation (2.36)).

Example 1: non-planar diagram

In the first example the method to extract the UV divergences is shown for the non-planar diagram in Figure 2.6. The matrix element can be built up using the Feynman rules in Figure 2.4 leading to

$$\begin{aligned}\mathcal{M} = \int \frac{\mathrm{d}k^D}{(2\pi)^D} \int \frac{\mathrm{d}q^D}{(2\pi)^D} Tr\Big\{ &\Delta_t(k+q)\lambda_{htt}\Delta_t(k+q+p_1)\lambda^{\sigma}_{gtt}\Delta_t(k+p_1-q_1) \\ &\lambda_{htt}\Delta_t(k+q_2)\lambda^{\nu}_{gtt}\Delta_t(k)\lambda^{\rho}_{gtt}\lambda_{ggg}(q,q_1,-(q+q_1);\rho,\mu,\sigma)\Big\}, \end{aligned} \tag{2.41}$$

where k and q are the loop-momenta of the quark and gluon in the loops. This matrix element contains only UV singularities. There are no IR singularities.

A Feynman parametrization is performed as described in Equation (2.25) introducing six Feynman parameters $\hat{x_i}, i = 1, ..., 6$. The propagator denominators a_i of Equation (2.25) are chosen for the integral over the first loop-momentum k as

$$\begin{aligned} a_1 &= (k+q)^2 - m_t^2, \\ a_2 &= (k+q+p_1)^2 - m_t^2, \\ a_3 &= (k-q_1+p_1)^2 - m_t^2, \\ a_4 &= (k+q_2)^2 - m_t^2, \\ a_5 &= k^2 - m_t^2, \end{aligned} \tag{2.42}$$

and for the integral over the second loop-momentum q as

$$\begin{aligned} \tilde{a}_1 &= N_1, \\ \tilde{a}_2 &= q^2 + 2qq_1, \\ \tilde{a}_3 &= q^2, \end{aligned} \tag{2.43}$$

where N_1 is the denominator of the amplitude after integrating over the loop-momentum k. The following substitution is performed to obtain integrals from 0 to 1 of the Feynman parameters

$$\begin{aligned} &\hat{x}_1 \to (1-x_1)(1-x_2), \quad \hat{x}_2 \to (1-x_1)x_2, \quad \hat{x}_3 \to x_1(1-x_3), \\ &\hat{x}_4 \to x_1x_3x_4, \quad \hat{x}_5 \to x_5, \quad \hat{x}_6 \to (1-x_5)x_6 \end{aligned} \tag{2.44}$$

Further a shift in both loop momenta is performed to obtain integrals of the form as in Equation (2.32),

$$k^\mu \to k'^\mu = k^\mu - Q_1, \tag{2.45}$$

$$q^\mu \to q'^\mu = q^\mu - Q_2, \tag{2.46}$$

with

$$\begin{aligned} Q_1 &= (1-x_1)q - x_1(1-x_3)q_1 + x_1x_3x_4q_2 + [(x_2(1-x_1) + x_1(1-x_3))]p_1, \\ Q_2 &= [x_5(1-x_3) - x_6(1-x_5)]q_1 - x_3x_4x_5q_2 - (1-x_2-x_3)x_5p_1. \end{aligned}$$

After these manipulations the remaining Feynman integrals acquire the following general structure

$$S = \int_0^1 \mathrm{d}\vec{x}\, G \frac{x_1^{2+\epsilon}\,(1-x_1)^{1+\epsilon}\,x_3\,(1-x_5)}{x_5^{1+\epsilon} N^{3+2\epsilon}(\vec{x})} H\,(\vec{x}) \tag{2.47}$$

G contains all the factors which are not relevant for the singularity structure and H is the numerator of the matrix element depending on the Feynman parameters $\vec{x}_i$ $(i = 1, ..., 6)$. The denominator N has the following structure

$$\begin{aligned}
N &= 1 - c_1\rho_s + c_2\rho_t - c_3\rho_u + c_4\rho_h, \\
c_1 &= x_1(1-x_1)[x_5(1-x_3) + x_6(1-x_5)]x_3x_4 + x_1^2x_3x_4(1-x_3), \\
c_2 &= x_1(1-x_1)[x_5(1-x_3) + x_6(1-x_5)](1-x_2-x_3) + x_1(1-x_3)[x_2(1-x_1) \\
&\quad + x_1(1-x_3) - 1], \\
c_3 &= x_3x_4x_5(1-x_1)x_1(1-x_2-x_3) + x_1x_3x_4[x_2(1-x_1) + x_1 + (1-x_3)], \\
c_4 &= x_1(1-x_1)x_3(1-x_2-x_3)^2 + [x_2(1-x_1) + x_1(1-x_3)][x_2(1-x_1) \\
&\quad + x_1(1-x_3) - 1].
\end{aligned} \tag{2.48}$$

For this diagram the singularity appears as x_5 is approaching zero. This can be regularized using endpoint subtractions as explained in the last section. The subtraction term is in this case the original integrand with vanishing x_5. This leads to the following expression

$$\begin{aligned}
S &= \int_0^1 \mathrm{d}\vec{x}\, \frac{1}{x_5^{1+\epsilon}} \frac{\tilde{H}\,(\vec{x})}{N^{3+2\epsilon}(\vec{x})} \\
&= \underbrace{\int_0^1 \mathrm{d}\vec{x}\, \frac{1}{x_5^{1+\epsilon}} \left\{ \frac{\tilde{H}\,(\vec{x})}{N^{3+2\epsilon}(\vec{x})} - \frac{\tilde{H}(\vec{x}; x_5 = 0)}{N(\vec{x}; x_5 = 0)^{3+2\epsilon}} \right\}}_{S_1} + \underbrace{\int_0^1 \mathrm{d}\vec{x}\, \frac{1}{x_5^{1+\epsilon}} \frac{\tilde{H}\,(\vec{x}; x_5 = 0)}{N(\vec{x}; x_5 = 0)^{3+2\epsilon}}}_{S_2}
\end{aligned} \tag{2.49}$$

with the abbreviation

$$\tilde{H}\,(\vec{x}) = G x_1^{2+\epsilon}(1-x_1)^{1+\epsilon} x_3(1-x_5) H\,(\vec{x})\,. \tag{2.50}$$

Further, we introduce the notation $F(\vec{x}; x_i = 0)$ where the boundary condition $x_i = 0$ is imposed[1]. S_1 is a regular integral in x_5 and can be expanded in ϵ while S_2 can be integrated analytically over x_5. Explicitly, we have

$$\begin{aligned}
S_1 = \int_0^1 \mathrm{d}\vec{x} \frac{1}{x_5} \Bigg[& \frac{H(\vec{x})(1-x_5)}{N^3(\vec{x})} \left\{ 1 - \epsilon 2\log(\sqrt{x_5}N(\vec{x})) + \frac{\epsilon^2}{2} 4\log^2(\sqrt{x_5}N(\vec{x})) \right\} \\
& - \frac{H(\vec{x}; x_5 = 0)(1-x_5)}{N^3(\vec{x}; x_5 = 0)} \left\{ 1 - \epsilon 2\log(\sqrt{x_5}N(\vec{x}; x_5 = 0)) + \frac{\epsilon^2}{2} 4\log^2(\sqrt{x_5}N(\vec{x}; x_5 = 0)) \right\} \Bigg]
\end{aligned} \tag{2.51}$$

[1]Later, this notation is generalized to other boundary conditions

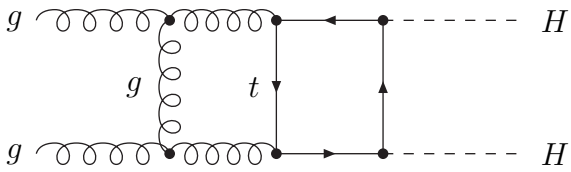

Figure 2.7: Gluon rescattering diagram to exemplify the method to extract the divergences from the amplitude for a process with two thresholds.

and

$$S_2 = -\int_0^1 \mathrm{d}\vec{x}\, \frac{H(\vec{x}; x_5 = 0)}{N^3(\vec{x}; x_5 = 0)} \left\{ \frac{1}{\epsilon} - 2\log(N(\vec{x}; x_5 = 0)) + \frac{\epsilon}{2} 4\log^2(N(\vec{x}; x_5 = 0)) \right\} \tag{2.52}$$

In summary, we were able to divide the divergent integral S into two parts S_1 and S_2 such that the divergent parts were extracted and regular integrals in x_5 were left over.

Example 2: Gluon rescattering diagram

In this section the extraction of the IR and collinear singularities of the gluon rescattering amplitude of the diagram illustrated in Figure 2.7 is described. Those are particularly challenging to calculate since they have an additional threshold where the invariant double Higgs mass exceeds zero: $M_{hh}^2 > 0$. In this case a modified subtraction terms is needed to extract the divergences.

The Feynman rules (Figure 2.4) lead to the following expression for the amplitude

$$\mathcal{M} = \int \frac{\mathrm{d}k^n \mathrm{d}q^n}{(2\pi)^{2n}} Tr\big\{ \Delta_t(k - q_1) \lambda_{htt} \Delta_t(k - q_1 + p_1) \lambda_{htt} \Delta_t(k + q_2) \lambda^{\sigma}_{gtt} \Delta_t(k + q) \lambda^{\rho}_{gtt} \big\}$$
$$\lambda_{ggg}(q, q_1, -(q + q_1); \tau, \mu, \rho) \lambda_{ggg}(-q, q_2, q - q_2; \tau, \nu, \sigma). \tag{2.53}$$

As in the preceding example, the form factors are obtained by applying the proper projectors on the matrix element. A Feynman parametrization is performed introducing six Feynman parameters x_i, $i = 1, ..., 6$. The propagator denominators a_i of

Equation (2.25) are chosen for the integration over the first loop-momentum k as

$$\begin{aligned} a_1 &= (k+q)^2 - m_t^2, \\ a_2 &= (k+q_2)^2 - m_t^2, \\ a_3 &= (k+p_1-q_1)^2 - m_t^2, \\ a_4 &= (k-q_1)^2 - m_t^2, \end{aligned} \tag{2.54}$$

and for the integration over the second loop-momentum as

$$\begin{aligned} \tilde{a}_1 &= N_1, \\ \tilde{a}_2 &= q^2 + 2qq_1, \\ \tilde{a}_3 &= q^2 - 2qq_2, \\ \tilde{a}_4 &= q^2, \end{aligned} \tag{2.55}$$

where N_1 is the denominator of the amplitude after integrating over the loop-momentum k. The following substitution is used to obtain integrals from 0 to 1,

$$\hat{x}_1 \to 1 - x_1, \quad \hat{x}_2 \to x_1(1-x_2), \quad \hat{x}_3 \to x_1 x_2 x_3, \tag{2.56}$$

$$\hat{x}_4 \to x_4 x_5, \quad \hat{x}_5 \to 1 - x_5, \quad \hat{x}_6 \to (1-x_4) x_5 x_6 \tag{2.57}$$

Further, a momentum shift in the momenta q and k as described in the preceding example is performed.

$$\begin{aligned} k^\mu &\to k'^\mu = k^\mu - Q_1, \\ q^\mu &\to q'^\mu = q^\mu - Q_2, \end{aligned} \tag{2.58}$$

with

$$\begin{aligned} Q_1 &= (1-x_1)q - x_1 x_2 q_1 + x_1(1-x_2)q_2 + x_1 x_2 x_3 p_1, \\ Q_2 &= [x_4 x_5 x_2 + 1 - x_5]q_1 - [x_4 x_5 (1-x_2) - (1-x_4) x_5 x_6]q_2 - x_4 x_5 x_2 x_3 p_1. \end{aligned}$$

This leads to an expression of the following general structure,

$$S = \int_0^1 \mathrm{d}\vec{x} \quad \frac{x_1^{1+\epsilon}(1-x_1)^\epsilon x_2 x_4^{1+\epsilon+\alpha}(1-x_4) x_5^{-\epsilon}}{N^{3+2\epsilon}(\vec{x})} H(\vec{x}) \tag{2.59}$$

where $\mathrm{d}\vec{x}$ is an abbreviation of $\mathrm{d}x_1\mathrm{d}x_2\mathrm{d}x_3\mathrm{d}x_4\mathrm{d}x_5\mathrm{d}x_6$. The denominator N can be brought into the following form

$$\begin{aligned}
N &= x_4 - c_1\rho_s - c_2\rho_t - c_3\rho_u - c_4\rho_h, \\
c_1 &= x_1\Big\{x_1x_2(1-x_2)x_4 + (1-x_1)(1-x_5+x_4x_5x_2)[(1-x_4)x_6 + x_4(1-x_2)]\Big\}, \\
c_2 &= x_1x_2x_3x_4\Big\{1 - x_1x_2 - (1-x_1)[x_2x_4x_5 + 1 - x_5]\Big\}, \\
c_3 &= x_1x_2x_3x_4\Big\{x_1(1-x_2) + (1-x_1)x_5[(1-x_4)x_6 + x_4(1-x_2)]\Big\}, \\
c_4 &= x_1x_2x_3x_4\Big\{1 - x_1x_2x_3 - (1-x_1)x_4x_5x_2x_3\Big\}.
\end{aligned} \tag{2.60}$$

The integral becomes singular if x_4 and c vanish simultaneously. In the following the auxiliary exponent α takes possible x_4 contributions from the matrix element into account.

For the infrared and collinear divergences the subtraction method has to be improved. The integral contains the denominator that is a second order polynomial $N = ax_4^2 + bx_4 + c$ in one of the Feymann parameters x_4. The coefficients a and c are of the order ρ_i $(i = s, t, u, h)$ and b of the order 1 in the heavy-top limit. From the calculation in the heavy-top limit it is known that only b and c contribute to the singularities. Since the singularity structure in the ratio to the Born term is universal, the same has to hold for the full mass dependent calculation as well. Thus one can construct a modified denominator N_0 which only depends on b and c. With this observation a subtraction term is constructed as

$$\begin{aligned}
S &= \int_0^1 \mathrm{d}\tilde{\vec{x}}\mathrm{d}x_4 \frac{x_4 H(\tilde{\vec{x}})}{N^{3+2\epsilon}(\vec{x})} \\
&= \int_0^1 \mathrm{d}\tilde{\vec{x}}\mathrm{d}x_4 \left\{ \underbrace{\left(\frac{x_4 H(\vec{x})}{N^{3+2\epsilon}(\vec{x})} - \frac{x_4 H(\vec{x}, x_4 = 0)}{N_0^{3+2\epsilon}(\vec{x})} \right)}_{S_1} + \underbrace{\frac{x_4 H(\vec{x}, x_4 = 0)}{N_0^{3+2\epsilon}(\vec{x})}}_{\tilde{S}_2} \right\}
\end{aligned} \tag{2.61}$$

with $N_0 = bx_4 + c$ and $\mathrm{d}\tilde{\vec{x}} = \mathrm{d}x_1\mathrm{d}x_2\mathrm{d}x_3\mathrm{d}x_5\mathrm{d}x_6$.

$$a = \mathcal{O}(\rho_i), b = 1 + \mathcal{O}(\rho_i), c = -\rho_s x_1(1-x_1)(1-x_5)x_6$$

The first subtracted term is regular and can be Taylor-expanded in ϵ. The integration over the Feynman parameter of the term added back can be performed which leads to

hypergeometric functions F and thus to an extraction of the divergences after using their transformation properties. The hypergeometric function is defined as

$$F(a,b;c;z) = \frac{\Gamma(c)}{\Gamma(b)\Gamma(c-b)} \int_0^1 \mathrm{d}t t^{b-1}(1-t)^{c-b-1}(1-zt)^{-a} \tag{2.62}$$

and has the following properties

$$\begin{aligned} F(a,0;c;z) &= 1 \\ F(a,b;c;z) &= \frac{\Gamma(c)\Gamma(b-a)}{\Gamma(b)\Gamma(c-a)}(-z)^{-a}F(a,1-c+a;1-b+a;z^{-1}) \\ &\quad + \frac{\Gamma(c)\Gamma(a-b)}{\Gamma(a)\Gamma(c-b)}(-z)^{-b}F(b,1-c+b;1-a+b;z^{-1}). \end{aligned} \tag{2.63}$$

For the generic initial integral S the divergent part is subtracted resulting in a regular term called S_1

$$S_1 = \int_0^1 \mathrm{d}\vec{x}\, x_1 x_2 x_4^{1+\alpha} \left\{ \frac{(1-x_4)H(\vec{x})}{N^3(\vec{x})} \left[\frac{x_1(1-x_1)x_4}{x_5 N^2(\vec{x})}\right]^\epsilon - \frac{H(\vec{x};x_4=0)}{N_0^3(\vec{x})} \left[\frac{x_1(1-x_1)x_4}{x_5 N_0^2(\vec{x})}\right]^\epsilon \right\} \tag{2.64}$$

that can be expanded in ϵ. For the term added back referred to as $\tilde{S}_2$ the integration over x_4 is performed using hypergeometric functions,

$$\begin{aligned} \tilde{S}_2 &= \int_0^1 \mathrm{d}\vec{x}\, x_1 x_2 x_4^{1+\alpha} \frac{H(\vec{x};x_4=0)}{N_0^3(\vec{x})} \left[\frac{x_1(1-x_1)x_4}{x_5 N_0^2(\vec{x})}\right] \\ &= \frac{\Gamma(2+\epsilon+\alpha)}{\Gamma(3+\epsilon+\alpha)} \int_0^1 \mathrm{d}\vec{x}_0 \frac{x_1^{1+\epsilon}(1-x)^\epsilon x_2 x_5^{-\epsilon}}{c^{3+2\epsilon}} F(3+2\epsilon, 2+\epsilon+\alpha; 3+\epsilon+\alpha; -\frac{b}{c}) \\ &\qquad H(\vec{x};x_4=0) \end{aligned} \tag{2.65}$$

A transformation in the argument of the hypergeometric function provides an extraction of the divergences. Using the identities in Equation (2.63) we arrive at

$$\begin{aligned} \tilde{S}_2 = \int_0^1 \mathrm{d}\tilde{x}\, \frac{x_1^{1+\epsilon}(1-x_1)^\epsilon x_2}{x_5^\epsilon} \Big\{ &\frac{\Gamma(-1-\epsilon+\alpha)}{\Gamma(-\epsilon+\alpha)} \frac{F(3+2\epsilon, 1+\epsilon-\alpha; 2+\epsilon-\alpha; -\frac{c}{b})}{b^{3+2\epsilon}} \\ &+ \frac{\Gamma(1+\epsilon-\alpha)\Gamma(2+\epsilon+\alpha)}{\Gamma(3+2\epsilon)} \frac{1}{c^{1+\epsilon-\alpha} b^{2+\epsilon+\alpha}} \Big\} H(\vec{x};x_4=0) \end{aligned} \tag{2.66}$$

The second term is only singular if α is zero. Otherwise, the integrand can be expressed as logarithms of c resulting in regular integrals. Therefore, only the case for a vanishing α has to be investigated further. This corroborates that $H(\vec{x}, x_4 = 0)$

defines all related singularities, while terms of $\mathcal{O}(x_4)$ result in regular integrals. $\tilde{S}_2$ with α set to zero now reads

$$\tilde{S}_2 = \int_0^1 \mathrm{d}\tilde{x} x_1^{1+\epsilon}(1-x_1)^\epsilon x_2 x_5^{-\epsilon} H(\vec{x}; x_4 = 0)\Big\{ \underbrace{-\frac{F(3+2\epsilon, 1+\epsilon; 2+\epsilon; -\frac{c}{b})}{(1+\epsilon)b^{3+2\epsilon}}}_{S_2} \tag{2.67}$$

$$+ \underbrace{\frac{\Gamma(1+\epsilon)\Gamma(2+\epsilon)}{\Gamma(3+2\epsilon)} \frac{1}{c^{1+\epsilon}b^{2+\epsilon}}}_{\tilde{S}_3} \Big\} \tag{2.68}$$

S_2 is a regular integral and can thus be expanded in ϵ. The second term referred to as $\tilde{S}_3$ contains further singularities in x_5 and x_6. Here a simple endpoint subtraction can be applied. Using the following abbreviation

$$\tilde{H}(\vec{x}; x_4 = 0) = x_2 \frac{H(\vec{x}; x_4 = 0)}{b^{2+\epsilon}(1-x_1)} \tag{2.69}$$

the integral $\tilde{S}_3$ can be decomposed as

$$\begin{aligned} \tilde{S}_3 &= (-\rho_s)^{-1-\epsilon} \int_0^1 \mathrm{d}\tilde{x} x_5^{-\epsilon}(1-x_5)^{-1-\epsilon} x_6^{-1-\epsilon} \tilde{H}(\vec{x}; x_4 = 0) \\ &= (-\rho_s)^{-1-\epsilon} \left[S_3 + S_4 + S_5 + S_6\right] \end{aligned} \tag{2.70}$$

A subtraction term for each of the singularities, where $x_5 \to 1$ or $x_6 \to 0$, is required. A further term has to be added back to compensate for the double counting of the point where $(x_5 \to 1)$ or $(x_6 \to 0)$ simultaneously. The S_3 term contains now regular integrals

$$\begin{aligned} S_3 = \int_0^1 \frac{\mathrm{d}\tilde{x}}{x_5^\epsilon (1-x_5)^{1+\epsilon} x_6^{1+\epsilon}} \Big\{ &\tilde{H}(x_1, x_2, x_3, 0, x_5, x_6) + \tilde{H}(x_1, x_2, x_3, 0, 1, 0) \\ &- \tilde{H}(x_1, x_2, x_3, 0, 1, x_6) - \tilde{H}(x_1, x_2, x_3, 0, x_5, 0) \Big\} \end{aligned} \tag{2.71}$$

The integration over x_6 of the first term added back leads to an explicit expression for S_4

$$S_4 = -\frac{1}{\epsilon} \int_0^1 \mathrm{d}x_1 \mathrm{d}x_2 \mathrm{d}x_3 \mathrm{d}x_5 \frac{\tilde{H}(\vec{x}; x_4 = 0, x_6 = 0) - \tilde{H}(\vec{x}; x_4 = 0, x_5 = 1, x_6 = 0)}{x_5^\epsilon (1-x_5)^{1+\epsilon}} \tag{2.72}$$

For the second term added back, S_5, the integration over x_5 is performed analytically,

$$S_5 = \frac{\Gamma^2(1-\epsilon)}{\Gamma(1-2\epsilon)} \int_0^1 \mathrm{d}x_1 \mathrm{d}x_2 \mathrm{d}x_3 \mathrm{d}x_6 \frac{\tilde{H}(\vec{x}; x_4 = 0, x_5 = 1) - \tilde{H}(\vec{x}; x_4 = 0, x_5 = 1, x_6 = 0)}{x_6^{1+\epsilon}} \tag{2.73}$$

while for the last term the integration over x_5 and over x_6 is performed,

$$S_6 = \frac{\Gamma^2(1-\epsilon)}{\epsilon^2\Gamma(1-2\epsilon)} \int_0^1 \mathrm{d}x_1\mathrm{d}x_2\mathrm{d}x_3 \tilde{H}(\vec{x}; x_4 = 0, x_5 = 1, x_6 = 1). \tag{2.74}$$

Finally, we arrive at an expression for S where all IR singularities are isolated as ϵ^{-1} and ϵ^{-2} poles,

$$S = \sum_{i=1}^{2} S_i + (-\rho_s)^{-1-\epsilon} \sum_{i=3}^{6} S_i \,. \tag{2.75}$$

2.2.2 One-Particle Reducible Diagrams

There are two one-particle reducible diagrams (Figure 2.2). They can either be calculated analytically or they can be derived from the known results of $H \to Z\gamma$. The analytical calculation has been published in [191]. The one-particle reducible diagrams consist of twice a two gluons-to-one-Higgs process connected by an off-shell gluon. The second approach uses the analytical results of $H \to Z\gamma$. The coupling coefficients have to be adjusted; the Z boson is replaced by the off-shell gluon and the photon by the on-shell gluon. In the case of the Higgs decaying into a photon and a Z boson, the partial decay width looks as follows [192, 193]:

$$\Gamma\left[H \to Z\gamma\right] = \frac{G_F^2 M_W^2 \alpha m_h^3}{64\pi^4} \left(1 - \frac{M_Z^2}{m_h^2}\right) \left| \sum_f A_f(\tau_f, \lambda_f) + A_W(\tau_W, \lambda_w) \right|^2 \tag{2.76}$$

where for $i = f$,W

$$\tau_i = \frac{4m_i^2}{m_h^2} \tag{2.77}$$

and

$$\lambda_i = \frac{4m_i^2}{m_Z^2} \,. \tag{2.78}$$

The form factor A_W describes the W boson loop contribution which can be disregarded since for the QCD corrections we only have to consider the fermion loop term A_f for the gluonic counter part

$$A_f(\tau, \lambda) = 2N_{cf} \frac{e_f(I_{3f} - 2e_f \sin^2\theta_w)}{\cos\theta_w} \left[I_1(\tau, \lambda) - I_2(\tau, \lambda)\right] \tag{2.79}$$

with the functions I_1 and I_2 defined as

$$I_1(\tau,\lambda) = \frac{\tau\lambda}{2(\tau-\lambda)} + \frac{\tau^2\lambda^2}{2(\tau-\lambda)^2}[f(\tau)-f(\lambda)] + \frac{\tau^2\lambda}{(\tau-\lambda)^2}[g(\tau)-g(\lambda)]\,, \tag{2.80}$$

$$I_2(\tau,\lambda) = \frac{\tau\lambda}{2(\tau-\lambda)}[f(\tau)-f(\lambda)]\,, \tag{2.81}$$

and

$$f(\tau) = \begin{cases} \arcsin^2\frac{1}{\sqrt{\tau}} & \tau \geq 1 \\ -\frac{1}{4}\left[\log\frac{1+\sqrt{1-\tau}}{1-\sqrt{1-\tau}} - i\pi\right] & \tau < 1\,, \end{cases}$$

$$g(\tau) = \begin{cases} \sqrt{\tau-1}\arcsin\frac{1}{\sqrt{\tau}} & \tau \geq 1 \\ \frac{\sqrt{1-\tau}}{2}\left[\log\frac{1+\sqrt{1-\tau}}{1-\sqrt{1-\tau}} - i\pi\right] & \tau < 1\,. \end{cases}$$

This result can be translated to the following "effective" Feynman rule for the Hgg^*-vertex

$$-i\frac{\alpha_s}{\pi v}\delta_{ab}(I_1-I_2)\left[q_2^\mu q_1^\nu - (q_1q_2)g^{\mu\nu}\right] \tag{2.82}$$

that is only valid for the quark-induced subdiagram of the Hgg^*-coupling. For the investigated process q_2 is chosen to be the momentum of the off-shell gluon. Using this Feynman rule one obtains the following expression for the matrix element,

$$\mathcal{M} = -i\left(\frac{\alpha_s}{\pi v}\right)\frac{\delta_{ab}}{2t}(I_1-I_2)^2\left\{sq^\mu q^\nu + t_1(q^\mu q_1^\nu - q_2^\mu q^\nu) - \frac{t_1^2}{2}g^{\mu\nu}\right\} \tag{2.83}$$

giving rise to an explicit expression for both form factors of the Higgs pair production,

$$F_j = -i\frac{g_s^4 m^2}{(4\pi)^4 v^2}\delta_{ab}4(I_1-I_2)^2 G_j \qquad (j=1,2) \tag{2.84}$$

with $G_1 = \rho_s$ and $G_2 = \frac{\rho_t\rho_u - \rho_s\rho_h}{\rho_t+\rho_h}$.

2.2.3 Triangular Diagrams

One has to consider twelve generic diagrams for the triangular case. As in the LO case, the known results of the single Higgs case can be used to obtain the partonic cross section contribution of the triangular diagrams. The QCD corrections of the triangular diagram only appear in the initial state involving the quark loop while the final-state $h^* \to hh$ splitting is of purely electroweak nature. Therefore, they are the same for single Higgs and for double Higgs production for a given Q^2. On the level of

the matrix element this means that the known virtual corrections C of single Higgs production can be used and only the LO matrix element has to be modified for Higgs pair production,

$$\mathcal{M}_{virt} = \mathcal{M}_{LO}[1 + C(Q^2)\frac{\alpha_s}{\pi}]. \tag{2.85}$$

2.2.4 Renormalization

The higher order virtual corrections lead to divergent results. To obtain the physical, finite correction a counter term has to be introduced such that the UV poles cancel. The IR and COLL singularities cancel against the real corrections. The counter terms are only defined up to finite terms that are defined the renormalization scheme. The scheme choice of these counter terms does not affect the physical quantities if calculated up to all orders in perturbation theory. However, calculations performed only up to finite order of perturbation theory lead to renormalization-scheme dependent results. The scale dependence of the input parameters can be used to estimate the theoretical uncertainties caused by the truncation of the perturbative series. All physical input parameters contributing to a process have to be renormalized. In our calculation these are the strong coupling constant α_s and the quark mass. Since the bottom-quark is neglected in this calculation, only the top-quark mass m_t has to be considered. The bare quantities $\alpha_{s,0}$ and $m_{t,0}$ have to be replaced by the renormalized quantities α_s and m_t and the counter terms $\delta\alpha_s$ and δm_t

$$\begin{aligned} \alpha_{s,0} &= \alpha_s + \delta\alpha_s, \\ m_{t,0} &= m_t + \delta m_t. \end{aligned} \tag{2.86}$$

At the level of the cross section, the virtual corrections can be decomposed into the loop-corrections $\delta\sigma_{virt}$ and the LO cross section σ_{LO} that is a function of the bare parameters. The perturbative expansion of the bare parameters in terms of the renormalized ones yields the counter term of the cross section,

$$\begin{aligned} \Delta\sigma_{virt} &= \sigma_{LO}(\alpha_{s,0}, m_{t,0}) + \delta\sigma_{virt} \\ &= \sigma_{LO}(\alpha_s, m_t) + \delta\sigma_{CT} + \delta\sigma_{virt}, \end{aligned} \tag{2.87}$$

where $\delta\sigma_{CT}$ is the counter term originating from $\delta\alpha_s$ and δm_t. Hence, the counter term can be expressed as

$$\delta\sigma_{CT} = \delta\alpha_s \frac{\partial\sigma_{LO}}{\partial\alpha_s} + \delta m_t \frac{\partial\sigma_{LO}}{\partial m_t} \tag{2.88}$$

where $\delta\alpha_s$ and δm_t denote the counter terms of the strong coupling constant and the top mass. In terms of the form factors $\mathcal{F}_i$ this corresponds to the counter term of the matrix element

$$\mathcal{M}^{CT} = \frac{\alpha_s^2}{\pi^2}\left[(\mathcal{F}_\triangle^{CT} + \mathcal{F}_1^{CT})T_1^{\mu\nu} + \mathcal{F}_2^{CT}T_2^{\mu\nu}\right]\delta_{ab}\epsilon_\mu^a(q_1)\epsilon_\mu^b(q_2). \tag{2.89}$$

The IR and COLL divergences cancel at the cross section level with the IR and COLL poles of the real corrections. In addition, a subtraction term can be constructed such that the IR divergences cancel for the virtual corrections alone, that is then added back to the real corrections thus resulting in finite virtual and real corrections separately. This subtraction term can be constructed from the results in the heavy quark limit since the relative IR singularity structure to the Born term is universal and therefore it is the same for the heavy quark mass limit and the full mass-dependent calculation. The subtraction term in the heavy-top limit is given by [181],

$$\delta_{HTL}F = \frac{\alpha_s}{\pi}\frac{\Gamma(1-\epsilon)}{\Gamma(1-2\epsilon)}\left(\frac{4\pi\mu^2}{-\bar{Q}^2}\right)^\epsilon\left\{\frac{3}{2\epsilon^2} + \frac{33-2N_F}{12\epsilon}\left(\frac{\mu^2}{-\bar{Q}^2}\right)^{-\epsilon} - \frac{11}{4} + \frac{\pi^2}{4}\right\}F_{LO} \tag{2.90}$$

with $\bar{Q}^2 = Q^2 + io$ and the abbreviation

$$\tilde{F}_{LO} = \Gamma(1+\epsilon)\left(\frac{4\pi\mu^2}{m_t^2}\right)^\epsilon F_{LO} \tag{2.91}$$

involving the full mass-dependent LO form factors F_{LO} derived in Section 2.1. The explicit transformation to the overall coefficients used in our calculation leads to

$$\begin{aligned}\delta_{HTL}F =& \frac{\alpha_s}{2\pi}\Gamma(1+\epsilon)\frac{\Gamma(1-\epsilon)}{\Gamma(1-2\epsilon)}\left(\frac{4\pi\mu^2}{m_t^2}\right)^\epsilon\left\{\frac{3}{\epsilon^2} + \frac{1}{\epsilon}\left[\frac{33-2N_F}{6} - 3\log\left(\frac{-Q^2}{m_t^2}\right)\right]\right.\\ &\left. - \frac{11}{2} + \frac{\pi^2}{2} + \frac{3}{2}\log^2\left(\frac{-Q^2}{m_t^2}\right) - \frac{33-2N_F}{6}\log\left(\frac{\mu^2}{m_t^2}\right)\right\}F_{LO}\end{aligned} \tag{2.92}$$

For the renormalization of α_s, the modified minimal-subtraction scheme $\overline{MS}$ with the top-quark decoupled from the running of α_s is used

$$\frac{\delta\alpha_s}{\alpha_s} = \frac{\alpha_s}{\pi}\Gamma(1+\epsilon)\left(\frac{4\pi\mu^2}{\mu_R^2}\right)^\epsilon\left\{-\frac{33-2(N_F+1)}{12\epsilon} + \frac{1}{6}\log\frac{\mu_R^2}{m_t^2}\right\}, \tag{2.93}$$

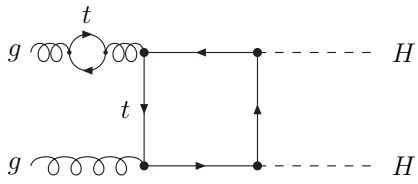

Figure 2.8: Feynman diagram for $gg \to HH$ exemplifying external self-energy corrections.

where $N_F = 5$ [3, 4, 194]. The additional divergence and finite term due to the top quark is cancelled by the external self-energies Δ_t for the amputated Green-functions (Figure 2.8),

$$\delta_{\alpha_s} F = \left(\frac{\delta \alpha_s}{\alpha_s} + \Delta_t \right) F_{LO} \tag{2.94}$$

with

$$\Delta_t F = \frac{\alpha_s}{\pi} \Gamma(1+\epsilon) \left(\frac{4\pi\mu^2}{m_t^2} \right)^{\epsilon} \frac{-1}{6\epsilon} F_{LO} \tag{2.95}$$

resulting in the explicit sum over the 5 light flavours

$$\delta_{\alpha_s} F = \frac{\alpha_s}{\pi} \Gamma(1+\epsilon)(4\pi)^{\epsilon} \left[-\frac{33 - 2N_F}{12\epsilon} \right] F_{LO}. \tag{2.96}$$

The amputation of the external legs gives an additional factor 1/2. Since the top-loop can appear in both legs there is a factor 2 which cancels the factor 1/2 from the amputation.
This leads to an additional logarithmic term in Equation (2.93) and avoids the appearance of large artificial logarithms in the total result.

Rewriting this expression to the overall coefficients used in our calculation we end up with the following counter term due to α_s and the external self energies involving the top quark

$$\delta_{\alpha_s} F = \frac{\Gamma(1+\epsilon)\Gamma(1-\epsilon)}{\Gamma(1-2\epsilon)} \left(\frac{4\pi\mu^2}{m_t^2} \right)^{2\epsilon} \left[-\frac{33 - 2N_F}{6} \right] \left[\frac{1}{\epsilon} - \log \frac{\mu^2}{m_t^2} \right] F_{LO} \tag{2.97}$$

Since there are explicit cancellations between the α_s and HTL counter term we add them up to a subtraction term denoted as $\delta_{IR} F$

$$\delta_{IR} F = \frac{\Gamma(1+\epsilon)\Gamma(1-\epsilon)}{\Gamma(1-2\epsilon)} \left(\frac{4\pi\mu^2}{m_t^2} \right)^{2\epsilon} F_{LO} \left\{ \frac{3}{\epsilon^2} - \frac{3}{\epsilon} \log(-\rho_s) + \frac{3}{2} \log^2(-\rho_s) - \frac{11}{2} + \frac{\pi^2}{2} \right\} \tag{2.98}$$

with $\rho_s = Q^2/m_t^2$. Adding this expression to the 2-loop contributions results in the pure top-mass dependent part of the virtual corrections. This however, still involves the bare top mass that has to be renormalized, too.

In the on-shell scheme the counter term δm_t reads

$$\frac{\delta m_t}{m_t} = -\frac{\alpha_s}{\pi}\Gamma(1+\epsilon)\left(\frac{4\pi\mu^2}{m_t^2}\right)^{\epsilon}\left(\frac{1}{\epsilon}+\frac{4}{3}\right). \tag{2.99}$$

The mass counter term of Equation (2.88) can be translated to the form factors according to Equation (2.89),

$$\begin{aligned}\delta_{m_t}F &= -2\frac{\delta m_t}{m_t}m_t^2\frac{\partial\tilde{F}_{LO}}{\partial m_t^2} \\ &= \Gamma(1+\epsilon)\frac{\Gamma(1-\epsilon)}{\Gamma(1-2\epsilon)}\left(\frac{4\pi\mu^2}{m_t^2}\right)^{\epsilon}\left(\frac{1}{\epsilon}+\frac{4}{3}\right)\left\{\epsilon F_{LO} + m_t^2\frac{\partial F_{LO}}{\partial m_t^2}\right\}.\end{aligned} \tag{2.100}$$

2.2.5 Finite Part of the Virtual Corrections

The virtual part of the differential partonic cross section can be expressed in terms of the form factors after summing up all the box diagrams, the one-particle reducible diagrams, the triangular diagrams, all their permutations and the counter terms as

$$\frac{\mathrm{d}\hat{\sigma}_{virt}}{\mathrm{d}t} = KRe\Big\{\left[\mathcal{F}_{1\triangle}^{LO}C_{\triangle}+\mathcal{F}_{1\square}^{LO}\right]^*\left[C_{\triangle}\mathcal{F}_{1\triangle}+\mathcal{F}_{1\square}\right]+\mathcal{F}_{2\square}^{LO^*}\mathcal{F}_{2\square}\Big\} \tag{2.101}$$

with $\mathcal{F}_{i,\square}$ the two form factors of the box contributions and $\mathcal{F}_{1,\triangle}$ the form factor of the triangular contributions, the overall coefficient

$$K = \frac{G_F^2\alpha_s^3 m_t^4}{256(2\pi)^4Q^4}, \tag{2.102}$$

and

$$C_{\triangle} = \frac{3m_h^2}{Q^2-m_h^2}. \tag{2.103}$$

The form factors are normalized such that in the heavy-top limit the LO form factors approach the values

$$\begin{aligned}\mathcal{F}_{1\triangle}^{LO} &= \frac{2}{3}, \\ \mathcal{F}_{1\square}^{LO} &= -\frac{2}{3}, \\ \mathcal{F}_{2\triangle}^{LO} &= \frac{2}{3}, \\ \mathcal{F}_{2\square}^{LO} &= \mathcal{O}\left(\frac{Q^2}{m_t^2}\right),\end{aligned} \tag{2.104}$$

and for the NLO form factors as of [181]

$$\mathcal{F}_{i,\triangle/\square} = \frac{\Gamma(1-\epsilon)}{\Gamma(1-2\epsilon)} \left(\frac{4\pi\mu^2}{m_t^2}\right)^{\epsilon} \left\{\frac{3}{\epsilon^2} - \frac{3}{\epsilon}\log(-\rho_s) + \frac{3}{2}\log^2(-\rho_s) - \frac{11}{2} + \frac{\pi^2}{2}\right\} \mathcal{F}^{LO}_{i,\triangle/\square} \,. \tag{2.105}$$

The expression in Equation (2.101) considering all the box, the triangular, the one-particle reducible diagrams and the counter terms is finite. An integration of this expression over the Mandelstam variable t_1 leads to the virtual part of the cross section depending only on Q^2. The detailed implementation of this additional integration is explained in Section 2.2.6. The virtual part of the differential hadronic cross section can thus be obtained by multiplying this virtual partonic cross section with the differential gluon density $\mathcal{L}^{gg}$ as

$$Q^2 \frac{\mathrm{d}\Delta\sigma_{virt}}{\mathrm{d}Q^2} = Q^2 \int_{\tau_0}^{1} \mathrm{d}\tau \frac{\mathrm{d}\mathcal{L}^{gg}}{\mathrm{d}\tau} \hat{\sigma}_{virt}(Q^2)\delta(Q^2 - \tau S) = \tau \frac{\mathrm{d}\mathcal{L}^{gg}}{\mathrm{d}\tau} \hat{\sigma}_{virt}(Q^2)\Big|_{\tau=\frac{Q^2}{S}} \,. \tag{2.106}$$

Hence, the virtual part of the differential cross section is a seven dimensional integral which needs to be evaluated numerically.

2.2.6 Numerical Evaluation

Besides the derivation of the individual amplitudes a major challenge of this project is the numerical evaluation of the integrals. Up to seven dimensional integrals have to be calculated where six dimensions originate from the Feynman parametrization and one from the phase-space integration. The numerical evaluation of those integrals has been performed using the adaptive Monte Carlo routine VEGAS [195]. In addition to the numerical instabilities above the threshold described at the end of Section 2.1, numerical instabilities occur due to the phase-space integration and for small imaginary parts $\bar{\epsilon}$ of the quark mass. In the following, the methods how the integrals have been stabilized are described.

The additional integration over the phase-space variable t_1 to the six dimensional Feynman integral leads to logarithmic divergences for each individual diagram at the end points. Therefore we substitute t_1 by y smoothing the function in the integration range for each individual diagram:

$$\int_{t_{1-}}^{t_{1+}} \frac{\mathrm{d}t_1}{t_1 u_1 - s M_H^2} f(t_1, u_1) = \int_{y_-}^{y_+} \frac{\mathrm{d}y}{t_{1+} - t_{1-}} \left[f(t_1, u_1) + f(u_1, t_1)\right] \tag{2.107}$$

with $u_1 = -s - t_1$, the substitution $y = \log\frac{t_1 - t_{1-}}{m_t^2}$, $f(t_1, u_1)$ the matrix element with the singular coefficient extracted and the integration limits

$$\begin{aligned} t_{1\pm} &= -\frac{s}{2}\left[1 \mp \sqrt{1 - 4\frac{m_h^2}{s}}\right], \\ y_+ &= \log\frac{(t_{1+} - t_{1-})(1-\epsilon)}{m_t^2}, \\ y_- &= \log\frac{(t_{1+} - t_{1-})\epsilon}{m_t^2}, \end{aligned} \tag{2.108}$$

where ϵ is a cut-off regulator at the boundaries of the t_1-integration. We have checked that the total sum of all the diagrams is independent of ϵ.

Further, the numerical integration to obtain the virtual part of the partonic cross section becomes unstable for very small imaginary parts $\bar{\epsilon}$ of the quark mass. Therefore the virtual contributions are calculated with different values of $\bar{\epsilon}$ for which the integration is sufficiently stable. Then an extrapolation is used to obtain the result valid in the narrow width approximation where $\bar{\epsilon} \to 0$. For this calculation we have used the Richardson extrapolation [196]. This is a sequence acceleration method to obtain a better convergence behaviour and is only valid for a polynomial behaviour in the regulator. The number of nodes is inversely proportional to the error. In the simplest case, it combines two approximations obtained by evaluating the polynomial for two different discretizations. For instance, in the case of the approximation of an arbitrary function f with two nodes at the locations h and $2h$ the approximation polynomial M_2 can generically be expressed as:

$$M_2(h) = af(h) + bf(2h).$$

This is required to be the same as the value at the origin up to order h^2,

$$M_2(h) = af(h) + bf(2h) \stackrel{!}{=} f(0) + \mathcal{O}(h^2).$$

Solving this expression for M_2 leads to

$$M_2(h) = 2f(h) - f(2h).$$

The approximations M_i can be derived with the same idea up to any order. Figure 2.9 sketches the Richardson extrapolation of a function $f(x)$ with four nodes. Alternatively, the approximation polynomial can iteratively be expressed as

$$M_{i+1}(h) = \frac{t^{k_i} M_i\left(\frac{h}{t}\right) - M_i(h)}{t^{k_i} - 1}, \tag{2.109}$$

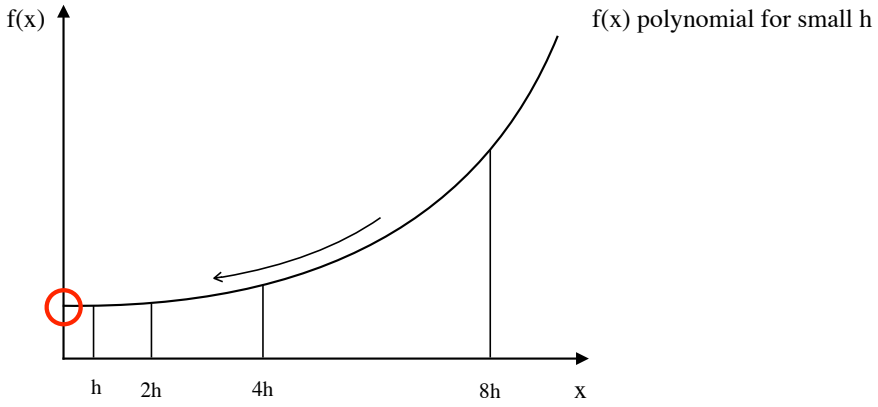

Figure 2.9: Sketch of the Richardson extrapolation for a polynomial $f(x)$.

where h and h/t are two step sizes and k_i the truncation error, i.e. the error is of the order of $\mathcal{O}\left(h^{k_i}\right)$.

For our calculation, h is identified with the imaginary part of the quark mass, $\bar{\epsilon}$. Several numbers of nodes have been tested to see when the plateau is reached where additional nodes do not improve the approximation significantly.

For this purpose, the differential cross sections have been calculated for four different $\bar{\epsilon}$ values for every individual box diagram. Then the Richardson extrapolation has been applied using different numbers of nodes. The explicit Richardson polynomials used for this, read

$$\begin{aligned} M_2\left[f(h), f(2h)\right] &= 2f(h) - f(2h) = f(0) + \mathcal{O}(h^2), \\ M_4\left[f(h), f(2h), f(4h)\right] &= [8f(h) - 6f(2h) + f(4h)]/3 = f(0) + \mathcal{O}(h^3), \\ M_8\left[f(h), f(2h), f(4h), f(8h)\right] &= [64f(h) - 56f(2h) + 14f(4h) - f(8h)]/21 \\ &= f(0) + \mathcal{O}(h^4)\,. \end{aligned} \tag{2.110}$$

Figure 2.10 shows the results for one specific diagram (form factor 1 of box diagram 45 in Appendix A). In the upper histogram one can see the invariant Higgs pair mass distribution for different $\bar{\epsilon}$ values, i.e. different sizes of the imaginary part of the top mass. In addition, there are the values in the narrow width approximation obtained with the Richardson extrapolation for various numbers of nodes referred to as $RiEx$. The first index defines how many nodes have been used. Since the numerical error is quite sizable for an $\bar{\epsilon}$ value of 0.1, the Richardson extrapolation has been calculated once including 0.1 and once starting at 0.2. The index 0.1 at the $RiEx$ means that $\bar{\epsilon} = 0.1$ is included in the Richardson extrapolation while the index 0.2 means that the $\bar{\epsilon}$ values start at 0.2. The error bands represent the numerical error for the curves with the different $\bar{\epsilon}$ while the errors of the $RiEx$ curves have been obtained by adding

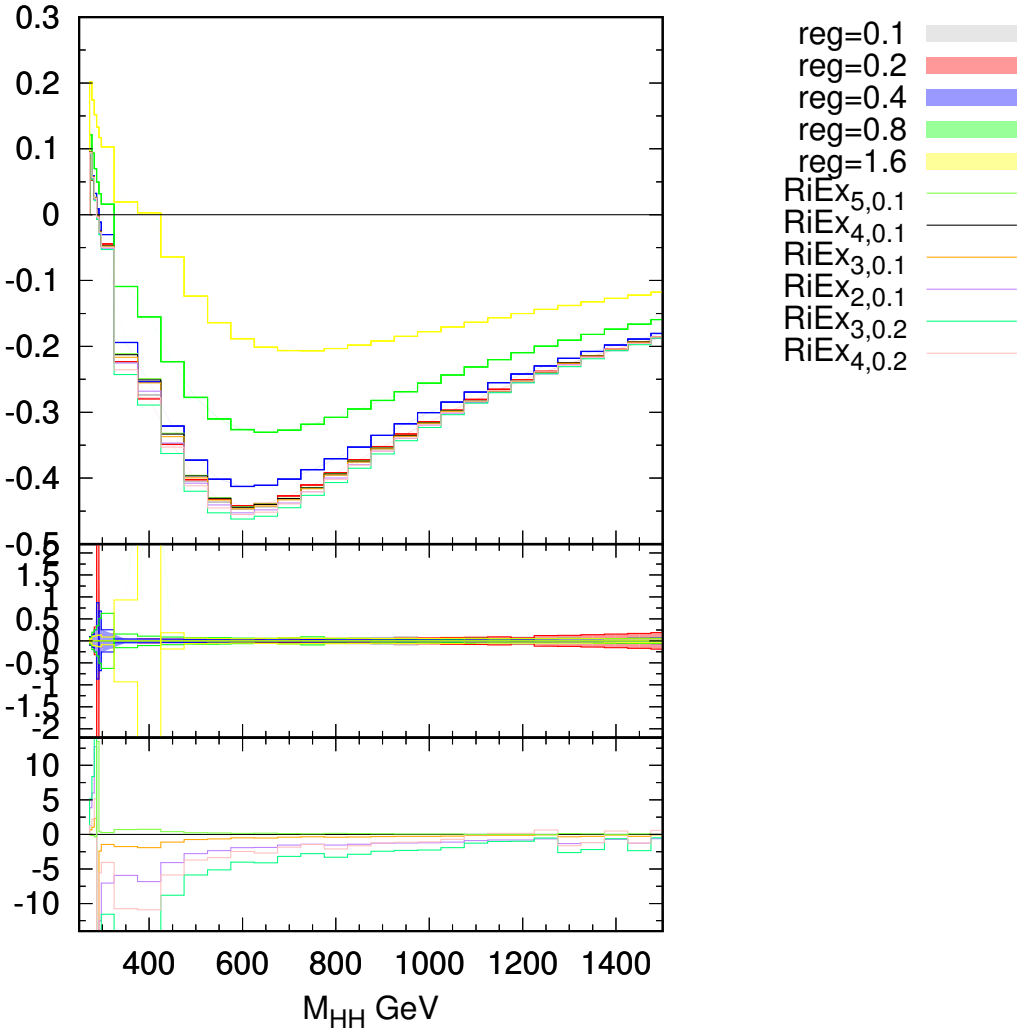

Figure 2.10: The upper histogram illustrates the contribution of one individual box diagram (box diagram 45 in Appendix A) to the differential cross section over the invariant Higgs pair mass. The curves labeled by "$reg = x$" show the contributions for $\bar{\epsilon} = x$. The curves labeled by "$RiEx_{y,z}$" illustrate the narrow width approximation obtained by a Richardson extrapolation with y the number of nodes and starting with the node at $z = 0.1, 0.2$. The middle plot shows the numerical integration error in percentages and the lower plot shows the deviations of the different extrapolated results from the default $RiEx_{4,0.1}$ result in percentages.

$\bar{\epsilon}$	differential cross section
$\bar{\epsilon} = 0.1$	$-0.4472 \pm 1.6 \cdot 10^{-4}$
$\bar{\epsilon} = 0.2$	$-0.4419 \pm 1.4 \cdot 10^{-4}$
$\bar{\epsilon} = 0.4$	$-0.4126 \pm 1.1 \cdot 10^{-4}$
$\bar{\epsilon} = 0.8$	$-0.3263 \pm 2.1 \cdot 10^{-4}$
$\bar{\epsilon} = 1.6$	$-0.1884 \pm 9.6 \cdot 10^{-5}$

Table 2.1: Virtual mass effects of the partonic differential cross section values for different $\bar{\epsilon}$ at an invariant Higgs pair mass of 600 GeV without the factor K of Equation (2.102) for the first form factor of box 45.

$RiEx_{x,y}$	differential cross section	numerical error
$RiEx_{4,0.1}$	-0.44418	0.00061
$RiEx_{3,0.1}$	-0.44641	0.00050
$RiEx_{2,0.1}$	-0.45262	0.00034
$RiEx_{3,0.2}$	-0.46206	0.00045
$RiEx_{4,0.2}$	-0.55386	0.00055

Table 2.2: Virtual mass effects of the partonic differential cross section obtained with the Richardson extrapolation using different numbers of nodes at an invariant Higgs pair mass of 600 GeV without the factor K of Equation (2.102) for the first form factor of box 45.

quadratically the error for every single node involved in the Richardson extrapolation. In the middle plot the statistical errors of the numerical integration in percentages are illustrated. These amount to less than 0.2% for almost the whole range in the invariant Higgs pair mass for this particular box diagram. In the lower plot the deviations from the default result $RiEx_{4,0.1}$ are given in percentages.

In the upper plot one can observe the good convergence behaviour as the lines approach each other for smaller $\bar{\epsilon}$ values reaching a plateau. The same behaviour can be observed for different numbers of nodes for the Richardson extrapolation; the differences between the curves decrease for more nodes. This underlines the stability and reliability of the method. Since it is difficult to distinguish the different curves in the histogram, the specific values for the differential partonic cross section at an invariant Higgs pair mass of 600 GeV are listed in Table 2.1 and in Table 2.2 the corresponding values obtained by the Richardson extrapolation. We found that four different $\bar{\epsilon}$ values are sufficient: 0.1, 0.2, 0.4, 0.8. The addition of a further node at 1.6 does not yield a significant improvement.

2.3 Real Corrections

The real corrections consist of one-loop diagrams with an additional massless particle in the final state. At LO Higgs pair production is mediated by two gluons in the initial state. At NLO, however, additional channels with gq and $q\bar{q}$ in the initial state contribute. As in the calculation for the virtual corrections we subtract the matrix elements in the heavy-top limit to obtain an IR safe expression. Therefore, we perform in a first step the calculation in the heavy-top limit. In a second step, these results are used for the full massive calculation.

2.3.1 The Heavy-Top Limit

For the LO cross section in the heavy-top limit two different diagrams have to be calculated (Figure 2.11). The expression for the matrix element can be derived from the effective Feynman rules of Figure 2.12. The squared matrix element averaged over all possible spin and colour configurations reads

$$\sum \overline{|\mathcal{M}_{LO}|^2} = \Gamma(1+\epsilon)^2 \kappa \left(\frac{4\pi\mu^2}{m_t^2}\right)^{2\epsilon} \left(\frac{\alpha_s}{3\pi v^2}\right)^2 \frac{Q^4}{64} \left(\frac{1}{1-\epsilon}\right) \tag{2.111}$$

with $\kappa = \left(\frac{3m_h^2}{Q^2-m_h^2} - 1\right)^2$. The NLO matrix elements can be derived with the same procedure using the effective Feynman rules of Figure 2.12. Let the momenta of the two initial state particles be denoted by q_i $(i = 1, 2)$ and the momenta of the three final state particles by p_i with p_1 being the massless parton. The initial state particles are massless, $q_i^2 = 0$, while for the final state particles $p_1^2 = 0$ and $p_2^2 = p_3^2 = m_h^2$ holds. The Mandelstam variables used for the matrix elements are defined as

$$\begin{aligned} s &= 2q_1q_2 \\ t &= -2q_1p_1 \\ u &= -2q_2p_1 \end{aligned} \tag{2.112}$$

and the following sum rule is valid

$$Q^2 = m_{HH}^2 = (q_1 + q_2 - p_1)^2 = s + t + u. \tag{2.113}$$

Using these definitions, the spin and colour averaged matrix elements can be ex-

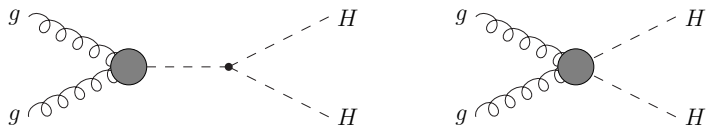

Figure 2.11: LO Feynman diagrams in the heavy-top limit.

pressed as

$$\begin{aligned}
\sum \overline{|\mathcal{M}_{gg}|^2} &= \kappa \frac{\Gamma^2(1+\epsilon)}{(1-\epsilon)^2} \left(\frac{4\pi\mu^2}{m_t^2}\right)^{2\epsilon} \frac{G_F^2 \alpha_s^3}{12\pi} \left[(1-\epsilon)\frac{s^4+t^4+u^4+Q^8}{stu} - 4\epsilon Q^2\right], \\
\sum \overline{|\mathcal{M}_{gq}|^2} &= \kappa \frac{\Gamma^2(1+\epsilon)}{(1-\epsilon)} \left(\frac{4\pi\mu^2}{m_t^2}\right)^{2\epsilon} \frac{G_F^2 \alpha_s^3}{27\pi} \left[\frac{s^2+u^2}{-t} + \epsilon\frac{(s+u)^2}{t}\right], \\
\sum \overline{|\mathcal{M}_{q\bar{q}}|^2} &= \kappa \Gamma^2(1+\epsilon) \left(\frac{4\pi\mu^2}{m_t^2}\right)^{2\epsilon} \frac{8 G_F^2 \alpha_s^3}{81\pi} \left[\frac{t^2+u^2}{s} - \epsilon\frac{(t+u)^2}{s}\right].
\end{aligned} \tag{2.114}$$

The partonic cross section can then be obtained by integrating the spin and colour averaged matrix element over the three particle phase space $\mathrm{d}\Phi_3$. In D dimensions $\mathrm{d}\Phi_3$ with three different masses can be expressed in general as

$$\mathrm{d}\Phi_3 = \mu^{4-D} \frac{d^{D-1}p_1}{(2\pi)^{D-1} 2p_1} \frac{d^{D-1}p_2}{(2\pi)^{D-1} 2p_2} \frac{d^{D-1}p_3}{(2\pi)^{D-1} 2p_3} (2\pi)^D \delta_D(p_1+p_2+p_3-q_1-q_2). \tag{2.115}$$

For this calculation $\mathrm{d}\Phi_3$ has been parameterized such that the two particle phase space factorizes. We introduce x_i as the fraction of the partonic center of mass energy $\sqrt{s}$ carried by the final state particle i: $p_i^0 = x_i \frac{\sqrt{s}}{2}$ and $\mu_i = m_i/\sqrt{s}$. For the x_i the sum rule $\sum x_i = 2$ holds. In a first step, D-dimensional spherical coordinates are introduced. We decompose the four-momenta into the common four space-time coordinates and the remaining D-4 dimensional perpendicular components $\vec{0}_\perp$ which are set to zero. The angle ϑ has been chosen as the angle between the first incoming particle and the radiated gluon while χ has been chosen as the projected angle between the first incoming particle and the second final state particle (Figure 2.13). The angle between the first outgoing and the second incoming particle has been denoted as ϑ_{12}. This leads to the following parametrization of the incoming q_i and outgoing p_i

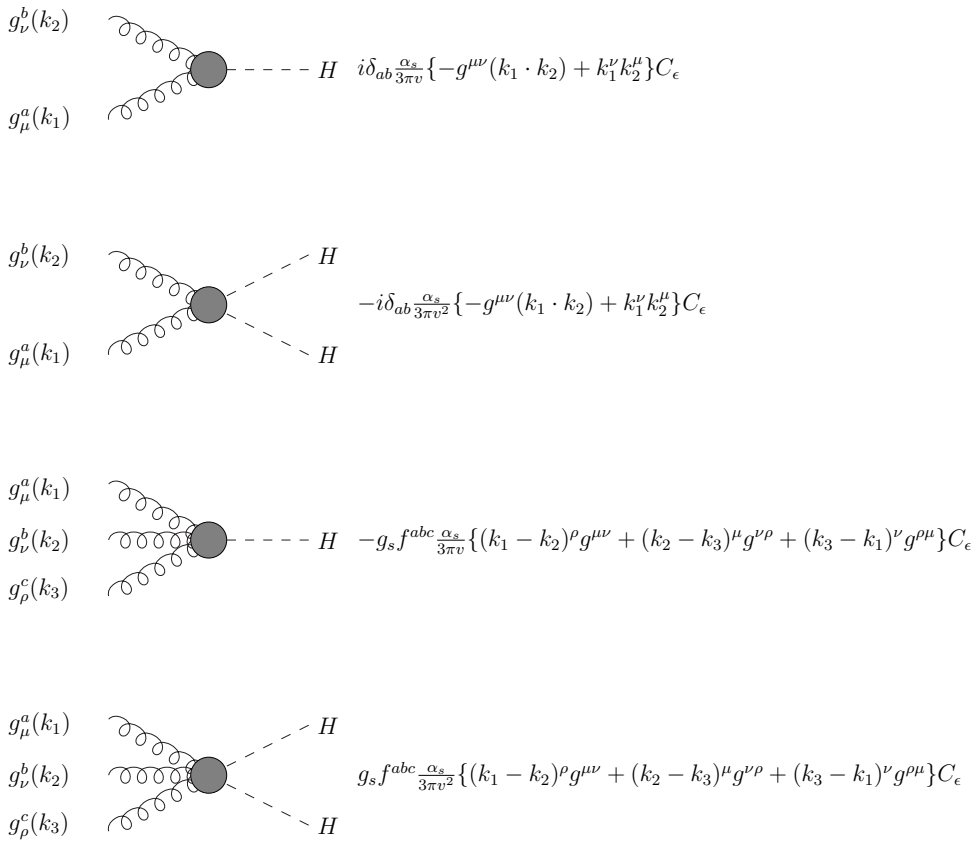

Figure 2.12: Effective Feynman rules used for the calculation of the real matrix elements in the heavy-top limit. The factor C_ϵ is defined as $C_\epsilon = \Gamma(1+\epsilon)\left(\frac{4\pi\mu^2}{m_t^2}\right)^\epsilon$.

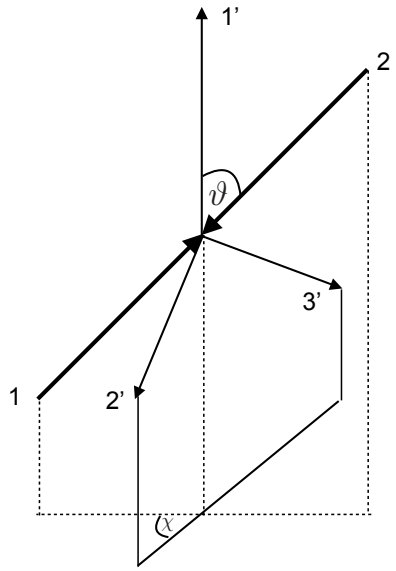

Figure 2.13: Illustration of the spherical coordinates with particle 1 and 2 the two incoming particles and 1',2' and 3' the outgoing particles.

momenta

$$\begin{aligned}
q_1 &= \frac{\sqrt{s}}{2}\left(1;\sin\vartheta,0,\vec{0}_\perp,\cos\vartheta\right),\\
q_2 &= \frac{\sqrt{s}}{2}\left(1;-\sin\vartheta,0,\vec{0}_\perp,-\cos\vartheta\right),\\
p_1 &= x_1\frac{\sqrt{s}}{2}\left(1;0,0,\vec{0}_\perp,\beta_1\right),\\
p_2 &= x_2\frac{\sqrt{s}}{2}\left(1;\beta_2\sin\vartheta_{12}\cos\chi,\beta_2\sin\vartheta_{12}\sin\chi,\vec{0}_\perp,\beta_2\cos\vartheta_{12}\right),\\
p_3 &= \frac{\sqrt{s}}{2}\left(x_3;-\vec{p}_1-\vec{p}_2\right),
\end{aligned} \tag{2.116}$$

with $\beta_i = \sqrt{1-4\frac{\mu_i^2}{x_i^2}}$. This results in the following expression for the three particle phase space

$$\mathrm{d}\Phi_3 = \frac{s}{256\pi^4}\left(\frac{4\pi\mu^2}{x_1x_2s}\right)^{2\epsilon}\frac{(1-\cos^2\vartheta)^{-\epsilon}\sin^{-2\epsilon}\chi\left(\beta_1^2\beta_2^2\frac{1-\cos^2\vartheta_{12}}{4}\right)^{-\epsilon}}{\Gamma(1-2\epsilon)}\mathrm{d}x_1\mathrm{d}x_2\mathrm{d}\cos\vartheta\mathrm{d}\chi \tag{2.117}$$

with the integration limits

$$\begin{aligned}
0 \le \vartheta,\chi \le \pi,\\
2\mu_1 \le x_1 \le 1+\mu_1^2-(\mu_2+\mu_3)^2,\\
x_2^- \le x_2 \le x_2^+,
\end{aligned} \tag{2.118}$$

using the abbreviations

$$\begin{aligned} x_2^{\pm} &= \frac{1}{2a}[b \pm \sqrt{\Delta}], \\ a &= 1 - x_1 + \mu_1^2, \\ b &= (2 - x_1)(a + \mu_2^2 - \mu_3^2), \\ \Delta &= (x_1^2 - 4\mu_1^2)[a - (\mu_2 + \mu_3)^2][a - (\mu_2 - \mu_3)^2]. \end{aligned} \tag{2.119}$$

Next, we substitute the variable x_2 by $x_2 = 1 - (1 - Q^2/s)x$.

Returning to the investigated process, we choose $m_1 = 0$ to be the mass of the radiated massless particle and m_2 and m_3 the masses of the two Higgs particles (m_h). Further the variable z is introduced as $z = Q^2/s$. These definitions simplify the expression of the integration boundaries $x_\pm$ of x to $x_\pm = \frac{1}{2}[1 \pm \beta]$ with $\beta = \sqrt{1 - 4\mu_h^2/z}$. Further we substitute the variable x by r as $x = x_- + (x_+ - x_-)r$. Using these substitutions the following explicit expression for the phase space integration is obtained

$$\mathrm{d}\Phi_3 = \frac{s\beta^{1-2\epsilon} r^{-\epsilon}(1-r)^{-\epsilon}}{256\pi^4\Gamma(1-2\epsilon)} \frac{(1-z)^{1-2\epsilon}}{z^\epsilon} \left(\frac{4\pi\mu^2}{s}\right)^{2\epsilon} (1 - \cos^2\vartheta)^{-\epsilon} \sin^{-2\epsilon}\chi \mathrm{d}r\mathrm{d}z\mathrm{d}\cos\vartheta\mathrm{d}\chi\,. \tag{2.120}$$

The integration limits are given by $0 \leq r \leq 1$, $\tau_0 \leq z \leq 1$ and $0 \leq \vartheta, \chi \leq \pi$. After performing the integration over χ and r and fixing $Q^2 = zs$, the two particle phase space Φ_2 factorizes resulting in the following expression for $\mathrm{d}\Phi_3$

$$\mathrm{d}\Phi_3 = \Phi_2 \frac{Q^2}{32\pi^2} \frac{z^{-1+\epsilon}(1-z)^{1-2\epsilon}}{\Gamma(1-\epsilon)} \left(\frac{4\pi\mu^2}{Q^2}\right)^\epsilon \left(\frac{1-\cos^2(\vartheta)}{4}\right)^{-\epsilon} \mathrm{d}z\,\mathrm{d}\cos\vartheta \tag{2.121}$$

with the integrated two-particle phase space

$$\Phi_2 = \frac{\beta^{1-2\epsilon}}{8\pi} \frac{\Gamma(1-\epsilon)}{\Gamma(2-2\epsilon)} \left(\frac{4\pi\mu^2}{Q^2}\right)^\epsilon, \tag{2.122}$$

and the integration boundaries $0 \leq \vartheta \leq \pi$ and $4\mu_h^2 \leq z \leq 1$. This expression can now be used to integrate the matrix elements in Equation (2.114) over $\mathrm{d}\Phi_3$ to obtain the partonic cross section. The Born term factorizes from the full matrix element. The integration over the angle ϑ can be performed while the integration over z is kept. The partonic real cross sections $\hat{\sigma}_{ij}$ ($ij = gg, gq, q\bar{q}$) can finally be expressed as

$$\hat{\sigma}_{ij} = \sigma_0 \frac{\alpha_s}{\pi} \left[D_{ij}(z)\Theta(1-z) + \delta_{ig}\delta_{jg} C \delta(1-z)\right] \tag{2.123}$$

with

$$C = \frac{\Gamma(1-\epsilon)}{\Gamma(1-2\epsilon)} \left(\frac{4\pi\mu^2}{Q^2}\right)^{\epsilon} \left\{\frac{3}{\epsilon^2} + \frac{33-2N_F}{6\epsilon}\right\},$$
$$D_{gg} = -\frac{11}{2}(1-z)^3 - \frac{z}{\epsilon}\frac{\Gamma(1-\epsilon)}{\Gamma(1-2\epsilon)} \left(\frac{4\pi\mu^2}{s}\right)^{\epsilon} P_{gg}(z) + 6[1+z^4+(1-z)^4] \left[\frac{\log(1-z)}{1-z}\right]_+,$$
$$D_{gq} = \frac{\Gamma(1-\epsilon)}{\Gamma(1-2\epsilon)} \left(\frac{4\pi\mu^2}{s}\right)^{\epsilon} \left\{zP_{gq}(-\frac{1}{2\epsilon} + \log(1-z)) - 1 + 2z - \frac{z^2}{3}\right\},$$
$$D_{q\bar{q}} = \frac{32}{27}(1-z)^3.$$

$P_{ij}(z)$ are the regularized Altarelli-Parisi splitting functions

$$P_{gg}(z) = 6\left\{\left[\frac{1}{1-z}\right]_+ + \frac{1}{z} - 2 + z(1-z)\right\} + \delta(1-z)\frac{33-2N_F}{6},$$
$$P_{gq}(z) = \frac{4}{3}\frac{1+(1-z)^2}{z}. \tag{2.124}$$

The infrared singularities of the real corrections C cancel exactly against the ones of the virtual corrections. The left over collinear initial-state singularities contained in the P_{ij} coefficients, however, are absorbed in the NLO parton densities. Therefore the parton densities need to be renormalized. For this purpose the bare gluon densities $f_{g0}(x_j, \mu_F^2)$ in Equation (2.125) are replaced by the renormalized ones and the related counterterms in Equation (2.126)

$$\mathrm{d}\sigma = \int_{\tau_0}^1 \mathrm{d}x_1 \int_{\tau_0/x_1}^1 \mathrm{d}x_2\, f_{g0}(x_1) f_{g0}(x_2) \mathrm{d}\hat{\sigma}_{LO}(Q^2 = z\tau s), \tag{2.125}$$

$$f_{g0}(x) = F_{gg} \otimes f_g(x, \mu_F^2) + \sum_{q,\bar{q}} F_{gq} \otimes f_q(x, \mu_F^2), \tag{2.126}$$

with

$$F_{ij} = \delta_{ij}\delta(1-x) + \frac{\alpha_s}{2\pi}\left\{\frac{1}{\epsilon}\frac{\Gamma(1-\epsilon)}{\Gamma(1-2\epsilon)} \left(\frac{4\pi\mu^2}{\mu_F^2}\right)^{\epsilon} P_{ij}(x) - g_{ij}(x)\right\},$$

where μ_F denotes the factorization scale of the parton densities. We introduce the variable $\tau = x_1 x_2/z$ that is related to the momentum fractions x_i carried by the two incoming particles at LO and $\tau_0 = 4m_h^2/S$. The convolution of two functions f and g is defined in general as

$$f \otimes g(x) = \int_0^1 \mathrm{d}y\mathrm{d}z\, f(y)g(z)\delta(x-yz) = \int_x^1 \frac{\mathrm{d}z}{z} f\left(\frac{x}{z}\right) g(z). \tag{2.127}$$

The functions $g_{ij}(x)$ are arbitrary leading to an additional degree of freedom in the counter term definition. It introduces a factorization scheme similar to the renormalization scheme of the ultraviolet renormalization. We use the $\overline{MS}$ scheme for which $g_{gg}(x) = g_{gq}(x) = 0$. The renormalized parton densities are then included in the corresponding parton luminosities

$$\begin{aligned}
\frac{\mathrm{d}\mathcal{L}^{gg}}{\mathrm{d}\tau} &= f_g \otimes f_g(\tau, \mu_F^2), \\
\frac{\mathrm{d}\mathcal{L}^{gq}}{\mathrm{d}\tau} &= f_g \otimes f_q(\tau, \mu_F^2) + f_q \otimes f_g(\tau, \mu_F^2), \\
\frac{\mathrm{d}\mathcal{L}^{q\bar{q}}}{\mathrm{d}\tau} &= f_q \otimes f_{\bar{q}}(\tau, \mu_F^2) + f_{\bar{q}} \otimes f_q(\tau, \mu_F^2).
\end{aligned} \tag{2.128}$$

This results in the following final expressions for the real corrections in the heavy-top limit for the individual channels

$$\begin{aligned}
\Delta\sigma_{gg} &= \frac{\alpha_s}{\pi} \int_{\tau_0}^1 \mathrm{d}\tau \frac{\mathrm{d}\mathcal{L}^{gg}}{\mathrm{d}\tau} \int_{\tau_0/\tau}^1 \frac{\mathrm{d}z}{z} \hat{\sigma}_{LO}(Q^2 = z\tau s) C_{gg}(z), \\
\Delta\sigma_{gq} &= \frac{\alpha_s}{\pi} \int_{\tau_0}^1 \mathrm{d}\tau \sum_{q,\bar{q}} \frac{\mathrm{d}\mathcal{L}^{gq}}{\mathrm{d}\tau} \int_{\tau_0/\tau}^1 \frac{\mathrm{d}z}{z} \hat{\sigma}_{LO}(Q^2 = z\tau s) C_{gq}(z), \\
\Delta\sigma_{q\bar{q}} &= \frac{\alpha_s}{\pi} \int_{\tau_0}^1 \mathrm{d}\tau \sum_{q,\bar{q}} \frac{\mathrm{d}\mathcal{L}^{q\bar{q}}}{\mathrm{d}\tau} \int_{\tau_0/\tau}^1 \frac{\mathrm{d}z}{z} \hat{\sigma}_{LO}(Q^2 = z\tau s) C_{q\bar{q}}(z),
\end{aligned} \tag{2.129}$$

with the real correction coefficients $C_{ij}(z)$ in the heavy-top limit

$$\begin{aligned}
C_{gg}(z) &= -\frac{11}{2}(1-z)^3 - zP_{gg}(z)\log\frac{\mu_F^2}{\tau s} + 6[1 + z^4 + (1-z)^4] \left[\frac{\log(1-z)}{1-z}\right]_+, \\
C_{gq}(z) &= -1 + 2z - \frac{z^2}{3} - \frac{z}{2}P_{gq}(z)\log\frac{\mu_F^2}{\tau s(1-z)^2}, \\
C_{q\bar{q}}(z) &= \frac{32}{27}(1-z)^3.
\end{aligned} \tag{2.130}$$

These results are in agreement with [181].

2.3.2 Massive Calculation

Since the massive real corrections have already been calculated before [170], we used publicly available programs to generate the full matrix elements. The diagrams listed in Appendix B have to be considered for the calculation of the full real cross sections. The code for the numerical evaluation has been generated using the Mathematica packages FeynArts-3.9 [197] and FormCalc-9.4 [198]. The former provides the amplitudes while the latter produces the cross section. For the evaluation of the one-loop

integrals we used the COLLIER-1.2 library [199] since the results were not sufficiently stable in the IR and COLL limits using the standard library implemented in `LoopTools` [198]. As in the calculation for the virtual corrections we subtract the matrix elements in the heavy-top limit to obtain an IR safe expression

$$\frac{|\mathcal{M}^R(p_i,k_j)|^2}{|\mathcal{M}_{LO}(\tilde{p}_i,\tilde{k}_j)|^2} - \frac{|\mathcal{M}^R_{HTL}(p_i,k_j)|^2}{|\mathcal{M}_{LO}(\tilde{p}_i,\tilde{k}_j)|^2} = \frac{\Delta^{RM}(p_i,k_j)}{|\mathcal{M}_{LO}(\tilde{p}_i,\tilde{k}_j)|^2}, \tag{2.131}$$

with $\mathcal{M}^R$ being the matrix element of the real corrections generated by FeynArts and FormCalc and Δ^{RM} the remaining part of the real NLO mass effects. This is possible since the IR singularity structure of the matrix element relative to the Born term of the HTL calculation and the full massive calculation is the same.

Figure 2.14 shows an example diagram for the real NLO corrections with the LO subdiagram. Here the incoming particles are denoted by $p_{a,b}$ and the outgoing by $k_{1,2}$. The left-over momentum of p_a after radiating a gluon with momentum p_i is called p_{ai}. This gluon contributing to the LO subprocess is in general off-shell. We have to project the full three particle kinematics onto the LO subkinematics, i.e. introduce a mapping of the involved four-momenta, in order to have a consistently defined LO matrix element factor. After integration of the mapped LO transverse momentum this mapping is reflected by the additional z dependence of the LO partonic cross section factor in Equation (2.129). The mapping can be achieved using the method described in [200]. Thereby the transformed four-momentum $\tilde{p}_{ai}, \tilde{p}_b$ of the on-shell intermediate and external gluons are defined as

$$\begin{aligned} \tilde{p}^\mu_{ai} &= x_{i,ab} p^\mu_a, \\ \tilde{p}^\mu_b &= p^\mu_b, \end{aligned} \tag{2.132}$$

with $x_{i,ab} = (p_a p_b - p_i p_a - p_i p_b)/(p_a p_b)$ and the final state-momenta $\tilde{k}_j$ are related to the original momenta as

$$\tilde{k}^\mu_j = k^\mu_j - \frac{2k_j\cdot(K+\widetilde{K})}{(K+\widetilde{K})^2}(K+\widetilde{K})^\mu + \frac{2k_j\cdot K}{K^2}\widetilde{K}^\mu, \tag{2.133}$$

where $K^\mu = p^\mu_a + p^\mu_b - p^\mu_i$ and $\widetilde{K}^\mu = \tilde{p}^\mu_{ai} + \tilde{p}^\mu_b$. After the integration over the phase space the real cross sections in the HTL $d\sigma_{HTL}$ of Equation (2.129) is added back to obtain the full real corrections $d\sigma^R$ free of IR and COLL singularities

$$d\sigma^R = \int \mathrm{d}\Phi_3\, \Delta^{\mathrm{RM}} + \mathrm{d}\sigma^{\mathrm{R}}_{\mathrm{HTL}}. \tag{2.134}$$

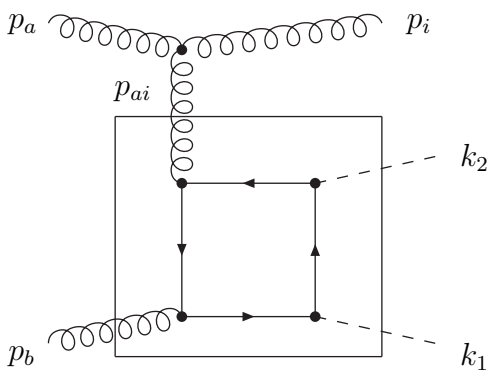

Figure 2.14: Illustration of the LO subprocess contained in the real correction-diagrams. The momentum $p_{ai} = p_a - p_i$ is off-shell ($p_{ai}^2 \neq 0$) in general.

The phase space integration has been performed, as for the virtual corrections, with the VEGAS Monte Carlo integration. A technical cut-off of the order 10^{-8} for the angular integration in the three particle phase space has been applied due to numerical instabilities in the IR and COLL limits. A numerical accuracy of the integration below one pro-mile has been reached.

Chapter 3

Results and Discussion

For the presented results in this chapter the Higgs mass has been chosen to be 125 GeV, the top mass as 172.5 GeV and the center of mass energy as 14 TeV. The renormalization and the factorization scales have been fixed at half the invariant Higgs pair mass. For the PDFs we used the PDF4LHC15 [126] and MMHT2014 [201] sets. The first uses for the strong coupling constant at the scale of the Z mass the value $\alpha_s(M_Z) = 0.118$ at NLO. MMHT2014 uses for the LO α_s at the Z mass a value of $\alpha_s(M_Z) = 0.135$ and at NLO $\alpha_s(M_Z) = 0.1201$. In the first Section 3.1 the differential cross section is presented with a detailed investigation of the K-factor behaviour and the validity of the HTL approximation. The second Section 3.2 discusses the calculation of the total hadronic cross section.

3.1 Differential Cross Section

Figure 3.1 shows the differential cross section as a function of the invariant Higgs boson pair mass m_{hh} obtained by adding the differential cross section in the heavy-top limit produced with HPAIR, the virtual part of the differential cross section obtained by evaluating the seven-dimensional integrals of Equation (2.106) and the real part of the differential cross section calculated with Equation (2.134). This result of the fully massive differential cross section (red curve) is complemented with the HTL results in blue, the HTL plus the full real corrections in yellow, the HTL plus the full virtual corrections in green. Further the LO cross section is included in black for comparison in the left plot. The error bands represent an estimate of the numerical error due to the integration and extrapolation of the virtual mass effects. For the HTL and the HTL plus the real corrections those are too small to be visible in the plot. The left histogram shows the differential cross section produced with the MMHT2014 PDFs, while the PDF4LHC15 have been used for the right histogram.

The lower plots indicate that the NLO mass effects contribute up to 30% on top of the LO mass dependence. Further, it is visible that the main contributions to the total cross section originate from the mass range between about 300 and 800 GeV. In the left figure, the lower subplot illustrates the differential K-factor. This is defined as the ratio of the NLO cross section and the consistent Born term. The blue curve shows that the K-factor of the differential cross section in the HTL is almost independent of the invariant Higgs pair mass. A similar behaviour can be observed for the HTL plus the full real corrections in yellow. The HTL plus the full virtual corrections, however, develops a stronger dependence on the invariant Higgs pair mass. In particular, the K-factor becomes smaller for larger invariant double Higgs pair masses. For instance, at $m_{hh} = 400$ GeV the K-factor is about 1.6, while at $m_{hh} = 1000$ GeV the K-factor decreases to about 1.3 for the green curve. This implies that for higher invariant Higgs pair masses the mass effects become relevant and that the full NLO corrections can no longer be reasonably be approximated by the HTL. Further, it indicates that the virtual NLO mass effects dominate in comparison to the real NLO mass effects and can therefore not be neglected. In the right figure, the lower subplot illustrates the ratios to the HTL results involving the LO mass effects at NLO. Thus the yellow curve shows the NLO mass effects of the real corrections alone and the green curve shows the ones of the virtual corrections alone, both on top of the LO mass effects. As in the left plot, showing the K-factor, it is visible that the blue and the yellow curves develop a flat behaviour, while the green and the red curves decrease for larger invariant Higgs pair masses. This implies again that the HTL is only a reasonable approximation for the invariant Higgs pair mass range up to about 600 GeV, where the NLO mass effects start to exceed the 20% level. The plot for the K-factor could only be produced with MMHT2014 PDFs since PDF4LHC15 does not provide LO PDFs. The right plot of Figure 3.1 has been produced with MMHT2014 as well. Since this looks almost the same as for the PDF4LHC15 PDFs we refrain from showing both of them.

Figure 3.2 shows the dependence of the K-factor on the invariant Higgs pair mass distribution on the left for the contributions involving only the trilinear couplings and on the right for the contributions without the trilinear couplings. The interference and the one-particle reducible terms are not included in these plots. The blue curve shows the heavy-top limit results, while the yellow curve includes in addition the full real contribution and the green curve the full virtual corrections. The red curve shows the fully massive results, i.e. the heavy-top limit plus the mass effects of the real and

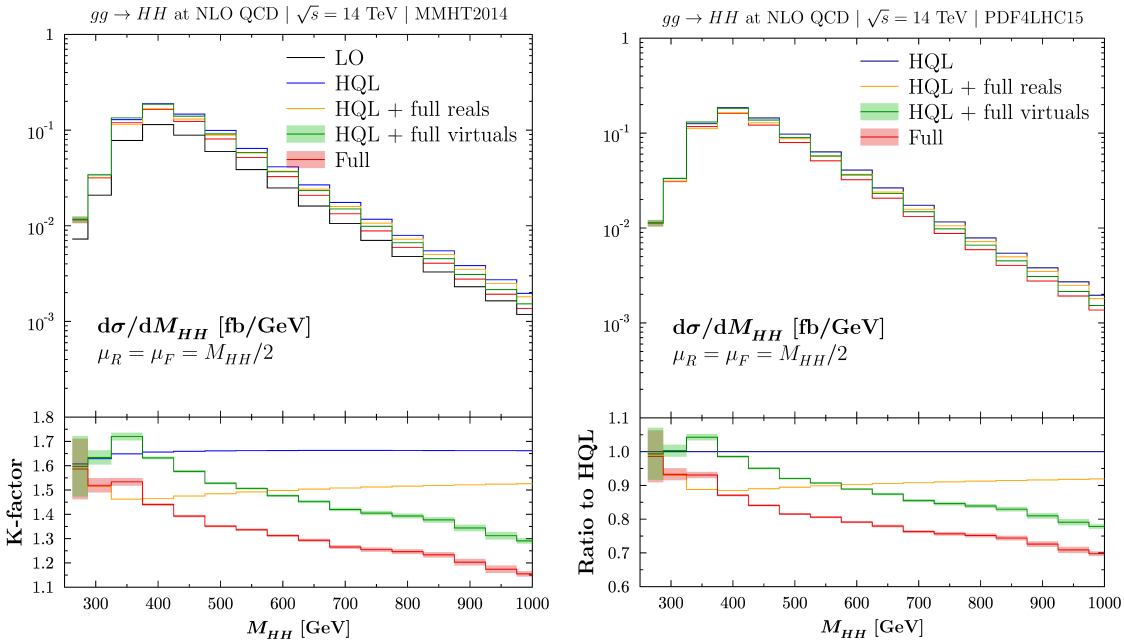

Figure 3.1: Invariant Higgs boson pair mass distribution for $\sqrt{s} = 14$ TeV using in the left plot the MMHT2014 and in the right plot the PDF4LHC15 PDFs. The lower plot on the left shows the K-factor as a function of the invariant double Higgs boson mass while the lower plot on the right shows the ratio to the NLO HTL results as a function of the invariant Higgs boson pair mass.

the virtual contributions. For the trilinear and the continuum contributions the K-factor becomes smaller for larger invariant Higgs pair masses as expected from the restoration of perturbative unitarity in the high-energy limit. However, this behaviour is stronger for the continuum contributions. For instance at an invariant Higgs pair mass of 1000 GeV the K-factor of 1.65 in the HTL gets reduced to 1.45 for the trilinear and to 1.20 for the continuum contributions. This implies that the mass effects are dominated by the continuum contributions at high invariant Higgs pair masses as expected. Further, it is evident that the HTL and the HTL plus real corrections show a similar behaviour in both cases. This corroborates again that the virtual mass effects have a bigger impact than the real contributions in the high invariant Higgs pair mass range and can therefore not be neglected. Those conclusions are additionally supported by Figure 3.3, were the ratios of the triangular (left) respectively continuum (right) K-factors to the full K-factors are illustrated. The blue curves show again the HTL, the yellow curve the HTL plus the full real contributions, the green curve the HTL plus the full virtual corrections and the red curve the fully massive results. From the left plot of Figure 3.3 it is evident that for higher invariant Higgs pair masses the yellow and blue curves are flat and close to unity, while the green and the red curves

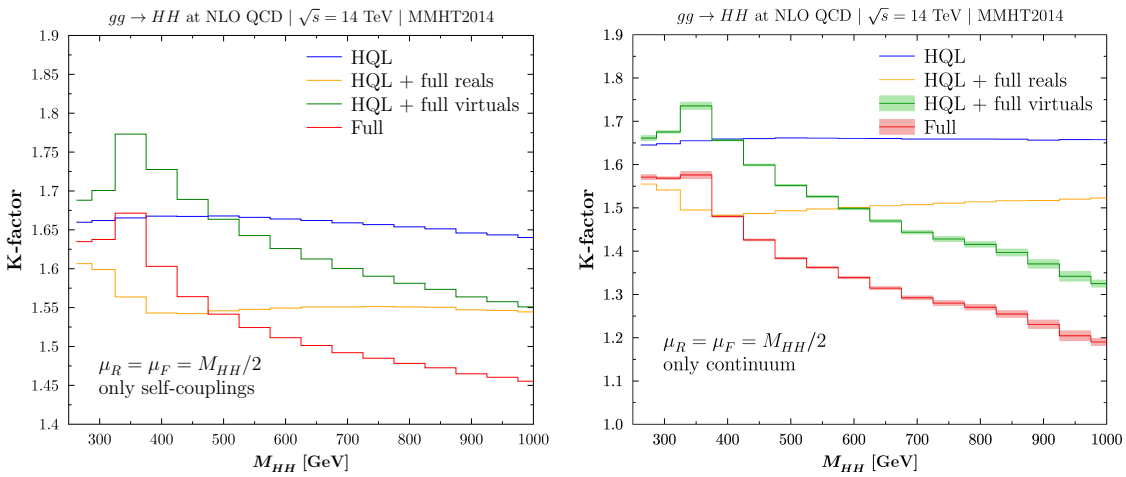

Figure 3.2: The K-factor as a function of the invariant double Higgs boson mass on the left for the trilinear and on the right for the continuum contributions in the mass range from 250 to 1000 GeV. The triangular contributions include only diagrams that involve the trilinear Higgs self-coupling and the continuum contributions only all other one-particle-irreducible diagrams.

gradually increase. This shows once more the dominance of the virtual mass effects for high invariant Higgs pair masses and underlines the relevance of the calculation of the mass effects, in particular the virtual corrections. Further, it is visible that for an invariant Higgs pair mass up to 400-600 GeV the K-factor ratio of the trilinear contributions solely is reasonably close to one. Hence, the NLO mass effects can be approximated within $10 - 20\%$ by the trilinear K-factor alone in this region. For instance at an invariant Higgs pair mass of 400 GeV this would lead to an accuracy of about 10% while at 800 GeV only an accuracy of 20% can be achieved. The distribution of the K-factor ratios in the right plot of Figure 3.3 is almost constant around unity. This confirms that the continuum contributions dominate in the whole invariant Higgs pair mass range and can therefore not be neglected.

3.2 Total Hadronic Cross Section

The total hadronic cross section can be obtained by integrating the differential cross section over the invariant Higgs pair mass. Since this distribution is only known in discrete steps, this integral has to be interpolated. From the differential cross section it is known that the main contributions to the total cross section originate from the invariant Higgs pair mass range between 300 and 800 GeV. Therefore, it is safe to integrate over a range between 275 and 1500 GeV. In the region from 275 to 300 GeV the differential cross section has been derived in steps of 5 GeV and for the range

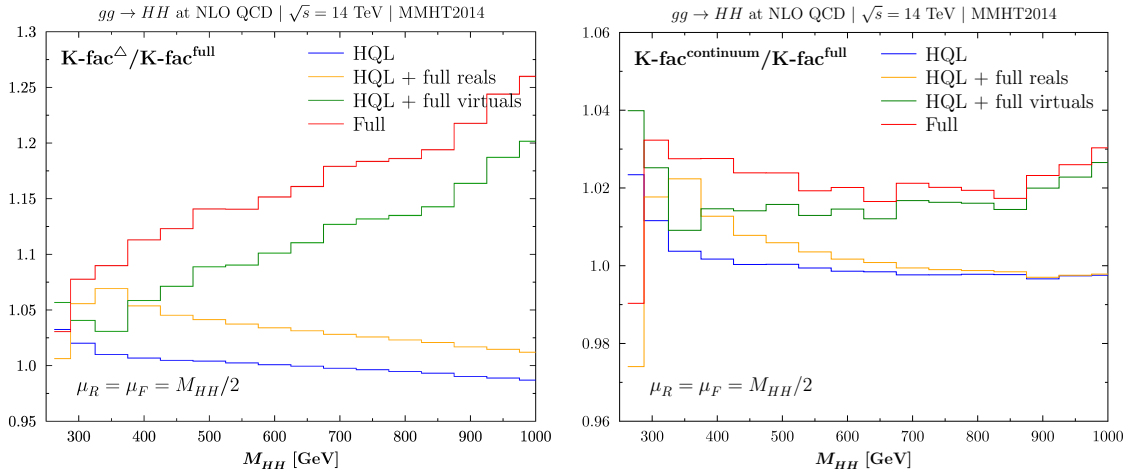

Figure 3.3: The distribution of the ratio of the K-factors on the left for the triangular and on the right for the box contributions to the full K-factor in the mass range from 250 to 1000 GeV. The triangular contributions include only diagrams that involve the trilinear Higgs self-coupling and the box contributions all other one-particle-irreducible diagrams.

between 300 GeV and 1500 GeV in steps of 50 GeV. For the latter, a combination of the trapezoidal rule and the Richardson extrapolation has been used to approximate the integral over the differential cross section. In a first step the differential cross section has been obtained for four different bin sizes: 50, 100, 200, and 400 GeV. For each of them the integral has been approximated using the trapezoidal rule. Thereby the area below a function is estimated as a trapezoid. In general, this method predicts the following approximation for the integral from a to b of a function $f(x)$

$$\int_a^b f(x)\,\mathrm{d}x \approx \frac{\Delta x}{2}[f(x_0) + 2f(x_1) + 2(x_2) + ... + 2f(x_{n-1}) + f(x_n)], \tag{3.1}$$

where n is the number of bins, $\Delta x = (b-a)/n$ and the step size $x_i = a + i\Delta x$. The resulting error can be expressed as

$$-\frac{nh^3}{12} f''(\zeta), \tag{3.2}$$

where ζ is a random point in the integration range [202]. Thus for this calculation, $a = 300$ GeV and $b = 1500$ GeV, while the step size is either 50, 100, 200 or 400 GeV. The values of the four integral values obtained with this method have then been used as the nodes of a Richardson extrapolation to extrapolate the values of the integrals to an infinitesimally small binning. The Richardson extrapolation polynomial has again been calculated using Equation (2.109). The resulting error of the combination of both methods can conservatively be estimated to be of the order of 10^{-4}.

	PDF4LHC15	MMHT2014
σ_{LO}	19.80 fb	23.75 fb
$\sigma_{\mathrm{NLO}}^{\mathrm{HTL}}$	(38.64 ± 0.01) fb	(39.33 ± 0.01) fb
σ_{NLO}	(32.93 ± 0.11) fb	(33.47 ± 0.12) fb

Table 3.1: Comparison of the total hadronic cross section at LO σ_{LO}, in the heavy-top limit $\sigma_{\mathrm{NLO}}^{\mathrm{HTL}}$ and including the full mass dependence σ_{NLO} for the PDF4LHC15 and MMHT2014 PDFs.

For the lower invariant Higgs pair mass region, an extension of Boole's rule has been used to approximate the integral of the differential cross section in the invariant Higgs pair mass range between 275 GeV and 300 GeV. This is a mathematical method to interpolate an integral with equally spaced nodes x_i. It provides the following formula to approximate an integral with six x_i of the function $f(x_i)$ in the integration range from x_0 to x_5 with a step size h [202],

$$\int_{x_0}^{x_5} f(x)\,\mathrm{d}x \approx \frac{5h}{288}[19f(x_0) + 75f(x_1) + 50f(x_2) + 50f(x_3) + 75f(x_4) + 19f(x_5)]. \tag{3.3}$$

The error term can be expressed in general as

$$-\frac{275}{12096}h^7 f(x_6), \tag{3.4}$$

where x_6 is a random number in the integration region. We have chosen six nodes and thus a step size of 5 GeV. A conservative estimation of the error term results in an uncertainty of the order of 10^{-5}. For the invariant Higgs pair mass between 250 GeV and 275 GeV the hadronic cross section amounts to about 0.14 fb.

For the PDF4LHC15 PDFs a total hadronic cross section of $(32.93 \pm 0.11)fb$ has been obtained, while the use of the MMHT2014 PDFs yields a value of $(33.47 \pm 0.12)fb$. The uncertainty reflects the errors due to the numerical integration and the extrapolation. The hadronic NLO cross section in the heavy-top limit using PDF4LHC15 PDFs is $(38.64 \pm 0.01)fb$ and with the MMHT2014 PDFs $(39.33 \pm 0.1)fb$. These are the values produced with HPAIR. These values are supplemented by a negative NLO mass contribution of about -14.8% for PDF4LHC15 and -14.9% for MMHT2014, respectively, compared to the previously known heavy-top limit results involving the full LO mass dependence. Compared to the LO cross section the fully massive NLO QCD corrections result in an increase by about 66%. The difference

between the NLO QCD correction with the fully massive real corrections and the virtual corrections in the HTL amounts to about -4%. The obtained hadronic cross section is in agreement with the results of [184, 185] which obtained a total hadronic cross section of $(32.91^{+13.6\%}_{-12.6\%})fb$ including the fully massive NLO QCD corrections. The given error considers the PDF and scale uncertainties. Table 3.1 gives an overview of all values for the total hadronic cross section obtained in our calculation.

Chapter 4

Conclusions

The aim of this thesis has been the calculation of the NLO QCD corrections to Higgs boson pair production via gluon fusion including the full mass dependence of the top quark in the context of the SM. The main challenge has been the calculation of the virtual corrections since this is a two-loop calculation of a two-to-two process containing massless and massive particles in the loop. The amplitudes have been established with the common Feynman parametrization. Instead of the usual reduction to master integrals, a modification of the standard subtraction method has been developed to achieve a systematic extraction of the ultraviolet, infrared and collinear singularities without reducing them to master integrals. The numerical evaluation of the integration has been performed using the Fortran routine VEGAS. Numerical instabilities, occurring above the virtual thresholds related to the $t\bar{t}$-threshold and virtual intermediate gg-states, have been regularized by introducing an analytic continuation by giving the quark mass a small imaginary part. The integrals have been stabilized by reducing the power of the denominator using integration by parts. To obtain the result in the narrow width approximation we have used a Richardson extrapolation, a sequence acceleration method for which the number of nodes is inversely proportional to the final extrapolation error. The one-particle reducible diagrams have been derived from the known $H \to Z\gamma$ results by properly dressing the effective Feynman rules by form factors. The results of the single Higgs process have been used to derive the triangular diagrams involving the trilinear self-coupling. The strong coupling constant and the top-quark mass have been renormalized to obtain the UV finite virtual corrections. For the strong coupling constant we have used the $\overline{MS}$ scheme with five active flavours and the top-quark mass has been renormalized on-shell. Finally, the results of the heavy-top limit have been subtracted such that the remaining contribution consisted of the IR-finite mass effects. The real cross section has first been recalculated in the HTL. Then the amplitudes of the complete

real corrections have been produced with the publicly available programs FeynArts and FormCalc. As for the virtual corrections, the HTL results have been subtracted from the full amplitudes with the factorized massive Born term. For this purpose, the matrix elements of the NLO results in the HTL have been adjusted to the massive LO part by a transformation of the 4-momenta. The final phase-space integration has led to the real corrections of the differential cross section in the invariant Higgs pair mass.

From this distribution it becomes evident that the main contributions to the cross section originate from the invariant Higgs pair mass range between 300 and 800 GeV. Further, we have observed that the HTL is a reasonable approximation only up to an invariant Higgs pair mass of about 600 GeV since in the high invariant Higgs pair mass range the box diagrams dominate and generate sizable mass effects. This underlines the importance of calculating the virtual and real NLO mass effects. From the differential K-factor one can conclude that for an invariant Higgs pair mass up to 400-600 GeV the NLO QCD corrections can be approximated by the triangular contributions involving the trilinear Higgs couplings only. These corrections can be obtained from single Higgs boson production. Finally, the obtained total hadronic cross section implies a negative contribution of about -15% from NLO mass effects compared to the previous known heavy-top limit results involving the full LO mass dependence. The obtained NLO mass effects are larger than in the case of single Higgs boson production.

Appendix A

Virtual contributions

Complete set of the generic Feynman diagrams for the virtual QCD corrections to Higgs boson pair production. They are divided into box diagrams, one-particle reducible diagrams and triangular diagrams. The box diagrams are further split into six topologies with similar propagator structure. The diagrams with simultaneously interchanged gluon momenta and Higgs momenta have to be added.

Topology 1:

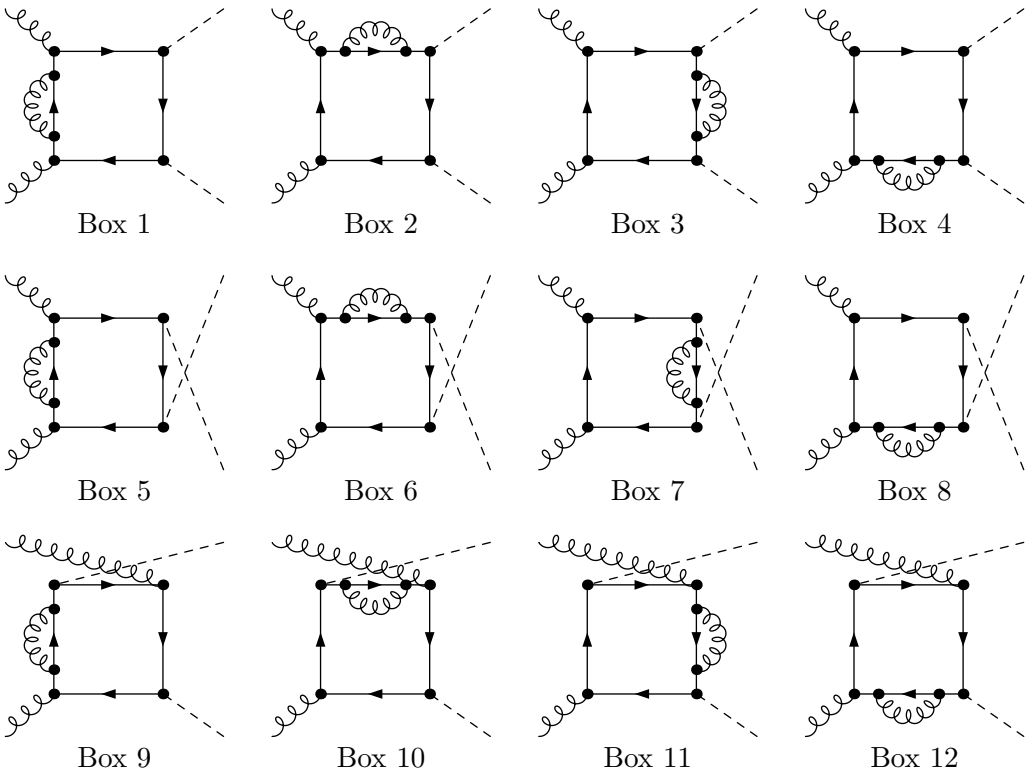

Topology 2:

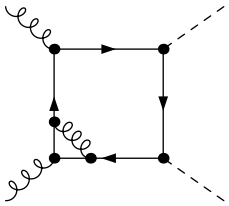
Box 13

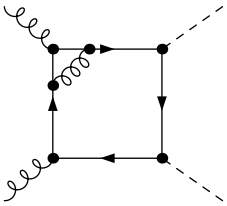
Box 14

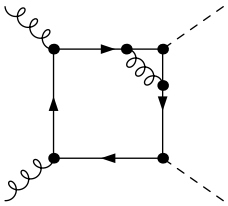
Box 15

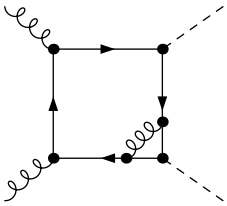
Box 16

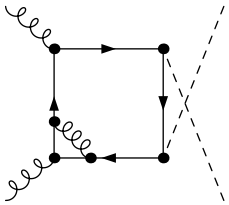
Box 17

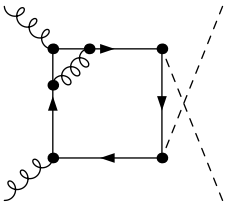
Box 18

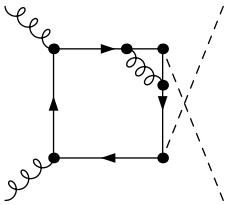
Box 19

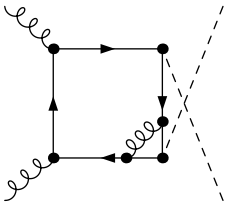
Box 20

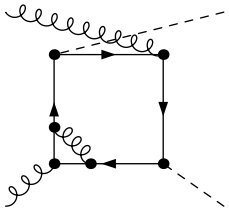
Box 21

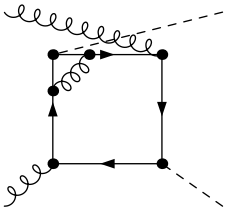
Box 22

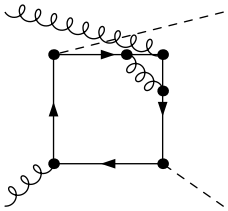
Box 23

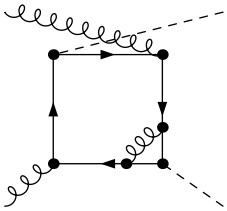
Box 24

Topology 3:

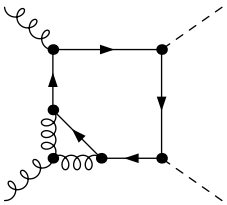
Box 25

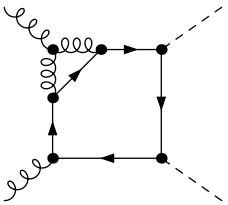
Box 26

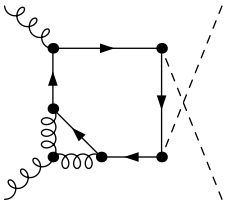
Box 27

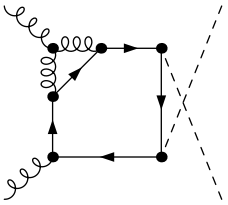
Box 28

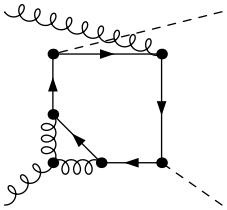
Box 29

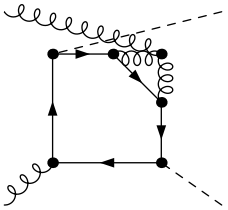
Box 30

Topology 4:

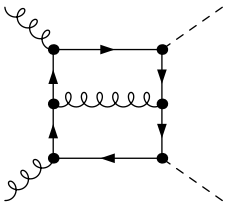
Box 31

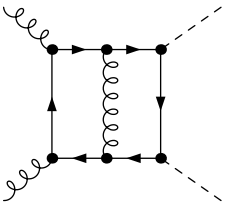
Box 32

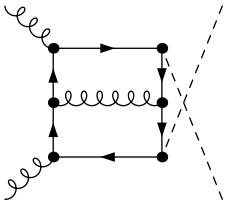
Box 33

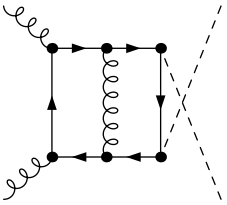
Box 34

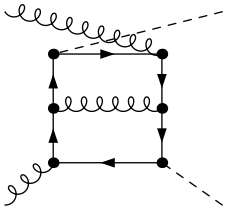
Box 35

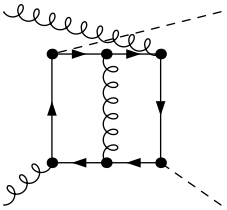
Box 36

Topology 5:

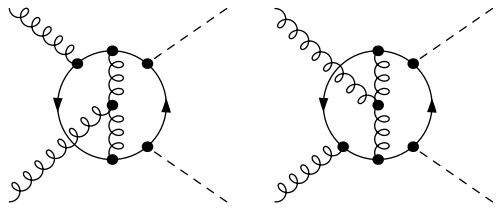

Box 37 Box 38

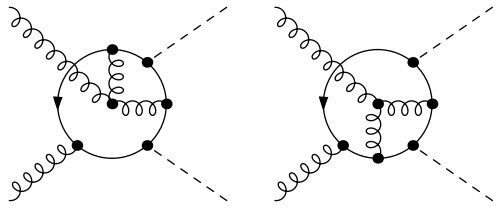

Box 39 Box 40

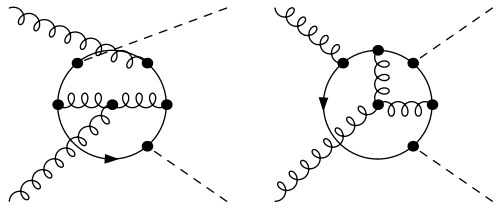

Box 41 Box 42

Topology 6:

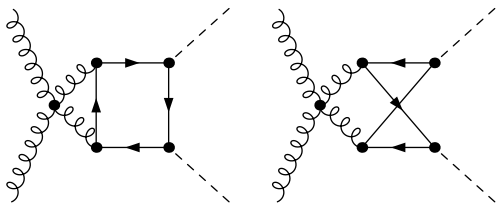

Box 43 Box 44

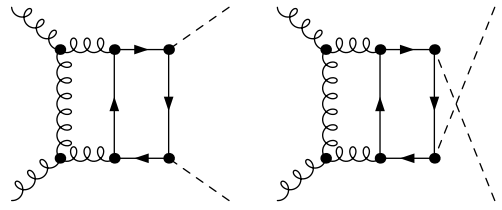

Box 45 Box 46

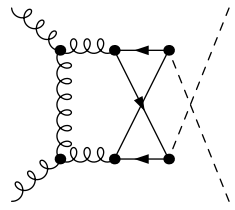

Box 47

Triangle Diagrams:

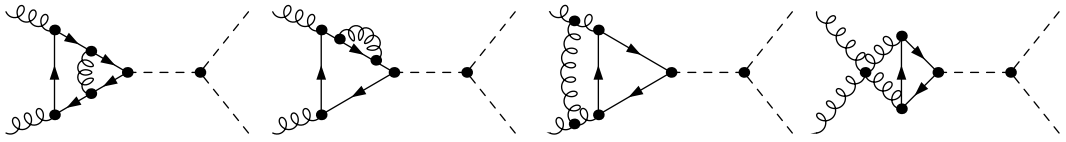

Triangle 1 Triangle 4 Triangle 7 Triangle 8

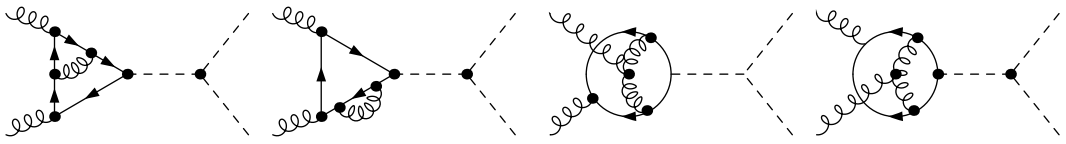

Triangle 2 Triangle 5 Triangle 9 Triangle 10

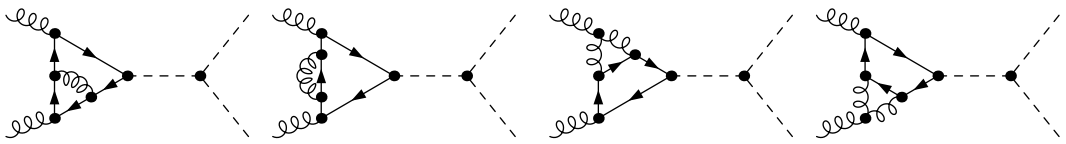

Triangle 3 Triangle 6 Triangle 11 Triangle 12

Double Triangle Diagrams:

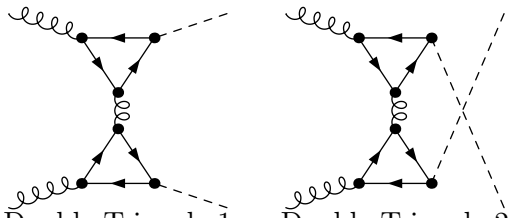

Double Triangle 1 Double Triangle 2

Appendix B

Real corrections

Complete set of the Feynman diagrams for the real QCD corrections to Higgs boson pair production. They are divided into groups with the same initial states.

gg → HHq:

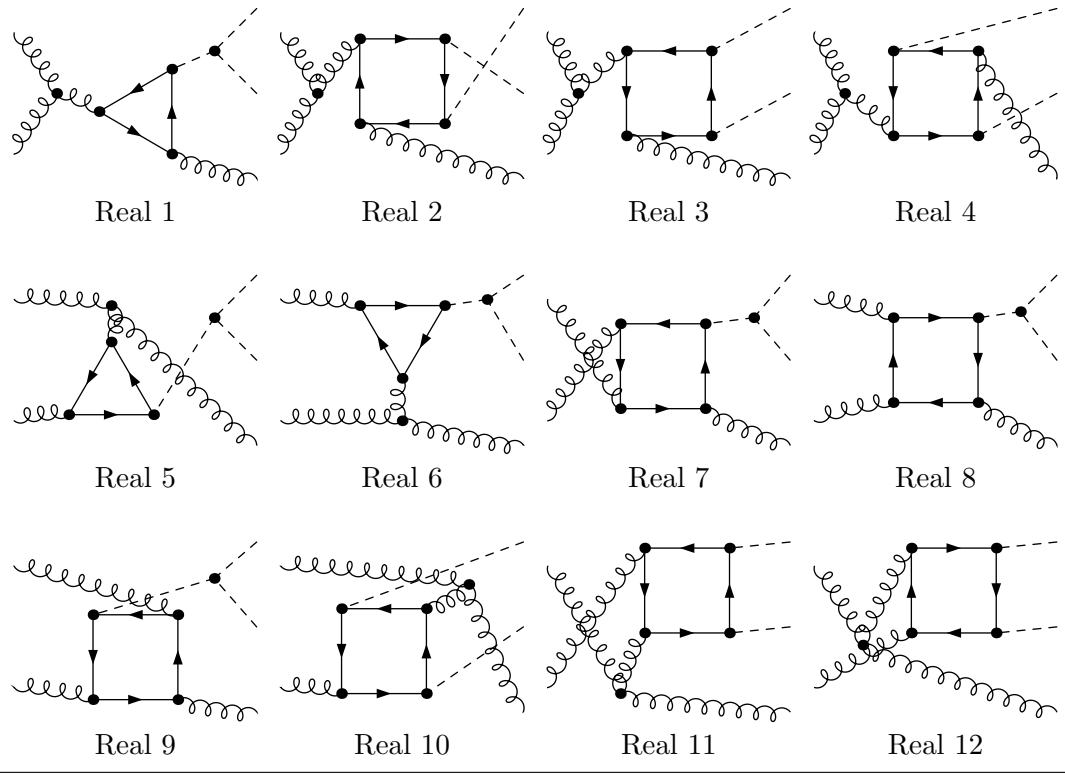

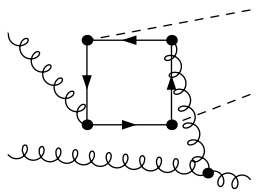

Real 13

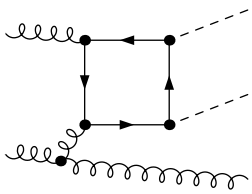

Real 14

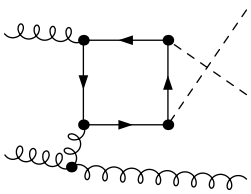

Real 15

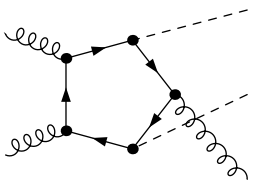

Real 16

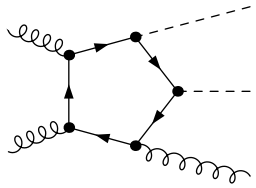

Real 17

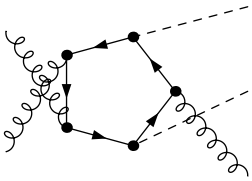

Real 18

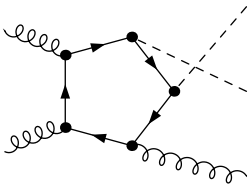

Real 19

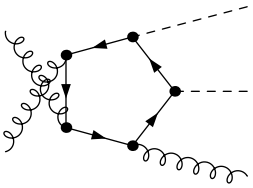

Real 20

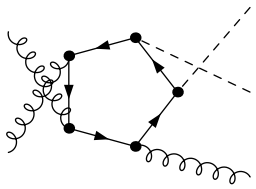

Real 21

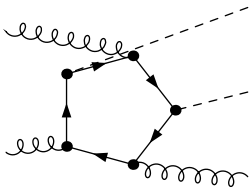

Real 22

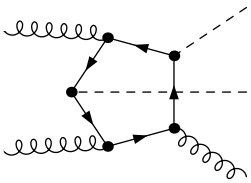

Real 23

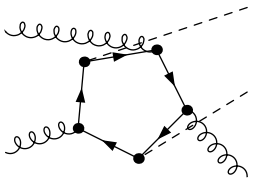

Real 24

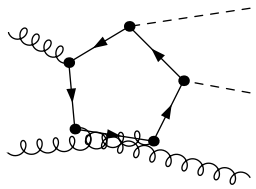

Real 25

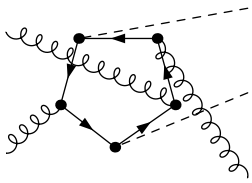

Real 26

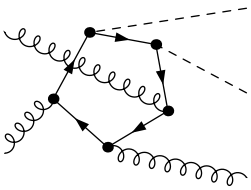

Real 27

$q\bar{q} \to HHg$:

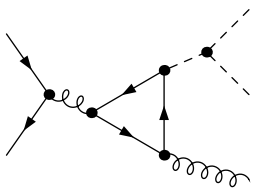

Real 28

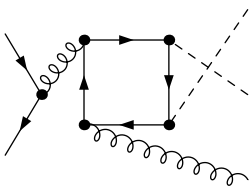

Real 29

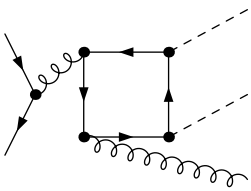

Real 30

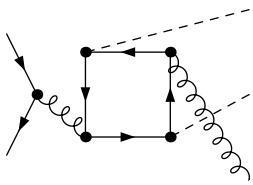

Real 31

gq → HHg:

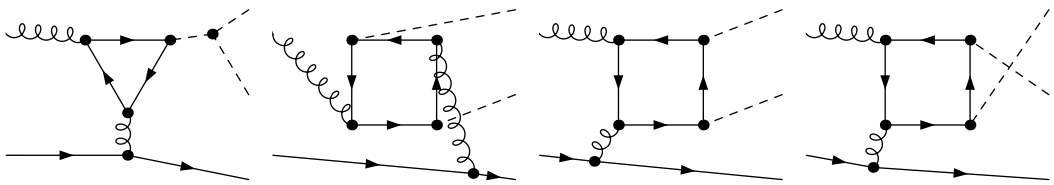

Real 32 | Real 33 | Real 34 | Real 35

Bibliography

[1] M. Gell-Mann, *A Schematic Model of Baryons and Mesons*, *Phys. Lett.* **8** (1964) 214.

[2] G. Zweig, *An SU(3) model for strong interaction symmetry and its breaking. Version 1*, .

[3] D. J. Gross and F. Wilczek, *Ultraviolet Behavior of Nonabelian Gauge Theories*, *Phys. Rev. Lett.* **30** (1973) 1343.

[4] H. D. Politzer, *Reliable Perturbative Results for Strong Interactions?*, *Phys. Rev. Lett.* **30** (1973) 1346.

[5] O. W. Greenberg, *Spin and Unitary Spin Independence in a Paraquark Model of Baryons and Mesons*, *Phys. Rev. Lett.* **13** (1964) 598.

[6] M. Y. Han and Y. Nambu, *Three Triplet Model with Double SU(3) Symmetry*, *Phys. Rev.* **139** (1965) B1006.

[7] H. Fritzsch, M. Gell-Mann and H. Leutwyler, *Advantages of the Color Octet Gluon Picture*, *Phys. Lett.* **47B** (1973) 365.

[8] D. J. Gross and F. Wilczek, *Asymptotically Free Gauge Theories - I*, *Phys. Rev.* **D8** (1973) 3633.

[9] H. D. Politzer, *Asymptotic Freedom: An Approach to Strong Interactions*, *Phys. Rept.* **14** (1974) 129.

[10] S. L. Glashow, *Partial Symmetries of Weak Interactions*, *Nucl. Phys.* **22** (1961) 579.

[11] S. Weinberg, *A Model of Leptons*, *Phys. Rev. Lett.* **19** (1967) 1264.

[12] A. Salam, *Weak and Electromagnetic Interactions*, *Conf. Proc.* **C680519** (1968) 367.

[13] P. W. Higgs, *Broken symmetries, massless particles and gauge fields*, *Phys. Lett.* **12** (1964) 132.

[14] P. W. Higgs, *Broken Symmetries and the Masses of Gauge Bosons*, *Phys. Rev. Lett.* **13** (1964) 508.

[15] P. W. Higgs, *Spontaneous Symmetry Breakdown without Massless Bosons*, *Phys. Rev.* **145** (1966) 1156.

[16] F. Englert and R. Brout, *Broken Symmetry and the Mass of Gauge Vector Mesons*, *Phys. Rev. Lett.* **13** (1964) 321.

[17] T. W. B. Kibble, *Symmetry breaking in nonAbelian gauge theories*, *Phys. Rev.* **155** (1967) 1554.

[18] G. S. Guralnik, C. R. Hagen and T. W. B. Kibble, *Global Conservation Laws and Massless Particles*, *Phys. Rev. Lett.* **13** (1964) 585.

[19] G. 't Hooft and M. J. G. Veltman, *Regularization and Renormalization of Gauge Fields*, *Nucl. Phys.* **B44** (1972) 189.

[20] G. 't Hooft, *Renormalizable Lagrangians for Massive Yang-Mills Fields*, *Nucl. Phys.* **B35** (1971) 167.

[21] ATLAS collaboration, G. Aad et al., *Observation of a new particle in the search for the Standard Model Higgs boson with the ATLAS detector at the LHC*, *Phys. Lett.* **B716** (2012) 1 [1207.7214].

[22] CMS collaboration, S. Chatrchyan et al., *Observation of a new boson at a mass of 125 GeV with the CMS experiment at the LHC*, *Phys. Lett.* **B716** (2012) 30 [1207.7235].

[23] A. Bredenstein, A. Denner, S. Dittmaier and M. M. Weber, *Precise predictions for the Higgs-boson decay $H \to WW/ZZ \to 4$ leptons*, *Phys. Rev.* **D74** (2006) 013004 [hep-ph/0604011].

[24] A. Bredenstein, A. Denner, S. Dittmaier and M. M. Weber, *Radiative corrections to the semileptonic and hadronic Higgs-boson decays $H \to WW/ZZ \to 4$ fermions*, *JHEP* **02** (2007) 080 [hep-ph/0611234].

[25] A. Bredenstein, A. Denner, S. Dittmaier and M. M. Weber, *Precision calculations for the Higgs decays $H \to ZZ/WW \to 4$ leptons*, *Nucl. Phys. Proc. Suppl.* **160** (2006) 131 [hep-ph/0607060].

[26] A. Djouadi, J. Kalinowski and M. Spira, *HDECAY: A Program for Higgs boson decays in the standard model and its supersymmetric extension*, *Comput. Phys. Commun.* **108** (1998) 56 [hep-ph/9704448].

[27] M. Spira, *QCD effects in Higgs physics*, *Fortsch. Phys.* **46** (1998) 203 [hep-ph/9705337].

[28] J. M. Butterworth et al., *THE TOOLS AND MONTE CARLO WORKING GROUP Summary Report from the Les Houches 2009 Workshop on TeV Colliders*, in *Physics at TeV colliders. Proceedings, 6th Workshop, dedicated to Thomas Binoth, Les Houches, France, June 8-26, 2009*, 2010, 1003.1643, arXiv:1003.1643.pdf.

[29] A. Djouadi, J. Kalinowski, M. Mühlleitner and M. Spira, *HDECAY: Twenty$_{++}$ Years After*, arXiv:1801.09506.

[30] LHC Higgs Cross Section Working Group collaboration, D. de Florian et al., *Handbook of LHC Higgs Cross Sections: 4. Deciphering the Nature of the Higgs Sector*, arXiv:1610.07922.

[31] S. G. Gorishnii, A. L. Kataev, S. A. Larin and L. R. Surguladze, *Scheme dependence of the next to next-to-leading QCD corrections to $\Gamma_{tot}(H^0 \to$ hadrons) and the spurious QCD infrared fixed point*, *Phys. Rev.* **D43** (1991) 1633.

[32] A. L. Kataev and V. T. Kim, *The Effects of the QCD corrections to $\Gamma(H^0 \to b\bar{b})$*, *Mod. Phys. Lett.* **A9** (1994) 1309.

[33] L. R. Surguladze, *Quark mass effects in fermionic decays of the Higgs boson in $\mathcal{O}(\alpha_s^2)$ perturbative QCD*, *Phys. Lett.* **B341** (1994) 60 [hep-ph/9405325].

[34] S. A. Larin, T. van Ritbergen and J. A. M. Vermaseren, *The Large top quark mass expansion for Higgs boson decays into bottom quarks and into gluons*, *Phys. Lett.* **B362** (1995) 134 [hep-ph/9506465].

[35] K. G. Chetyrkin and A. Kwiatkowski, *Second order QCD corrections to scalar and pseudoscalar Higgs decays into massive bottom quarks*, *Nucl. Phys.* **B461** (1996) 3 [hep-ph/9505358].

[36] K. G. Chetyrkin, *Correlator of the quark scalar currents and* $\Gamma_{tot}(H \to hadrons)$ *at*$\mathcal{O}(\alpha_s^3)$ *in pQCD*, *Phys. Lett.* **B390** (1997) 309 [hep-ph/9608318].

[37] P. A. Baikov, K. G. Chetyrkin and J. H. Kuhn, *Scalar correlator at* $\mathcal{O}(\alpha_s^4)$, *Higgs decay into b-quarks and bounds on the light quark masses*, *Phys. Rev. Lett.* **96** (2006) 012003 [hep-ph/0511063].

[38] J. Fleischer and F. Jegerlehner, *Radiative Corrections to Higgs Decays in the Extended Weinberg-Salam Model*, *Phys. Rev.* **D23** (1981) 2001.

[39] N. Sakai, *Perturbative QCD Corrections to the Hadronic Decay Width of the Higgs Boson*, *Phys. Rev.* **D22** (1980) 2220.

[40] T. Inami and T. Kubota, *Renormalization Group Estimate of the Hadronic Decay Width of the Higgs Boson*, *Nucl. Phys.* **B179** (1981) 171.

[41] S. G. Gorishnii, A. L. Kataev and S. A. Larin, *The Width of Higgs Boson Decay Into Hadrons: Three Loop Corrections of Strong Interactions*, *Sov. J. Nucl. Phys.* **40** (1984) 329.

[42] D. Yu. Bardin, B. M. Vilensky and P. K. Khristova, *Calculation of the Higgs boson decay width into fermion pairs*, *Sov. J. Nucl. Phys.* **53** (1991) 152.

[43] A. Dabelstein and W. Hollik, *Electroweak corrections to the fermionic decay width of the standard Higgs boson*, *Z. Phys.* **C53** (1992) 507.

[44] B. A. Kniehl, *Radiative corrections for* $H \to f$ *anti-f* (γ) *in the standard model*, *Nucl. Phys.* **B376** (1992) 3.

[45] A. Djouadi, D. Haidt, B. A. Kniehl, P. M. Zerwas and B. Mele, *Higgs in the standard model*, in *In *Munich/Annecy/Hamburg 1991, Proceedings, e+ e- collisions at 500-GeV, pt. A* 11-30*, 1991.

[46] M. Drees and K.-i. Hikasa, *Heavy Quark Thresholds in Higgs Physics*, *Phys. Rev.* **D41** (1990) 1547.

[47] M. Drees and K.-i. Hikasa, *NOTE ON QCD CORRECTIONS TO HADRONIC HIGGS DECAY*, *Phys. Lett.* **B240** (1990) 455.

[48] E. Braaten and J. P. Leveille, *Higgs Boson Decay and the Running Mass*, *Phys. Rev.* **D22** (1980) 715.

[49] A. Ghinculov, *Two loop heavy Higgs corrections to the Higgs fermionic width*, *Phys. Lett.* **B337** (1994) 137 [hep-ph/9405394].

[50] A. Ghinculov and J. J. van der Bij, *Massive two loop diagrams: The Higgs propagator*, *Nucl. Phys.* **B436** (1995) 30 [hep-ph/9405418].

[51] L. Durand, K. Riesselmann and B. A. Kniehl, *Onset of strong interactions in the Higgs sector of the standard model: $H \to f\bar{f}$ at two loops*, *Phys. Rev. Lett.* **72** (1994) 2534.

[52] L. Durand, B. A. Kniehl and K. Riesselmann, *Two loop $\mathcal{O}(G_F^2 M_H^4)$ corrections to the fermionic decay rates of the Higgs boson*, *Phys. Rev.* **D51** (1995) 5007 [hep-ph/9412311].

[53] T. Inami, T. Kubota and Y. Okada, *Effective Gauge Theory and the Effect of Heavy Quarks in Higgs Boson Decays*, *Z. Phys.* **C18** (1983) 69.

[54] A. Djouadi, M. Spira and P. M. Zerwas, *Production of Higgs bosons in proton colliders: QCD corrections*, *Phys. Lett.* **B264** (1991) 440.

[55] M. Spira, A. Djouadi, D. Graudenz and P. M. Zerwas, *Higgs boson production at the LHC*, *Nucl. Phys.* **B453** (1995) 17 [hep-ph/9504378].

[56] K. G. Chetyrkin, B. A. Kniehl and M. Steinhauser, *Hadronic Higgs decay to $\mathcal{O}(\alpha_s^4)$*, *Phys. Rev. Lett.* **79** (1997) 353 [hep-ph/9705240].

[57] S. Actis, G. Passarino, C. Sturm and S. Uccirati, *NLO Electroweak Corrections to Higgs Boson Production at Hadron Colliders*, *Phys. Lett.* **B670** (2008) 12 [arXiv:0809.1301].

[58] K. G. Chetyrkin, B. A. Kniehl and M. Steinhauser, *Virtual top quark effects on the $H \to b\bar{b}$ decay at next-to-leading order in QCD*, *Phys. Rev. Lett.* **78** (1997) 594 [hep-ph/9610456].

[59] A. Djouadi and P. Gambino, *Leading electroweak correction to Higgs boson production at proton colliders*, *Phys. Rev. Lett.* **73** (1994) 2528 [hep-ph/9406432].

[60] K. G. Chetyrkin, B. A. Kniehl and M. Steinhauser, *Three loop $\mathcal{O}(\alpha_s^2 G_F M_t^2)$ corrections to hadronic Higgs decays*, *Nucl. Phys.* **B490** (1997) 19 [hep-ph/9701277].

[61] U. Aglietti, R. Bonciani, G. Degrassi and A. Vicini, *Two loop light fermion contribution to Higgs production and decays*, *Phys. Lett.* **B595** (2004) 432 [hep-ph/0404071].

[62] G. Degrassi and F. Maltoni, *Two-loop electroweak corrections to Higgs production at hadron colliders*, *Phys. Lett.* **B600** (2004) 255 [hep-ph/0407249].

[63] S. Actis, G. Passarino, C. Sturm and S. Uccirati, *NNLO Computational Techniques: The Cases $H \to \gamma\gamma$ and $H \to gg$*, *Nucl. Phys.* **B811** (2009) 182 [arXiv:0809.3667].

[64] A. Djouadi, P. Gambino and B. A. Kniehl, *Two loop electroweak heavy fermion corrections to Higgs boson production and decay*, *Nucl. Phys.* **B523** (1998) 17 [hep-ph/9712330].

[65] G. Passarino, C. Sturm and S. Uccirati, *Complete Two-Loop Corrections to $H \to \gamma\gamma$*, *Phys. Lett.* **B655** (2007) 298 [arXiv:0707.1401].

[66] H.-Q. Zheng and D.-D. Wu, *First order QCD corrections to the decay of the Higgs boson into two photons*, *Phys. Rev.* **D42** (1990) 3760.

[67] A. Djouadi, M. Spira, J. J. van der Bij and P. M. Zerwas, *QCD corrections to gamma gamma decays of Higgs particles in the intermediate mass range*, *Phys. Lett.* **B257** (1991) 187.

[68] S. Dawson and R. P. Kauffman, *QCD corrections to $H \to \gamma\gamma$*, *Phys. Rev.* **D47** (1993) 1264.

[69] A. Djouadi, M. Spira and P. M. Zerwas, *Two photon decay widths of Higgs particles*, *Phys. Lett.* **B311** (1993) 255 [hep-ph/9305335].

[70] K. Melnikov and O. I. Yakovlev, *Higgs → two photon decay: QCD radiative correction*, *Phys. Lett.* **B312** (1993) 179 [hep-ph/9302281].

[71] N. Kodama and M. Oka, *The QCD sum rule for the delta (1232) in the instanton medium*, *Phys. Lett.* **B340** (1994) 221.

[72] J. Fleischer, O. V. Tarasov and V. O. Tarasov, *Analytical result for the two loop QCD correction to the decay $H \to \gamma\gamma$*, *Phys. Lett.* **B584** (2004) 294 [hep-ph/0401090].

[73] R. Harlander and P. Kant, *Higgs production and decay: Analytic results at next-to-leading order QCD*, *JHEP* **12** (2005) 015 [hep-ph/0509189].

[74] C. Anastasiou, S. Beerli, S. Bucherer, A. Daleo and Z. Kunszt, *Two-loop amplitudes and master integrals for the production of a Higgs boson via a massive quark and a scalar-quark loop*, *JHEP* **01** (2007) 082 [hep-ph/0611236].

[75] U. Aglietti, R. Bonciani, G. Degrassi and A. Vicini, *Analytic Results for Virtual QCD Corrections to Higgs Production and Decay*, *JHEP* **01** (2007) 021 [hep-ph/0611266].

[76] M. Steinhauser, *Corrections of $\mathcal{O}(\alpha_s^2)$ to the decay of an intermediate mass Higgs boson into two photons*, in *The Higgs puzzle - what can we learn from LEP-2, LHC, NLC and FMC? Proceedings, Ringberg Workshop, Tegernsee, Germany, December 8-13, 1996*, pp. 177–185, 1996, hep-ph/9612395.

[77] C. Sturm, *Higher order QCD results for the fermionic contributions of the Higgs-boson decay into two photons and the decoupling function for the $\overline{MS}$ renormalized fine-structure constant*, *Eur. Phys. J.* **C74** (2014) 2978 [arXiv:1404.3433].

[78] P. Maierhöfer and P. Marquard, *Complete three-loop QCD corrections to the decay $H \to \gamma\gamma$*, *Phys. Lett.* **B721** (2013) 131 [arXiv:1212.6233].

[79] M. Spira, A. Djouadi and P. M. Zerwas, *QCD corrections to the H Z gamma coupling*, *Phys. Lett.* **B276** (1992) 350.

[80] T. Gehrmann, S. Guns and D. Kara, *The rare decay $H \to Z\gamma$ in perturbative QCD*, *JHEP* **09** (2015) 038 [arXiv:1505.00561].

[81] R. Bonciani, V. Del Duca, H. Frellesvig, J. M. Henn, F. Moriello and V. A. Smirnov, *Next-to-leading order QCD corrections to the decay width H Z*, *JHEP* **08** (2015) 108 [arXiv:1505.00567].

[82] D. Graudenz, M. Spira and P. M. Zerwas, *QCD corrections to Higgs boson production at proton proton colliders*, *Phys. Rev. Lett.* **70** (1993) 1372.

[83] C. Anastasiou, S. Bucherer and Z. Kunszt, *HPro: A NLO Monte-Carlo for Higgs production via gluon fusion with finite heavy quark masses*, *JHEP* **10** (2009) 068 [arXiv:0907.2362].

[84] S. Catani, D. de Florian and M. Grazzini, *Higgs production in hadron collisions: Soft and virtual QCD corrections at NNLO*, *JHEP* **05** (2001) 025 [hep-ph/0102227].

[85] R. V. Harlander and W. B. Kilgore, *Soft and virtual corrections to proton proton → H + x at NNLO*, *Phys. Rev.* **D64** (2001) 013015 [hep-ph/0102241].

[86] R. V. Harlander and W. B. Kilgore, *Next-to-next-to-leading order Higgs production at hadron colliders*, *Phys. Rev. Lett.* **88** (2002) 201801 [hep-ph/0201206].

[87] C. Anastasiou and K. Melnikov, *Higgs boson production at hadron colliders in NNLO QCD*, *Nucl. Phys.* **B646** (2002) 220 [hep-ph/0207004].

[88] V. Ravindran, J. Smith and W. L. van Neerven, *NNLO corrections to the total cross-section for Higgs boson production in hadron hadron collisions*, *Nucl. Phys.* **B665** (2003) 325 [hep-ph/0302135].

[89] S. Marzani, R. D. Ball, V. Del Duca, S. Forte and A. Vicini, *Higgs production via gluon-gluon fusion with finite top mass beyond next-to-leading order*, *Nucl. Phys.* **B800** (2008) 127 [arXiv:0801.2544].

[90] T. Gehrmann, M. Jaquier, E. W. N. Glover and A. Koukoutsakis, *Two-Loop QCD Corrections to the Helicity Amplitudes for H → 3 partons*, *JHEP* **02** (2012) 056 [arXiv:1112.3554].

[91] C. Anastasiou, C. Duhr, F. Dulat and B. Mistlberger, *Soft triple-real radiation for Higgs production at N3LO*, *JHEP* **07** (2013) 003 [arXiv:1302.4379].

[92] C. Anastasiou, C. Duhr, F. Dulat, F. Herzog and B. Mistlberger, *Real-virtual contributions to the inclusive Higgs cross-section at N^3LO*, *JHEP* **12** (2013) 088 [arXiv:1311.1425].

[93] W. B. Kilgore, *One-loop single-real-emission contributions to $pp \to H + X$ at next-to-next-to-next-to-leading order*, *Phys. Rev.* **D89** (2014) 073008 [arXiv:1312.1296].

[94] Y. Li, A. von Manteuffel, R. M. Schabinger and H. X. Zhu, *N^3LO Higgs boson and Drell-Yan production at threshold: The one-loop two-emission contribution*, *Phys. Rev.* **D90** (2014) 053006 [arXiv:1404.5839].

[95] C. Anastasiou, C. Duhr, F. Dulat, E. Furlan, T. Gehrmann, F. Herzog et al., *Higgs Boson Gluon Fusion Production Beyond Threshold in N^3LO QCD*, *JHEP* **03** (2015) 091 [arXiv:1411.3584].

[96] C. Anastasiou, C. Duhr, F. Dulat, F. Herzog and B. Mistlberger, *Higgs Boson Gluon-Fusion Production in QCD at Three Loops*, *Phys. Rev. Lett.* **114** (2015) 212001 [arXiv:1503.06056].

[97] C. Anastasiou, C. Duhr, F. Dulat, E. Furlan, T. Gehrmann, F. Herzog et al., *High precision determination of the gluon fusion Higgs boson cross-section at the LHC*, *JHEP* **05** (2016) 058 [arXiv:1602.00695].

[98] B. Mistlberger, *Higgs boson production at hadron colliders at N^3LO in QCD*, *JHEP* **05** (2018) 028 [arXiv:1802.00833].

[99] T. Han, G. Valencia and S. Willenbrock, *Structure function approach to vector boson scattering in p p collisions*, *Phys. Rev. Lett.* **69** (1992) 3274 [hep-ph/9206246].

[100] T. Figy, C. Oleari and D. Zeppenfeld, *Next-to-leading order jet distributions for Higgs boson production via weak boson fusion*, *Phys. Rev.* **D68** (2003) 073005 [hep-ph/0306109].

[101] E. L. Berger and J. M. Campbell, *Higgs boson production in weak boson fusion at next-to-leading order*, *Phys. Rev.* **D70** (2004) 073011 [hep-ph/0403194].

[102] T. Figy and D. Zeppenfeld, *QCD corrections to jet correlations in weak boson fusion*, *Phys. Lett.* **B591** (2004) 297 [hep-ph/0403297].

[103] M. Ciccolini, A. Denner and S. Dittmaier, *Strong and electroweak corrections to the production of Higgs + 2jets via weak interactions at the LHC*, *Phys. Rev. Lett.* **99** (2007) 161803 [0707.0381].

[104] M. Ciccolini, A. Denner and S. Dittmaier, *Electroweak and QCD corrections to Higgs production via vector-boson fusion at the LHC*, *Phys. Rev.* **D77** (2008) 013002 [0710.4749].

[105] A. Denner, S. Dittmaier, S. Kallweit and A. Mck, *HAWK 2.0: A Monte Carlo program for Higgs production in vector-boson fusion and Higgs strahlung at hadron colliders*, *Comput. Phys. Commun.* **195** (2015) 161 [1412.5390].

[106] P. Bolzoni, F. Maltoni, S.-O. Moch and M. Zaro, *Higgs production via vector-boson fusion at NNLO in QCD*, *Phys. Rev. Lett.* **105** (2010) 011801 [arXiv:1003.4451].

[107] P. Bolzoni, F. Maltoni, S.-O. Moch and M. Zaro, *Vector boson fusion at NNLO in QCD: SM Higgs and beyond*, *Phys. Rev.* **D85** (2012) 035002 [arXiv:1109.3717].

[108] M. Cacciari, F. A. Dreyer, A. Karlberg, G. P. Salam and G. Zanderighi, *Fully Differential Vector-Boson-Fusion Higgs Production at Next-to-Next-to-Leading Order*, *Phys. Rev. Lett.* **115** (2015) 082002 [arXiv:1506.02660].

[109] F. A. Dreyer and A. Karlberg, *Vector-Boson Fusion Higgs Production at Three Loops in QCD*, *Phys. Rev. Lett.* **117** (2016) 072001 [1606.00840].

[110] O. Brein, A. Djouadi and R. Harlander, *NNLO QCD corrections to the Higgs-strahlung processes at hadron colliders*, *Phys. Lett.* **B579** (2004) 149 [hep-ph/0307206].

[111] G. Ferrera, M. Grazzini and F. Tramontano, *Higher-order QCD effects for associated WH production and decay at the LHC*, *JHEP* **04** (2014) 039 [arXiv:1312.1669].

[112] G. Ferrera, M. Grazzini and F. Tramontano, *Associated ZH production at hadron colliders: the fully differential NNLO QCD calculation*, *Phys. Lett.* **B740** (2015) 51 [arXiv:1407.4747].

[113] T. Han and S. Willenbrock, *QCD correction to the $p\ p \to W\ H$ and $Z\ H$ total cross-sections*, *Phys. Lett.* **B273** (1991) 167.

[114] M. L. Ciccolini, S. Dittmaier and M. Kramer, *Electroweak radiative corrections to associated WH and ZH production at hadron colliders*, *Phys. Rev.* **D68** (2003) 073003 [hep-ph/0306234].

[115] A. Denner, S. Dittmaier, S. Kallweit and A. Muck, *Electroweak corrections to Higgs-strahlung off W/Z bosons at the Tevatron and the LHC with HAWK*, *JHEP* **03** (2012) 075 [arXiv:1112.5142].

[116] W. Beenakker, S. Dittmaier, M. Kramer, B. Plumper, M. Spira and P. M. Zerwas, *Higgs radiation off top quarks at the Tevatron and the LHC*, *Phys. Rev. Lett.* **87** (2001) 201805 [hep-ph/0107081].

[117] W. Beenakker, S. Dittmaier, M. Kramer, B. Plumper, M. Spira and P. M. Zerwas, *NLO QCD corrections to t anti-t H production in hadron collisions*, *Nucl. Phys.* **B653** (2003) 151 [hep-ph/0211352].

[118] L. Reina and S. Dawson, *Next-to-leading order results for t anti-t h production at the Tevatron*, *Phys. Rev. Lett.* **87** (2001) 201804 [hep-ph/0107101].

[119] S. Dawson, L. H. Orr, L. Reina and D. Wackeroth, *Associated top quark Higgs boson production at the LHC*, *Phys. Rev.* **D67** (2003) 071503 [hep-ph/0211438].

[120] A. Denner and R. Feger, *NLO QCD corrections to off-shell top-antitop production with leptonic decays in association with a Higgs boson at the LHC*, *JHEP* **11** (2015) 209 [1506.07448].

[121] S. Frixione, V. Hirschi, D. Pagani, H. S. Shao and M. Zaro, *Weak corrections to Higgs hadroproduction in association with a top-quark pair*, *JHEP* **09** (2014) 065 [1407.0823].

[122] Y. Zhang, W.-G. Ma, R.-Y. Zhang, C. Chen and L. Guo, *QCD NLO and EW NLO corrections to $t\bar{t}H$ production with top quark decays at hadron collider*, *Phys. Lett.* **B738** (2014) 1 [1407.1110].

[123] A. Kulesza, L. Motyka, T. Stebel and V. Theeuwes, *Soft gluon resummation for associated $t\bar{t}H$ production at the LHC*, *JHEP* **03** (2016) 065 [arXiv:1509.02780].

[124] A. Broggio, A. Ferroglia, B. D. Pecjak, A. Signer and L. L. Yang, *Associated production of a top pair and a Higgs boson beyond NLO*, *JHEP* **03** (2016) 124 [arXiv:1510.01914].

[125] A. Broggio, A. Ferroglia, B. D. Pecjak and L. L. Yang, *NNLL resummation for the associated production of a top pair and a Higgs boson at the LHC*, *JHEP* **02** (2017) 126 [arXiv:1611.00049].

[126] J. Butterworth et al., *PDF4LHC recommendations for LHC Run II*, *J. Phys.* **G43** (2016) 023001 [arXiv:1510.03865].

[127] ATLAS, CMS collaboration, G. Aad et al., *Combined Measurement of the Higgs Boson Mass in pp Collisions at $\sqrt{s} = 7$ and 8 TeV with the ATLAS and CMS Experiments*, *Phys. Rev. Lett.* **114** (2015) 191803 [arXiv:1503.07589].

[128] CMS collaboration, S. Chatrchyan et al., *Study of the Mass and Spin-Parity of the Higgs Boson Candidate Via Its Decays to Z Boson Pairs*, *Phys. Rev. Lett.* **110** (2013) 081803 [arXiv:1212.6639].

[129] ATLAS collaboration, G. Aad et al., *Evidence for the spin-0 nature of the Higgs boson using ATLAS data*, *Phys. Lett.* **B726** (2013) 120 [arXiv:1307.1432].

[130] *Measurements of the Higgs boson production and decay rates and constraints on its couplings from a combined ATLAS and CMS analysis of the LHC pp collision data at $\sqrt{s} = 7$ and 8 TeV*, Tech. Rep. ATLAS-CONF-2015-044, CERN, Geneva, Sep, 2015.

[131] ATLAS, CMS collaboration, G. Aad et al., *Measurements of the Higgs boson production and decay rates and constraints on its couplings from a combined ATLAS and CMS analysis of the LHC pp collision data at $\sqrt{s} = 7$ and 8 TeV*, *JHEP* **08** (2016) 045 [arXiv:1606.02266].

[132] U. Baur, T. Plehn and D. L. Rainwater, *Determining the Higgs boson selfcoupling at hadron colliders*, *Phys. Rev.* **D67** (2003) 033003 [hep-ph/0211224].

[133] U. Baur, T. Plehn and D. L. Rainwater, *Measuring the Higgs boson self coupling at the LHC and finite top mass matrix elements*, *Phys. Rev. Lett.* **89** (2002) 151801 [hep-ph/0206024].

[134] U. Baur, T. Plehn and D. L. Rainwater, *Examining the Higgs boson potential at lepton and hadron colliders: A Comparative analysis*, *Phys. Rev.* **D68** (2003) 033001 [hep-ph/0304015].

[135] U. Baur, T. Plehn and D. L. Rainwater, *Probing the Higgs selfcoupling at hadron colliders using rare decays*, *Phys. Rev.* **D69** (2004) 053004 [hep-ph/0310056].

[136] M. J. Dolan, C. Englert and M. Spannowsky, *Higgs self-coupling measurements at the LHC*, *JHEP* **10** (2012) 112 [arXiv:1206.5001].

[137] A. Papaefstathiou, L. L. Yang and J. Zurita, *Higgs boson pair production at the LHC in the $b\bar{b}W^+W^-$ channel*, *Phys. Rev.* **D87** (2013) 011301 [arXiv:1209.1489].

[138] J. Baglio, A. Djouadi, R. Gröber, M. M. Mühlleitner, J. Quevillon and M. Spira, *The measurement of the Higgs self-coupling at the LHC: theoretical status*, *JHEP* **04** (2013) 151 [arXiv:1212.5581].

[139] F. Goertz, A. Papaefstathiou, L. L. Yang and J. Zurita, *Higgs Boson self-coupling measurements using ratios of cross sections*, *JHEP* **06** (2013) 016 [arXiv:1301.3492].

[140] W. Yao, *Studies of measuring Higgs self-coupling with $HH \to b\bar{b}\gamma\gamma$ at the future hadron colliders*, in *Proceedings, 2013 Community Summer Study on the Future of U.S. Particle Physics: Snowmass on the Mississippi (CSS2013): Minneapolis, MN, USA, July 29-August 6, 2013*, 2013, 1308.6302, arXiv:1308.6302.pdf.

[141] A. J. Barr, M. J. Dolan, C. Englert and M. Spannowsky, *Di-Higgs final states augMT2ed – selecting hh events at the high luminosity LHC*, *Phys. Lett.* **B728** (2014) 308 [arXiv:1309.6318].

[142] M. J. Dolan, C. Englert, N. Greiner and M. Spannowsky, *Further on up the road: hhjj production at the LHC*, *Phys. Rev. Lett.* **112** (2014) 101802 [arXiv:1310.1084].

[143] V. Barger, L. L. Everett, C. B. Jackson and G. Shaughnessy, *Higgs-Pair Production and Measurement of the Triscalar Coupling at LHC(8,14)*, *Phys. Lett.* **B728** (2014) 433 [arXiv:1311.2931].

[144] D. E. Ferreira de Lima, A. Papaefstathiou and M. Spannowsky, *Standard model Higgs boson pair production in the ($b\bar{b}$)($b\bar{b}$) final state*, *JHEP* **08** (2014) 030 [arXiv:1404.7139].

[145] C. Englert, F. Krauss, M. Spannowsky and J. Thompson, *Di-Higgs phenomenology in $t\bar{t}hh$: The forgotten channel*, *Phys. Lett.* **B743** (2015) 93 [arXiv:1409.8074].

[146] D. Wardrope, E. Jansen, N. Konstantinidis, B. Cooper, R. Falla and N. Norjoharuddeen, *Non-resonant Higgs-pair production in the $b\bar{b}$ $b\bar{b}$ final state at the LHC*, *Eur. Phys. J.* **C75** (2015) 219 [arXiv:1410.2794].

[147] Q. Li, Z. Li, Q.-S. Yan and X. Zhao, *Probe Higgs boson pair production via the 32j+Æ mode*, *Phys. Rev.* **D92** (2015) 014015 [arXiv:1503.07611].

[148] M. J. Dolan, C. Englert, N. Greiner, K. Nordstrom and M. Spannowsky, *$hhjj$ production at the LHC*, *Eur. Phys. J.* **C75** (2015) 387 [arXiv:1506.08008].

[149] Q.-H. Cao, Y. Liu and B. Yan, *Measuring trilinear Higgs coupling in WHH and ZHH productions at the high-luminosity LHC*, *Phys. Rev.* **D95** (2017) 073006 [arXiv:1511.03311].

[150] J. K. Behr, D. Bortoletto, J. A. Frost, N. P. Hartland, C. Issever and J. Rojo, *Boosting Higgs pair production in the $b\bar{b}b\bar{b}$ final state with multivariate techniques*, *Eur. Phys. J.* **C76** (2016) 386 [arXiv:1512.08928].

[151] F. Maltoni, E. Vryonidou and M. Zaro, *Top-quark mass effects in double and triple Higgs production in gluon-gluon fusion at NLO*, *JHEP* **11** (2014) 079 [arXiv:1408.6542].

[152] C.-T. Lu, J. Chang, K. Cheung and J. S. Lee, *An exploratory study of Higgs-boson pair production*, *JHEP* **08** (2015) 133 [arXiv:1505.00957].

[153] A. Djouadi, W. Kilian, M. Mühlleitner and P. M. Zerwas, *Testing Higgs self-couplings at e^+e^- linear colliders*, *Eur. Phys. J.* **C10** (1999) 27 [hep-ph/9903229].

[154] M. M. Mühlleitner, *Higgs particles in the standard model and supersymmetric theories*, Ph.D. thesis, Hamburg U., 2000. hep-ph/0008127.

[155] G. Cynolter, E. Lendvai and G. Pocsik, *Resonance production of three neutral supersymmetric Higgs bosons at LHC*, *Acta Phys. Polon.* **B31** (2000) 1749 [hep-ph/0003008].

[156] T. Plehn and M. Rauch, *The quartic higgs coupling at hadron colliders*, *Phys. Rev.* **D72** (2005) 053008 [hep-ph/0507321].

[157] T. Binoth, S. Karg, N. Kauer and R. Rückl, *Multi-Higgs boson production in the Standard Model and beyond*, *Phys. Rev.* **D74** (2006) 113008 [hep-ph/0608057].

[158] CLIC Physics Working Group collaboration, E. Accomando et al., *Physics at the CLIC multi-TeV linear collider*, in *Proceedings, 11th International Conference on Hadron spectroscopy (Hadron 2005): Rio de Janeiro, Brazil, August 21-26, 2005*, 2004, hep-ph/0412251, http://weblib.cern.ch/abstract?CERN-2004-005.

[159] R. Gonzalez Suarez, *Recent CMS results in top and Higgs physics. Recent CMS results in top and Higgs physics*, *Mod. Phys. Lett. A* **32** (2017) 1730026. 15 p.

[160] E. W. N. Glover and J. J. van der Bij, *HIGGS BOSON PAIR PRODUCTION VIA GLUON FUSION*, *Nucl. Phys.* **B309** (1988) 282.

[161] T. Plehn, M. Spira and P. M. Zerwas, *Pair production of neutral Higgs particles in gluon-gluon collisions*, *Nucl. Phys.* **B479** (1996) 46 [hep-ph/9603205].

[162] O. J. P. Eboli, G. C. Marques, S. F. Novaes and A. A. Natale, *TWIN HIGGS BOSON PRODUCTION*, *Phys. Lett.* **B197** (1987) 269.

[163] D. A. Dicus, C. Kao and S. S. D. Willenbrock, *Higgs Boson Pair Production From Gluon Fusion*, *Phys. Lett.* **B203** (1988) 457.

[164] W.-Y. Keung, *Double Higgs From $W - W$ Fusion*, *Mod. Phys. Lett.* **A2** (1987) 765.

[165] D. A. Dicus, K. J. Kallianpur and S. S. D. Willenbrock, *Higgs Boson Pair Production in the Effective W Approximation*, *Phys. Lett.* **B200** (1988) 187.

[166] K. J. Kallianpur, *Pair Production of Higgs Bosons via Heavy Quark Annihilation*, *Phys. Lett.* **B215** (1988) 392.

[167] A. Dobrovolskaya and V. Novikov, *On heavy Higgs boson production*, *Z. Phys.* **C52** (1991) 427.

[168] A. Abbasabadi, W. W. Repko, D. A. Dicus and R. Vega, *Comparison of Exact and Effective Gauge Boson Calculations for Gauge Boson Fusion Processes*, *Phys. Rev.* **D38** (1988) 2770.

[169] M. Moretti, S. Moretti, F. Piccinini, R. Pittau and A. D. Polosa, *Higgs boson self-couplings at the LHC as a probe of extended Higgs sectors*, *JHEP* **02** (2005) 024 [hep-ph/0410334].

[170] R. Frederix, S. Frixione, V. Hirschi, F. Maltoni, O. Mattelaer, P. Torrielli et al., *Higgs pair production at the LHC with NLO and parton-shower effects*, *Phys. Lett.* **B732** (2014) 142 [arXiv:1401.7340].

[171] V. D. Barger, T. Han and R. J. N. Phillips, *Double Higgs Boson Bremsstrahlung From W and Z Bosons at Supercolliders*, *Phys. Rev.* **D38** (1988) 2766.

[172] CMS collaboration, C. Collaboration, *Search for Higgs boson pair production in the final state containing two photons and two bottom quarks in proton-proton collisions at* $\sqrt{s} = 13$ TeV, .

[173] ATLAS Collaboration collaboration, *Study of the double Higgs production channel* $H(\to b\bar{b})H(\to \gamma\gamma)$ *with the ATLAS experiment at the HL-LHC*, Tech. Rep. ATL-PHYS-PUB-2017-001, CERN, Geneva, Jan, 2017.

[174] J. Baglio, A. Djouadi and J. Quevillon, *Prospects for Higgs physics at energies up to 100 TeV*, *Rept. Prog. Phys.* **79** (2016) 116201 [arXiv:1511.07853].

[175] M. McCullough, *An Indirect Model-Dependent Probe of the Higgs Self-Coupling*, *Phys. Rev.* **D90** (2014) 015001 [arXiv:1312.3322].

[176] G. Degrassi, P. P. Giardino, F. Maltoni and D. Pagani, *Probing the Higgs self coupling via single Higgs production at the LHC*, *JHEP* **12** (2016) 080 [arXiv:1607.04251].

[177] M. Gorbahn and U. Haisch, *Indirect probes of the trilinear Higgs coupling:* $gg \to h$ *and* $h \to \gamma\gamma$, *JHEP* **10** (2016) 094 [arXiv:1607.03773].

[178] W. Bizon, M. Gorbahn, U. Haisch and G. Zanderighi, *Constraints on the trilinear Higgs coupling from vector boson fusion and associated Higgs production at the LHC*, *JHEP* **07** (2017) 083 [arXiv:1610.05771].

[179] G. Degrassi, M. Fedele and P. P. Giardino, *Constraints on the trilinear Higgs self coupling from precision observables*, *JHEP* **04** (2017) 155 [arXiv:1702.01737].

[180] G. D. Kribs, A. Maier, H. Rzehak, M. Spannowsky and P. Waite, *Electroweak oblique parameters as a probe of the trilinear Higgs boson self-interaction*, *Phys. Rev.* **D95** (2017) 093004 [arXiv:1702.07678].

[181] S. Dawson, S. Dittmaier and M. Spira, *Neutral Higgs boson pair production at hadron colliders: QCD corrections*, *Phys. Rev.* **D58** (1998) 115012 [hep-ph/9805244].

[182] J. Grigo, J. Hoff, K. Melnikov and M. Steinhauser, *On the Higgs boson pair production at the LHC*, *Nucl. Phys.* **B875** (2013) 1 [arXiv:1305.7340].

[183] J. Grigo, J. Hoff and M. Steinhauser, *Higgs boson pair production: top quark mass effects at NLO and NNLO*, *Nucl. Phys.* **B900** (2015) 412 [arXiv:1508.00909].

[184] S. Borowka, N. Greiner, G. Heinrich, S. Jones, M. Kerner, J. Schlenk et al., *Higgs Boson Pair Production in Gluon Fusion at Next-to-Leading Order with Full Top-Quark Mass Dependence*, *Phys. Rev. Lett.* **117** (2016) 012001 [arXiv:1604.06447].

[185] S. Borowka, N. Greiner, G. Heinrich, S. P. Jones, M. Kerner, J. Schlenk et al., *Full top quark mass dependence in Higgs boson pair production at NLO*, *JHEP* **10** (2016) 107 [arXiv:1608.04798].

[186] D. de Florian and J. Mazzitelli, *Two-loop virtual corrections to Higgs pair production*, *Phys. Lett.* **B724** (2013) 306 [arXiv:1305.5206].

[187] J. Grigo, K. Melnikov and M. Steinhauser, *Virtual corrections to Higgs boson pair production in the large top quark mass limit*, *Nucl. Phys.* **B888** (2014) 17 [arXiv:1408.2422].

[188] D. de Florian and J. Mazzitelli, *Higgs pair production at next-to-next-to-leading logarithmic accuracy at the LHC*, *JHEP* **09** (2015) 053 [arXiv:1505.07122].

[189] L.-S. Ling, R.-Y. Zhang, W.-G. Ma, L. Guo, W.-H. Li and X.-Z. Li, *NNLO QCD corrections to Higgs pair production via vector boson fusion at hadron colliders*, *Phys. Rev.* **D89** (2014) 073001 [arXiv:1401.7754].

[190] J. C. Collins, D. E. Soper and G. F. Sterman, *Factorization of Hard Processes in QCD*, *Adv. Ser. Direct. High Energy Phys.* **5** (1989) 1 [hep-ph/0409313].

[191] G. Degrassi, P. P. Giardino and R. Gröber, *On the two-loop virtual QCD corrections to Higgs boson pair production in the Standard Model*, *Eur. Phys. J.* **C76** (2016) 411 [arXiv:1603.00385].

[192] R. N. Cahn, M. S. Chanowitz and N. Fleishon, *Higgs Particle Production by Z → H Gamma*, *Phys. Lett.* **82B** (1979) 113.

[193] L. Bergstrom and G. Hulth, *Induced Higgs Couplings to Neutral Bosons in e^+e^- Collisions*, *Nucl. Phys.* **B259** (1985) 137.

[194] J. C. Collins, F. Wilczek and A. Zee, *Low-Energy Manifestations of Heavy Particles: Application to the Neutral Current*, *Phys. Rev.* **D18** (1978) 242.

[195] G. P. Lepage, *A New Algorithm for Adaptive Multidimensional Integration*, *J. Comput. Phys.* **27** (1978) 192.

[196] L.F.Richardson, *Ix. the approximate arithmetical solution by finite differences of physical problems involving differential equations, with an application to the stresses in a masonry dam*, *Philosophical Transactions of the Royal Society of London A: Mathematical, Physical and Engineering Sciences* **210** (1911) 307.

[197] T. Hahn, *Generating Feynman diagrams and amplitudes with FeynArts 3*, *Comput. Phys. Commun.* **140** (2001) 418 [hep-ph/0012260].

[198] T. Hahn and M. Perez-Victoria, *Automatized one loop calculations in four-dimensions and D-dimensions*, *Comput. Phys. Commun.* **118** (1999) 153 [hep-ph/9807565].

[199] A. Denner, S. Dittmaier and L. Hofer, *Collier: a fortran-based Complex One-Loop LIbrary in Extended Regularizations*, *Comput. Phys. Commun.* **212** (2017) 220 [arXiv:1604.06792].

[200] S. Catani and M. H. Seymour, *A General algorithm for calculating jet cross-sections in NLO QCD*, *Nucl. Phys.* **B485** (1997) 291 [hep-ph/9605323].

[201] L. A. Harland-Lang, A. D. Martin, P. Motylinski and R. S. Thorne, *Parton distributions in the LHC era: MMHT 2014 PDFs*, *Eur. Phys. J.* **C75** (2015) 204 [arXiv:1412.3989].

[202] I. S. M. Abramowitz, *Handbook of Mathematical Functions*. 1964.

Acknowledgements

First of all, I would like to thank Dr. Michael Spira for initiating this project, for his huge technical and moral support during the last years and the very fruitful discussions, especially during running. A great thank goes to Prof. Dr. Gehrmann for his inputs during our annual meetings and for proof-reading my thesis. My gratitude is extended to Prof. Dr. Stefan Dittmaier for taking part as the co-examiner and for providing his Mathematica code producing the virtual corrections in the heavy-top limit of the individual diagrams. Further, I would like to thank all my collaborators Prof. Dr. Margarete Mühlleitner, Dr. Juraj Streicher, Dr. Julien Baglio and Dr. Francisco Campanario. In particular, I would like to thank Prof. Dr. Margarete Mühlleitner for the hospitality during our numerous meetings in Karlsruhe and for proof-reading my thesis. A special thank goes to Juraj Streicher for introducing me to the calculation of the real corrections as well as for proof-reading the respective part of my thesis. I would like to thank all the current and former members of the theory group of the Paul Scherrer Institut for the great time I had there. Especially, I would like to thank my office mate Yannick Ulrich for the many interesting discussions during our tea breaks and for proof-reading my thesis. Finally, I would like to thank my family for the moral support.